Advanced Germanium p-i-n and Avalanche Photodetectors for Low-Power Optical Interconnects

Geavanceerde p-i-n-fotodetectoren in germanium en 'avalanche'-fotodetectoren voor optische interconnecties met laag vermogen

Hongtao Chen

Promotoren: prof. dr. ir. G. Roelkens, dr. ir. J. Van Campenhout
Proefschrift ingediend tot het behalen van de graad van
Doctor in de ingenieurswetenschappen: fotonica

UNIVERSITEIT
GENT

Vakgroep Informatietechnologie
Voorzitter: prof. dr. ir. D. De Zutter
Faculteit Ingenieurswetenschappen en Architectuur
Academiejaar 2016 - 2017

ISBN 978-90-8578-935-2
NUR 959
Wettelijk depot: D/2016/10.500/67

Universiteit Gent
Faculteit Ingenieurswetenschappen en Architectuur
Vakgroep Informatietechnologie

Promotoren: Prof. dr. ir. Gunther Roelkens
dr. ir. Joris Van Campenhout

Examencommissie:

Prof. dr. ir. Patrick De Baets (voorzitter)	Universiteit Gent, Electrical Energy, Systems and Automation
Prof. dr. ir. Gunther Roelkens (promotor)	Universiteit Gent, INTEC
dr. ir. Joris Van Campenhout (promotor)	imec, Leuven
Prof. dr. ir. Dries Van Thourhout (secretaris)	Universiteit Gent, INTEC
Prof. dr. ir. Laurent Vivien	Université Paris-Sud
Prof. dr. ir. Jeremy Witzens	RWTH Aachen University
Prof. dr. ir. Xin Yin	Universiteit Gent, INTEC
Prof. dr. ir. Kristiaan Neyts	Universiteit Gent, ELIS

Universiteit Gent
Faculteit Ingenieurswetenschappen en architectuur

Vakgroep Informatietechnologie
Technologiepark-Zwijnaarde 15, B-9052 Gent, België

Tel.: +32-9-264.33.30
Fax.: +32-9-331.35.93

Dit werk kwam tot stand in het kader van het imec Optical IO programma.

Proefschrift tot het behalen van de graad van
Doctor in de ingenieurswetenschappen: fotonica
Academiejaar 2016-2017

Dankwoord

I express my special thanks to my supervisor prof. Gunther Roelkens and Dr. Joris Van Campenhout, who led me into the research world of Si photonics. I also express my thanks to the imec Si photonics team and Jochem Verbist/ Xin Yin/ Johan Bauwelinck from Intec design group. The Ge p-i-n PDs and Ge APDs that I have been working on were fabricated in the imec process line. While I was doing design for these devices, the imec Si photonics team contribute a lot to the fabrication. Also for the characterization of these devices, the dedicated members in the imec Si photonics team helped me to setup the measurement system, mostly for the wafer-scale characterization. The Ge APD optical receivers were constructed under the help from Intec design, and the trans-impedance amplifier chips adopted also come from Intec design. In the characterization of such optical receivers, they (Jochem Verbist/ Xin Yin/ Johan Bauwelinck) helped me to setup the electrical part of the measurement system and provided a lot of guidance.

Ghent, september 2016
Hongtao Chen

Table of Contents

Nederlandstalige samenvatting

1 Optische verbindingen gebaseerd op silicium fotonica

Volgens een Cisco Global Cloud Index 2014-2019 rapport, zal het jaarlijkse globale datacenter IP verkeer 10.4 zettabytes bereiken tegen eind 2019. Dit is het gevolg van het toenemende aantal multimedia-diensten, Video on Demand, HD televisie, en het toenemende aantal internetgebruikers. Meer dan 86% van de taken zal verwerkt worden door cloud data centers, en tegen 2019 zal 56% van de cloud workload in publieke cloud data centers gebeuren, ten opzicht van 30 procent in 2014.

Om dit te realizeren zijn grote datacenters vereist met duizenden servers geconnecteerd via hoge bandbreedte switches. Optische interconnecties tussen clusters van servers en de switches laten toe om hoge datadebieten, lage *latency* en lager vermogenverbruik te bekomen vergeleken met de huidige netwerken. Silicium fotonica is een interessante technologie om deze optische interconnecties in te realizeren aangezien CMOS fabricage-infrastructuur kan gebruikt worden om compacte en goedkope fotonische geïntegreerde circuits te realizeren.

Een optische zender/ontvanger is de belangrijkste module voor optische interconnecties, waarbij een zender en ontvanger samen geïntegreerd zijn in een enkele module. Een on-off keying (OOK) 4-kanaal CWDM zender/ontvanger gerealizeerd in silicium fotonica met 20 Gbps line rate werd gedemonstreerd door imec, zoals getoond in Fig. 1. De zender/ontvanger bestaat uit een 40 nm CMOS elektronische zender/ontvanger die door middel van flip-chip integratie geconnecteerd is aan een 130 nm silicium fotonica chip, bestaande uit een 4-kanaal microring modulator, een 4 kanaal micro-ring WDM demultiplexer en 4 Ge fotodetectoren. Een grating coupler wordt gebruikt als interface met single mode optische vezel. Het optische datasignaal wordt verzonden over 2km optische vezel alvorens in de ontvanger gekoppeld te worden.

Het energie-efficiëntie is de belangrijkste performantie-indicator van een optische transceiver. Voor 'foutloze' transmissie (bit error rate 1×10^{-12}) is het energie-efficiëntie 5.05 pJ/bit. De laser verbruikt 35% van dit vermogenbudget. Dit is omdat de laser een voldoende hoog uitgangsvermogen moet leveren, om voldoende licht over te houden aan de detector, teneinde een signaal te genereren dat substantieel sterker is dan de ruis van de elektronische ontvanger. Een effectieve manier om het link budget te verbeteren is om de gevoeligheid van de

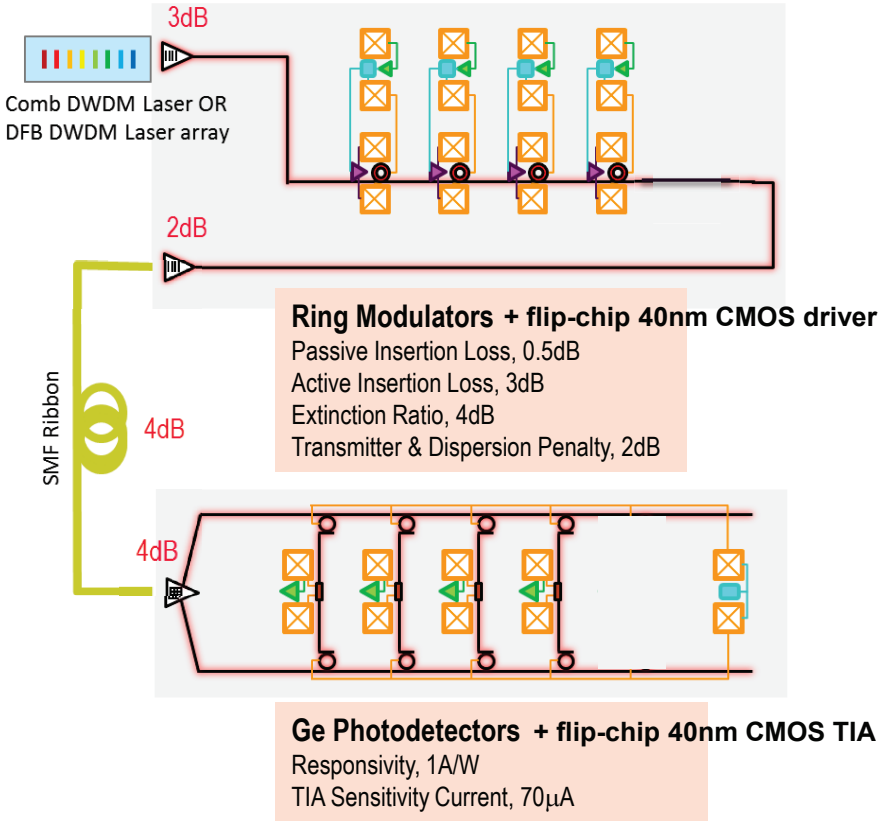

Figuur 1: OOK 4×20 Gbps CWDM Si fotonica optische zender/ontvanger gedemonstreerd door imec.

ontvanger te verhogen. Daardoor dient de laser minder optisch vermogen te genereren. Een 6dB verbetering van de gevoeligheid van de ontvanger zou leiden tot een reductie van het vermogenverbruik van de link met 26%, gewoon door het lagere vermogenverbruik van de laser.

In het optische domein betekent het realizeren van een ontvanger met hoge gevoeligheid het ontwikkelen van hoogperformante p-i-n fotodetectoren en avalanche fotodetectoren. Dit is het onderwerp van dit doctoraat.

2 Si-gecontacteerde germanium p-i-n fotodetectoren

Conventionele Ge golfgeleider p-i-n fotodetectoren vereisen dopering in Ge en een metaalcontact op Ge om de p-i-n junctie te vormen. Lichtabsorptie door het me-

taalcontact is een belangrijke oorzaak van vermindere responsiviteit van een dergelijke fotodetector. Bovendien is het contacteren van Ge minder goed ontwikkeld in standaard CMOS *foundries*. De hoge contactweerstand aan de metaal/germanium interface leidt tot een grote RC-constante, hetgeen normaal gezien de bandbreedte van de Ge p-i-n fotodetector bepaald. In dit werk demonstreerden we een Ge p-i-n fotodetector zonder metaalcontacten op Ge, gegroeid op en gecontacteerd via een silicium p-i-n fotodetector, met een 400 nm dikke Ge laag (Si-LPIN GePD genaamd), zoals getoond in Fig. 2. Een responsiviteit van 1 A/W over de volledige C-band werd gedemonstreerd, zoals getoond in Fig. 3. De donkerstroom is 3 nA bij -1 V bias. De 3dB bandbreedte van de detector was beperkt tot 20 GHz bij -1 V bias (bij een golflengte van 1550 nm), zoals getoond in Fig. 4.

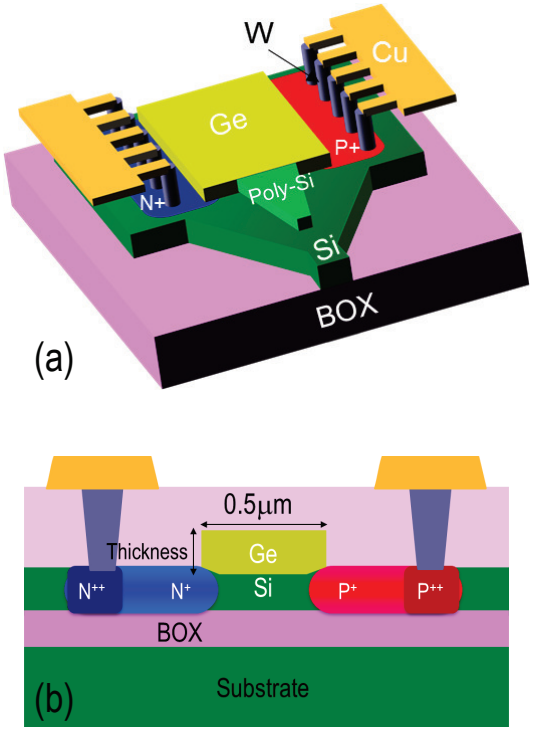

Figuur 2: (a) 3-D schematische weergave van de Si-LPIN GePD. (b) schematische dwarsdoorsnede van de Si-LPIN GePD

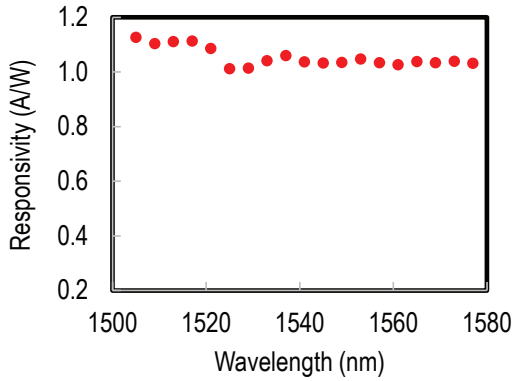

Figuur 3: Responsiviteit als functie van de golflengte in de C-band voor de 400 nm Si-LPIN GePD bij -1.2 V bias.

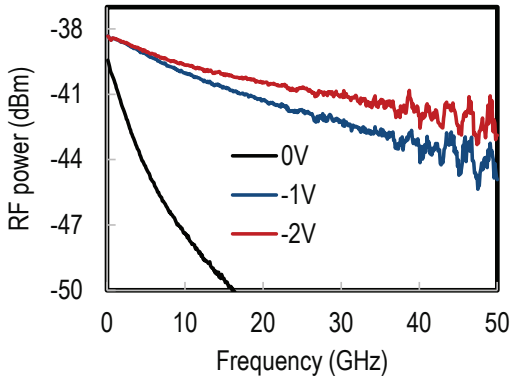

Figuur 4: Klein-signaal transmissieparameter S_{21} als functie van de frequentie voor de 400 nm Si-LPIN GePD bij 1550 nm golflengte.

Door gebruik te maken van een 160 nm dikke Ge laag om de transit-tijd te reduceren, kon de 3dB bandbreedte bij -1 V vergroot worden to 67 GHz en 44 GHz bij respectievelijk 1550 nm en 1310 nm voor een 14 μm lange Si-LPIN GePD. De S_{21} parameters gemeten bij 1550 nm en de corresponderende 3dB bandbreedte als functie van het gemiddeld optisch vermogen in de silicium golfgeleider is getoond in Fig. 5. De junctiecapaciteit is 6.8 fF bij -1 V bias, en de bandbreedte is nog steeds gelimiteerd door de transit-tijd. De optische koppeling van de siliciumgolfgeleider naar de Ge golfgeleider is geoptimalizeerd door het gebruik van een poly-Si taper boven de diepgeëtste Si taper. De responsiviteit bij -1 V bias was 0.74 A/W en 0.93 A/W bij respectievelijk 1550 nm en 1310 nm, zoals getoond in Fig. 6.

De donkerstroom was 4 nA bij -1 V. 56 Gbps OOK-NRZ data-ontvangst werd gedemonstreerd met open oogdiagramma zowel bij 1550nm als 1310nm golflengte. 80 Gbps en 100 Gbps OOK RZ data-ontvangst gebruik makende van een 14 μm lange Si-LPIN GePD werd ook gedemonstreerd bij 1550nm golflengte. De 100 Gbps oogdiagramma zijn getoond in Fig. 7.

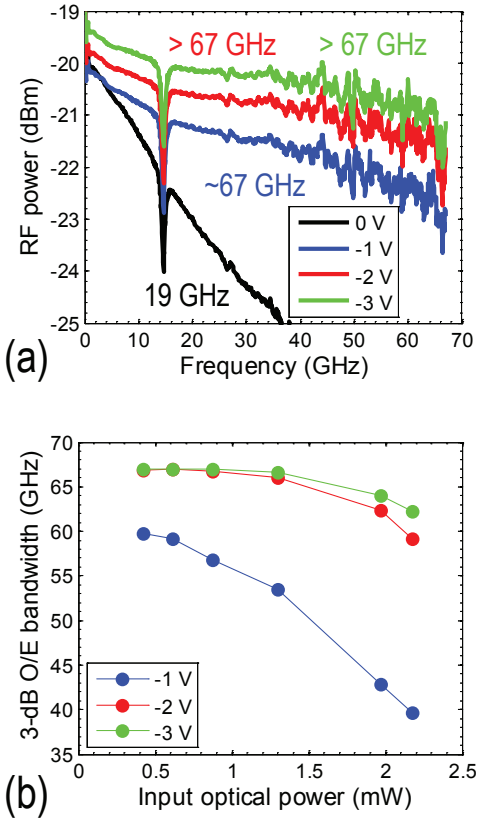

Figuur 5: (a) Klein-signaal S_{21} transmissieparameter als functie van frequentie voor de 160 nm Si-LPIN GePD bij 1550 nm. (b) 3dB bandbreedte als functie van het optische ingangsvermogen bij 1550 nm.

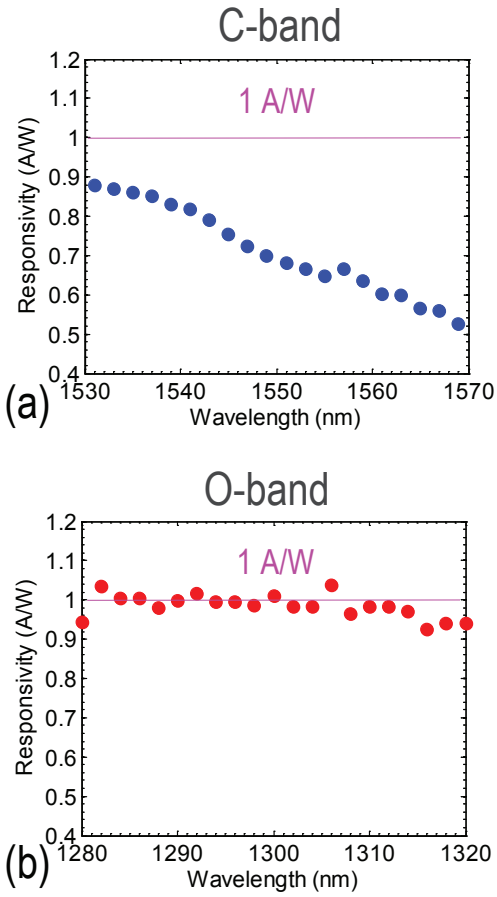

Figuur 6: Responsiviteit als functie van golflengte voor de 160 nm Si-LPIN GePD in (a) de C-band en (b) de O-band bij -1.2 V bias.

3 Lage spanning germanium avalanche fotodetectoren

Een studie werd uitgevoerd om een Ge APD te implementeren op imec's silicium fotonicaplatform. Een verticale p+(Ge)-i(Ge)-n+(Si) (VPIN) junctie bleek goed geschikt te zijn hiervoor. Deze VPIN diode met een 400 nm dikke Ge laag getoond in Fig. 8, leidt tot een sterk elektrisch veld (1×10^5 V/cm) in de onderste 200 nm van de Ge laag bij een biasspanning van -5.5 V. Daardoor kan er een grote avalanche multiplicatie verwacht worden bij vrij lage biasspanningen.

De gedemonstreerde Ge APD had een 3dB bandbreedte boven 10 GHz bij een

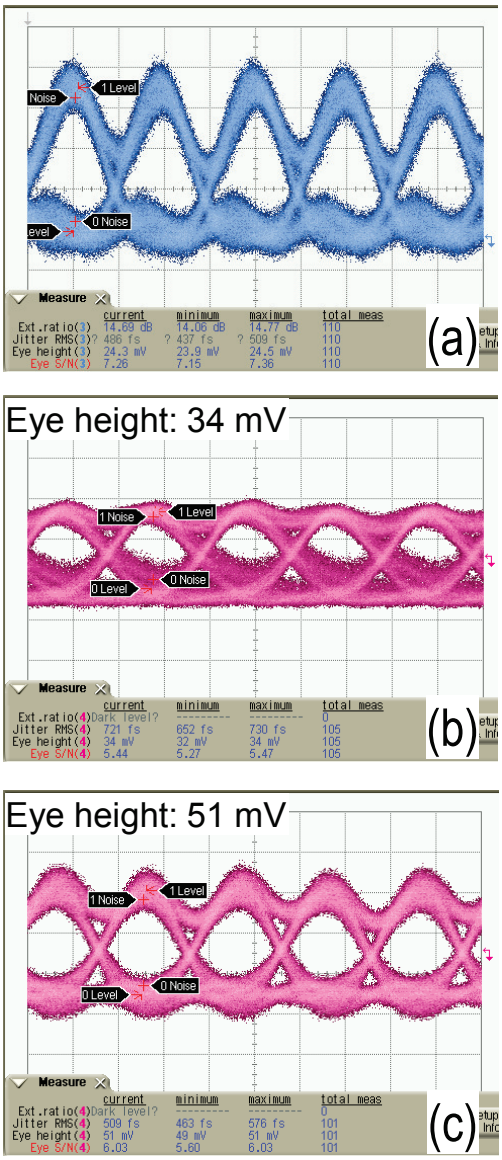

Figuur 7: Het 100 Gbps RZ oogdiagram gemeten met (a) een 70 GHz commerciële p-i-n fotodetector (u2t XPDV 3120R), (b) de 160 nm Si-LPIN GePD bij -1 V bias, (c) de 160 nm Si-LPIN GePD bij -2 V bias.

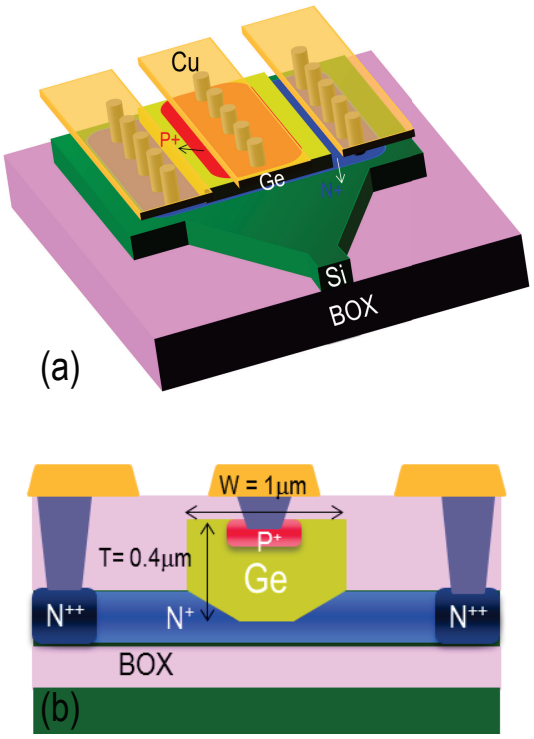

Figuur 8: (a) 3-D schema van een VPIN GePD. (b) schematische dwarsdoorsnede van een VPIN GePD.

avalanche versterking van 10.2 bij -6.2 V bias, resulterend in een winst- bandbreedteproduct van meer dan 100 GHz, zoals getoond in Fig. 9. De detector heeft een donkerstroom van 17 nA bij -1 V en een hoge primaire responsiviteit van 0.6 A/W. De gemeten effectieve verhouding van de ionizatietempo's van elektronen en gaten (k_{eff}) was 0.5, zoals getoond in Fig. 10. Een verbetering van de gevoeligheid van 5.8 dB bij 5.9 V bias werd aangetoond door bit error rate metingen op een optische ontvanger, zoals getoond in Fig. 11. De primaire gevoeligheid was -17.6 dBm en -18.6 dBm gemiddeld ingangsvermogen (NRZ, 10Gbps) bij -1.7 V voor een bit error rate van respectievelijk 1×10^{-12} en 1×10^{-9}. Dit resulteert in een absolute gevoeligheid in avalanche regime van -23.4 dBm en -24.4 dBm bij een bit error rate van respectievelijk 1×10^{-12} en 1×10^{-9}.

Om de VPIN Ge APD performantie te verbeteren, moeten zowel de primaire responsiviteit en de avalanche-versterking verbeterd worden. Een dunnere Ge laag (185 nm) werd voorgesteld om beter avalanche-gedrag te bekomen bij een lage biasspanning. Om excessieve absorptie in de metaalcontacten te vermijden werd een bredere Ge golfgeleider van 2.2 μm gebruikt met 2 metaalplugs weg van het

centrum van de Ge golfgeleider, zoals getoond in Fig. 12.

Een 20 Gbps 1310 nm optische ontvanger gebaseerd op een dergelijke Ge APD werd gedemonstreerd in dit werk die een 6.2 dB verbetering van de gevoeligheid toont bij -5 V biasspanning, zoals getoond in Fig. 13. Een lage k_{eff} van 0.2 werd gemeten door middel van ruismetingen, zoals getoond in Fig. 14. Het waferschaal gemiddelde winst-bandbreedteprodukt is 140 GHz bij -5 V bias, zoals getoond in Fig. 15.

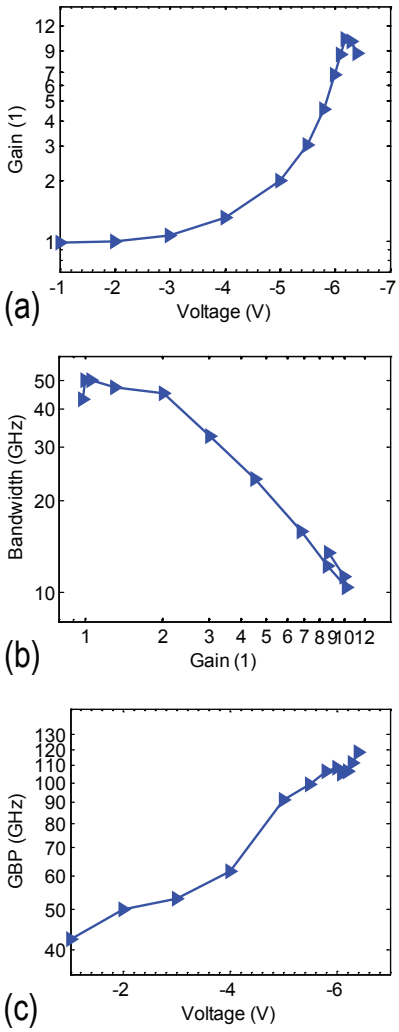

Figuur 9: (a) Avalanche-versterking geëxtraheerd van kleinsignaalmetingen als functie van de biasspanning. (b) gemeten 3dB bandbreedte versus avalanche-versterking geëxtraheerd van kleinsignaalmetingen (c) winst ×bandbreedteproduct als functie van de biasspanning.

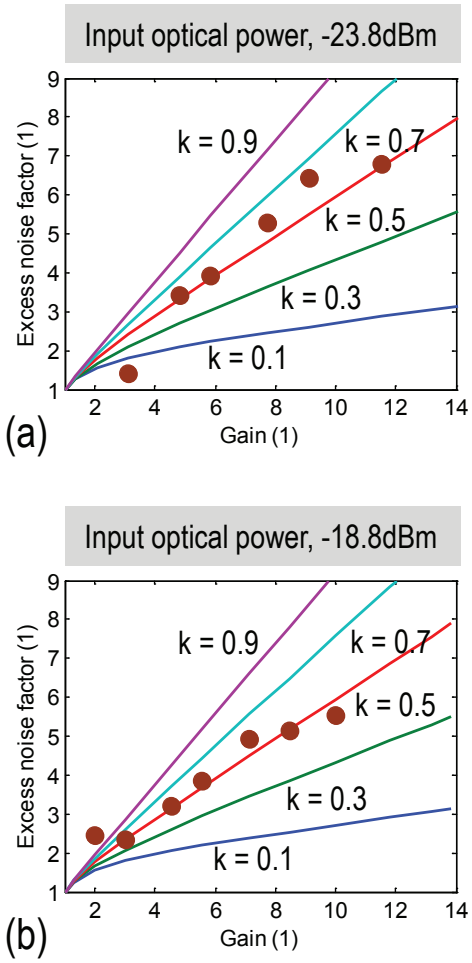

Figuur 10: Excess ruisfactor als functie van de versterking bij een input optisch vermogen van (a) -23.8dBm en (b) -18.8 dBm.

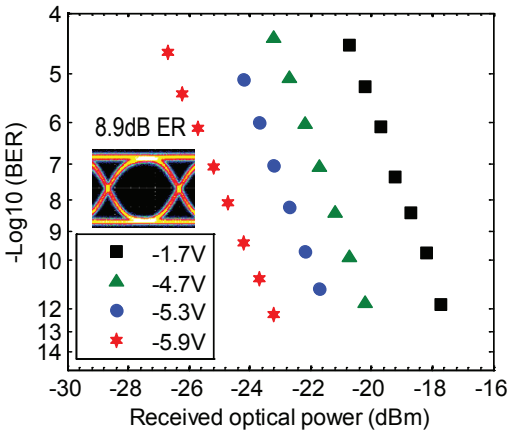

Figuur 11: Gemeten bit error rate als functie van het input optisch vermogen voor verschillende biasspanningen.

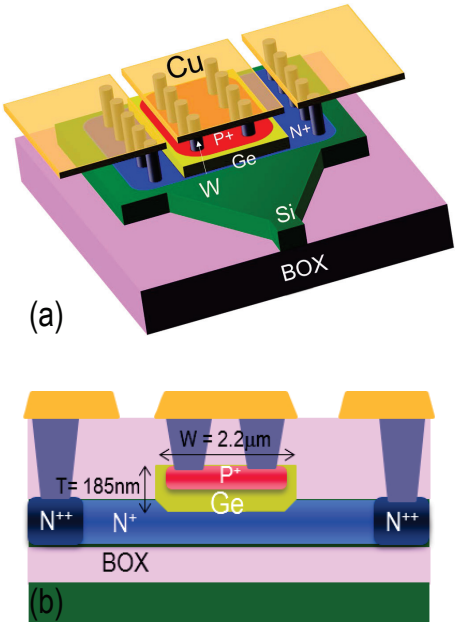

Figuur 12: (a) 3-D schematisch diagram van een VPIN GePD. (b) schematische dwarsdoorsnede van een VPIN GePD.

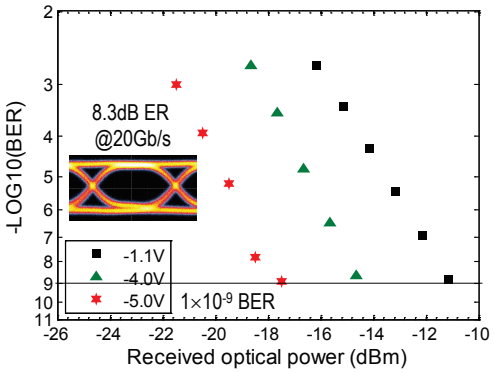

Figuur 13: BER bij 20 Gbps als functie van het optische ingangsvermogen gebruik makend van een $(2^{31}-1)$ lang NRZ PRBS patroon bij 1310 nm. De inset toont het 20 Gbps oogdiagram van het optisch ingangssignaal (extinction ratio 8.3 dB).

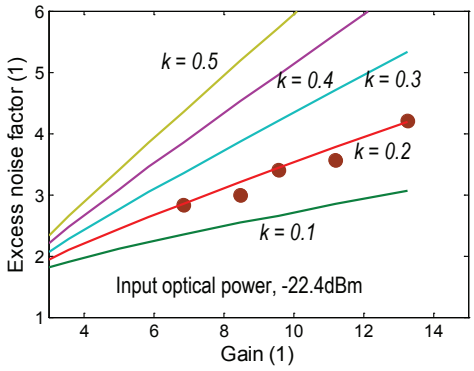

Figuur 14: De excess ruisfactor als functie van de avalanche-versterking bij een optisch ingangsvermogen van -22.4 dBm.

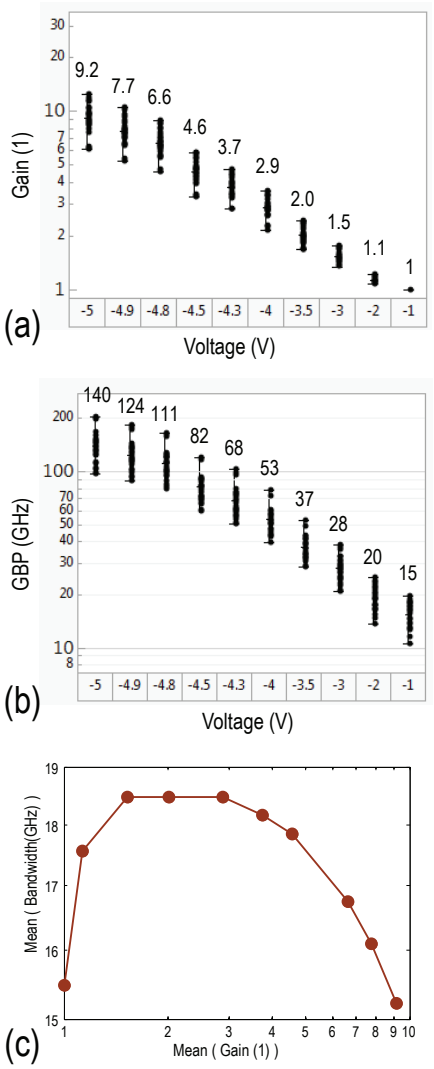

Figuur 15: (a) waferschaal avalanche-versterking data geëxtraheerd van de kleinsignaalmetingen voor verschillende biasspanningen. (b) waferschaal winst-bandbreedteproduct data. (c) gemiddelde 3dB bandbreedte als functie van de gemiddelde avalanche-versterking.

English summary

1 Si photonics optical interconnects

According to a Cisco Global Cloud Index 2014-2019 White Paper, annual global data center IP traffic will reach 10.4 zettabytes by the end of 2019. This is mainly driven by growing multimedia services, Video On Demand, HD television, and the increasing amount of internet users. More than 86 percent of workloads will be processed by cloud data centers, and by 2019, 56 percent of the cloud workloads will be in public cloud data centers, up from 30 percent in 2014.

Large data centers are required with thousands of servers interconnected with high bandwidth switches. Optical interconnects is a promising solution offering high throughput, low latency and reduced energy consumption compared to current networks. Si photonics is a promising technology to enable such optical interconnects by leveraging the mature CMOS manufacturing facilities to provide compact and low-cost integrated optical circuits.

An optical transceiver is the key module in optical interconnects, which includes both a transmitter and a receiver in a single module. An on-off keying (OOK) 4-channel CWDM Si photonics optical transceiver was demonstrated by imec with a line rate of 20 Gbps, as shown in Fig. 16. It comprises of a 40 nm CMOS electrical transceiver flip-chip integrated on a 130 nm Si photonics optical interposer. The 130 nm Si photonics optical interposer consists of 4-channel micro-ring modulators, a 4-channel micro-ring WDM demultiplexer and 4-channel Ge p-i-n photodetectors. A fiber-to-chip grating coupler is used as the interface for coupling light from a single-mode optical fiber to a single mode Si waveguide. The high-speed optical signal generated from the transmitter is coupled into a single-mode fiber and transmitted over 2 km before being coupled into the receiver.

The power efficiency is the key performance metric of a Si photonic optical transceiver. For error-free transmission with a bit error ratio of 1×10^{-12}, the measured power efficiency of the Si photonics optical transceiver is 5.05 pJ/bit, and the laser consumes 35% of the power. This is because the laser has to provide a sufficiently high output power such that there is enough optical power detected by the optical receiver to overcome the electronic noise and the signal quality degradation for error-free reception. One effective approach to improve the power efficiency of the Si photonics optical transceiver is to increase the optical receiver sensitivity. Therefore, a smaller amount of optical power will be required at the optical receiver side for error-free reception, and so less optical power is required

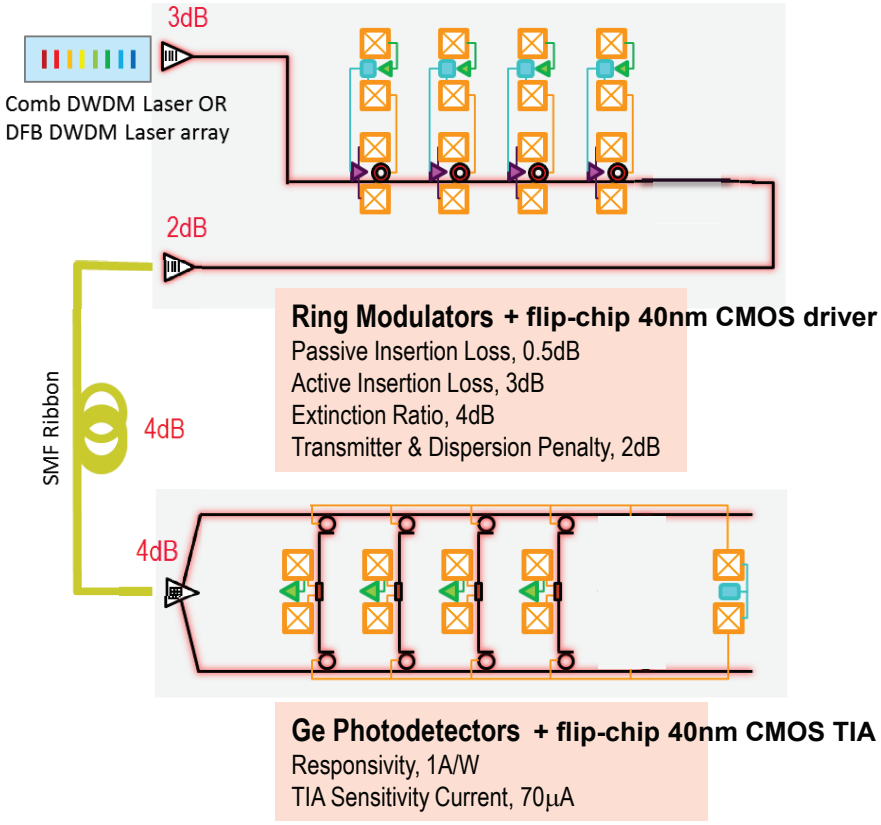

Figure 16: On-off keying 4×20 Gbps CWDM Si photonics optical transceiver demonstrated by imec.

from the transmitter side and thus from the laser. Assuming a 6 dB sensitivity improvement at the receiver side could lead to an overall 26% power efficiency improvement by solely reducing the power consumption by the laser.

In the optical domain, constructing such high-sensitivity optical receivers requires developing high performance p-i-n photodetectors and avalanche photodetectors. This is the motivation behind this PhD thesis.

2 Si-contacted Germanium p-i-n photodetectors

Conventional Ge waveguide p-i-n photodetectors require doping in Ge as well as a metal contact on Ge to form the p-i-n junction. Light absorption from the metal contacts on Ge is responsible for a substantial responsivity loss in these devices. In

addition, the process to form a metal contact to germanium is less well developed in standard CMOS foundries. The high contact resistance at the metal/Ge interface contributes to a large RC-constant, which normally determines the opto-electrical bandwidth of the Ge p-i-n photodetector. We demonstrated a Ge p-i-n photodetector without metal contacts on Ge, grown on and contacted through a silicon p-i-n diode structure, adopting a 400 nm thick Ge layer (referred to as Si-LPIN GePD hereafter), as shown in Fig. 17. It showed a high responsivity over 1 A/W across the whole C-band as shown in Fig. 18. The dark current is as low as 3 nA at -1 V bias. However, the 3-dB opto-electrical bandwidth of the device was transit-time limited to 20 GHz at -1 V bias at 1550 nm wavelength, as shown in Fig. 19.

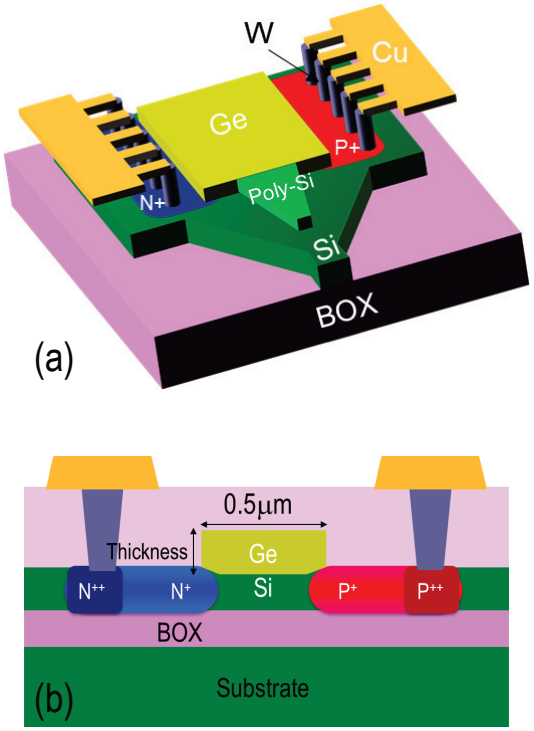

Figure 17: (a) 3-D schematic diagram of the Si-LPIN GePD. (b) Cross sectional schematic of the Si-LPIN GePD.

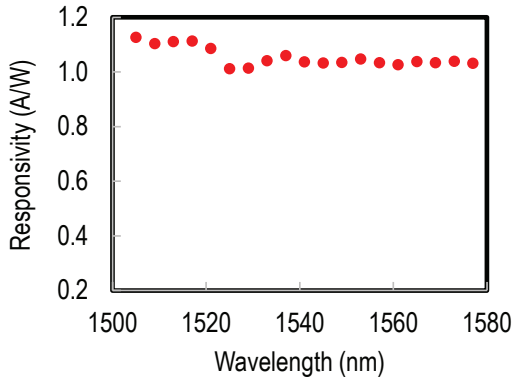

Figure 18: Responsivity as a function of wavelength in the C-band of the 400 nm Si-LPIN GePD at -1.2 V bias.

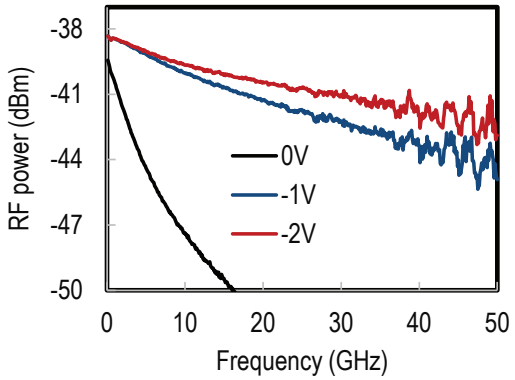

Figure 19: Small-signal transmission parameter (S_{21}) as a function of frequency of the 400 nm Si-LPIN GePD at 1550 nm wavelength.

By adopting a 160 nm thin Ge layer to reduce the transit time, the opto-electrical 3-dB bandwidth at -1 V was enhanced to 67 GHz and 44 GHz at 1550 nm and 1310 nm, respectively, for a 14 μm long Si-LPIN GePD. The S_{21} parameters measured at 1550 nm and the extracted 3-dB O/E bandwidth as a function of the waveguide-referred optical input power are shown in Fig. 20. The junction capacitance was 6.8 fF at -1 V, and the O/E bandwidth was still transit-time limited. Light coupling from the Si waveguide to the Ge waveguide is optimized by adding a poly-Si taper on top of the fully etched Si taper. The measured responsivity at -1 V was 0.74 A/W and 0.93 A/W at 1550 nm and 1310 nm respectively, as shown in Fig. 21. The dark current was as low as 4 nA at -1 V. 56 Gbps on-off keying

non-return-to zero data reception was demonstrated with clear open eye diagrams at both 1550 nm and 1310 nm wavelength. 80 Gbps and 100 Gbps on-off keying return-to-zero data reception using the 14 μm long Si-LPIN GePD was characterized, and clear open eye diagrams at 1550 nm wavelength were demonstrated. The eye diagrams captured in the 100 Gbps data reception experiment are shown in Fig. 22.

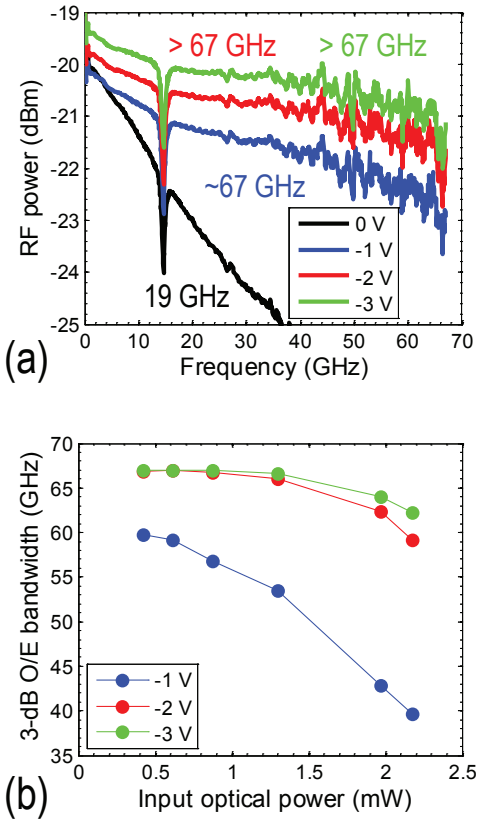

Figure 20: (a) Small-signal S_{21} transmission parameter as a function of frequency of the 160 nm Si-LPIN GePD at 1550 nm. (b) Measured 3-dB opto-electrical bandwidth as a function of input optical power at 1550 nm.

3 Low-voltage Germanium Avalanche photodetectors

A study to explore effective Ge APD designs compatible with the imec Si Photonics Platform was done, and a simple vertical p+(Ge)-i(Ge)-n+(Si) (VPIN) junction

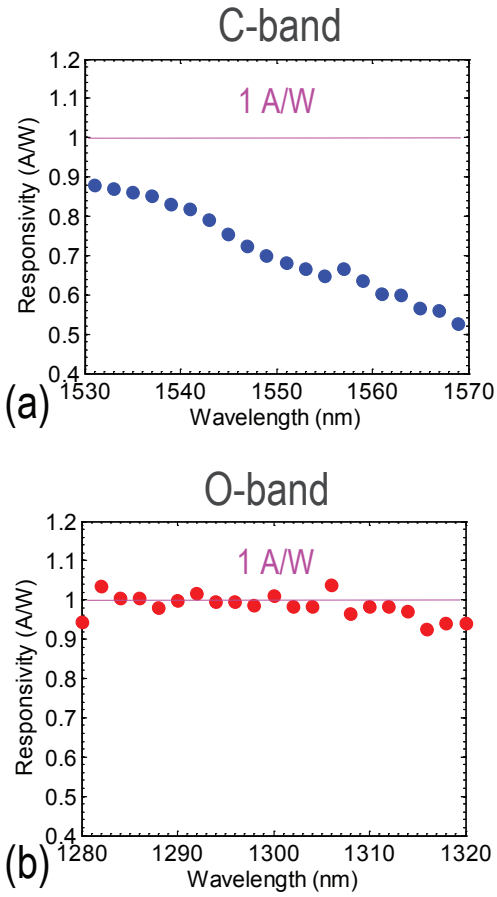

Figure 21: Responsivity as a function of wavelength of the 160 nm Si-LPIN GePD in (a) the C-band and (b) the O-band at -1.2 V bias.

proved to be an effective Ge APD design. This heterogeneous Ge/Si VPIN diode configuration adopting a 400 nm thick Ge layer, as shown in Fig. 23, results in a strong electric field as high as 1×10^5 V/cm confined to the lower 200 nm of the Ge layer at -5.5V bias voltage. Hence, it is expected that strong avalanche multiplication can take place at moderate applied bias voltage.

The demonstrated standalone Ge APD showed a 3-dB opto-electrical bandwidth above 10 GHz at an avalanche gain of 10.2 at -6.2 V, resulting in a gain$\times$bandwidth product (GBP) above 100 GHz, as shown in Fig. 24. It has a low dark current of 17 nA at -1 V and a high primary responsivity of 0.6 A/W. The measured effective ratio of ionization coefficients for electrons and holes (keff) was as low as 0.5,

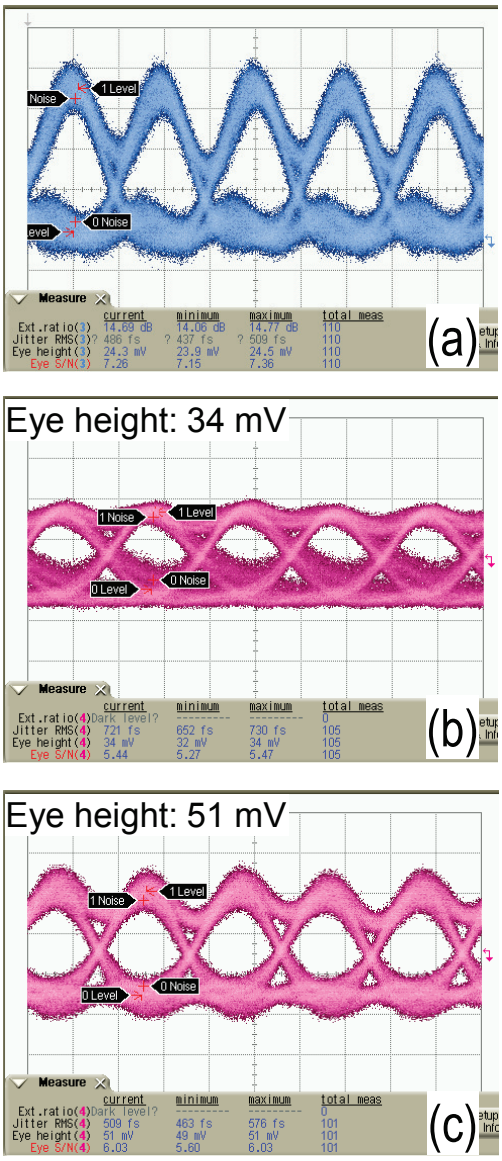

Figure 22: The 100 Gbps RZ eye diagram measured using (a) a 70 GHz commercial p-i-n photodetector (u2t XPDV 3120R), (b) the 160 nm Si-LPIN GePD at -1 V bias. (c) the 160 nm Si-LPIN GePD at -2 V bias.

as shown in Fig. 25. A significant sensitivity improvement of 5.8 dB at -5.9 V

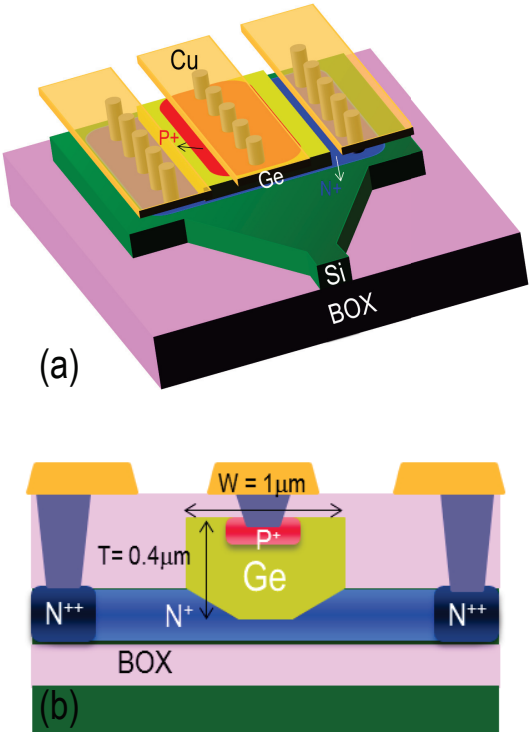

Figure 23: (a) 3-D schematic diagram of a VPIN GePD. (b) Cross sectional schematic of the VPIN GePD.

was demonstrated from bit error rate measurements on the wire-bonded optical receiver, as shown in Fig. 26. The primary sensitivity was -17.6 dBm and -18.6 dBm average optical power (non-return-to-zero modulation at 10 Gbps) at -1.7 V for a bit error rate of 1×10^{-12} and 1×10^{-9} respectively. This results in an absolute sensitivity in avalanche mode of -23.4 dBm and -24.4 dBm at a bit error rate of 1×10^{-12} and 1×10^{-12} respectively.

In order to increase the VPIN Ge APD performance, both the primary responsivity and the avalanche performance need to be improved. A thinner Ge layer (185 nm) was proposed to improve the avalanche performance under a lower operation voltage. To avoid excessive light absorption due to the metal contacts on top of Ge, a wider Ge layer of 2.2 μm is adopted with 2 metal contact plugs located away from the Ge layer center, as shown in Fig. 27.

A 20 Gbps 1310 nm optical receiver based on such a Ge APD is demonstrated showing a 6.2 dB avalanche sensitivity improvement at -5.0 V APD bias as shown in Fig. 28. A low effective k-value (the ratio of holes impact ionization rate to electrons impact ionization rate) of 0.2 is demonstrated from multiplication noise

measurements, as shown in Fig. 29. The wafer-scale mean gain×bandwidth product value is 140 GHz at -5 V bias voltage, as shown in Fig. 30.

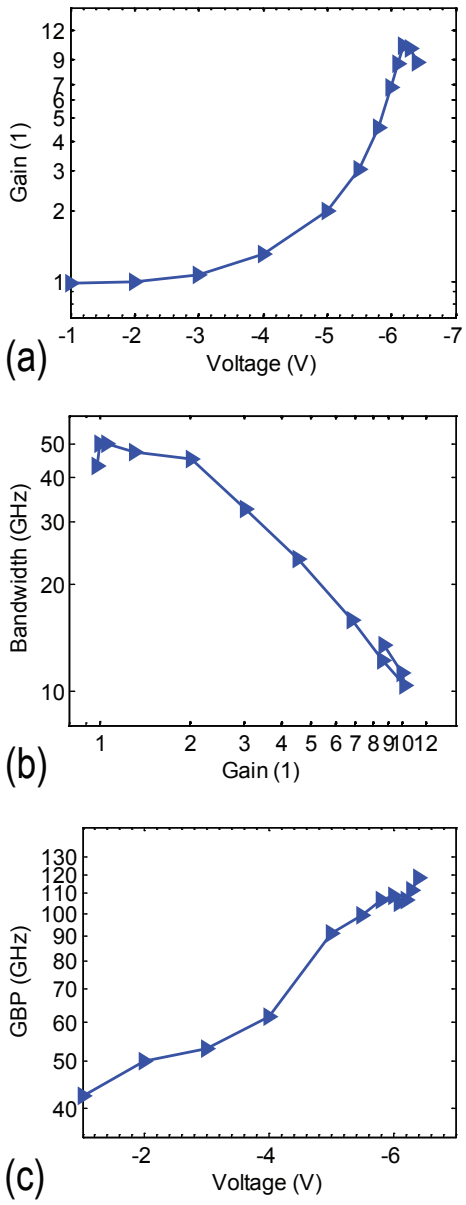

Figure 24: (a) Avalanche gain extracted from small-signal RF measurements as a function of bias voltage. (b) Measured 3dB opto-electrical bandwidth versus avalanche gain extracted from the S_{21} RF curves. (c) gain×bandwidth product as a function of bias voltage.

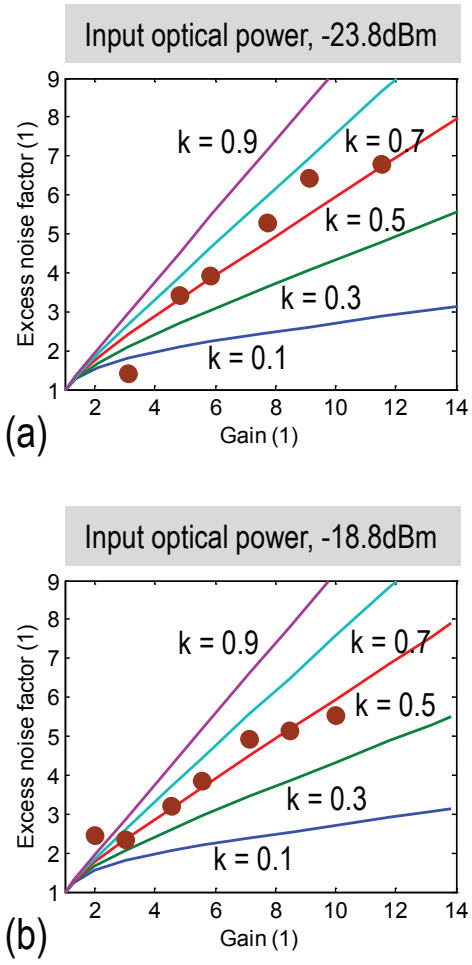

Figure 25: The excess noise factor as a function of gain with an input optical power of (a) -23.8 dBm and (b) -18.8 dBm.

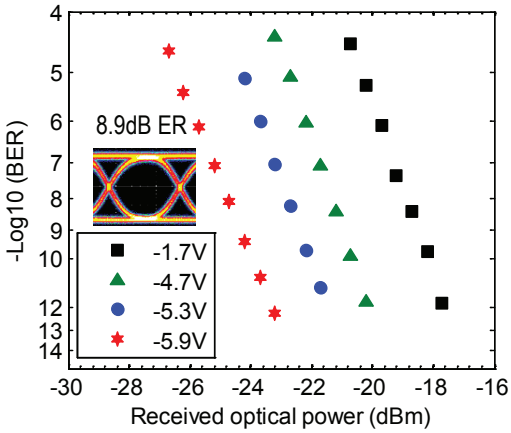

Figure 26: Measured bit error rate as a function of input optical power for various bias voltages.

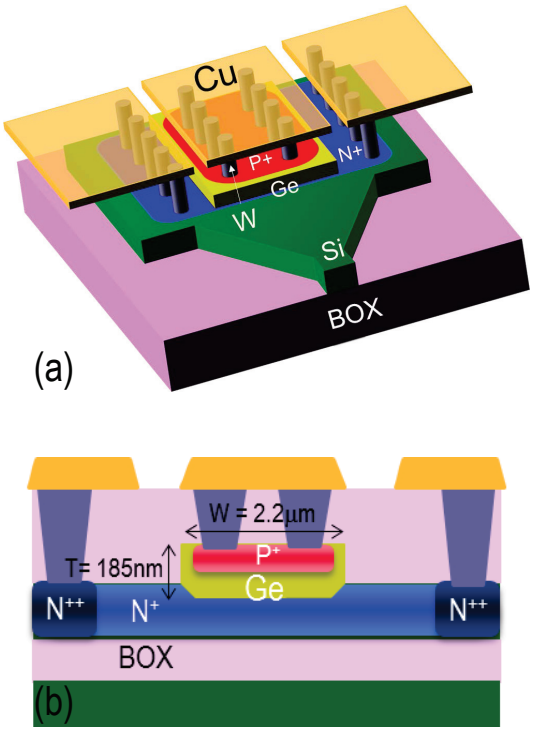

Figure 27: 3-D schematic diagram of a VPIN GePD.

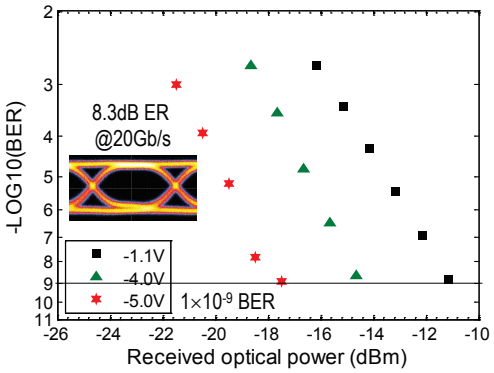

Figure 28: BER at 20 Gbps as a function of input optical power using a $(2^{31}-1)$ long NRZ PRBS pattern at 1310 nm. The inset shows the 20 Gbps optical input eye diagram with an extinction ratio of 8.3 dB.

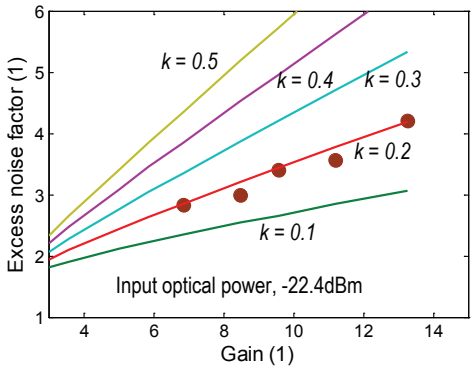

Figure 29: The excess noise factor as a function of avalanche gain for an input optical power of -22.4 dBm.

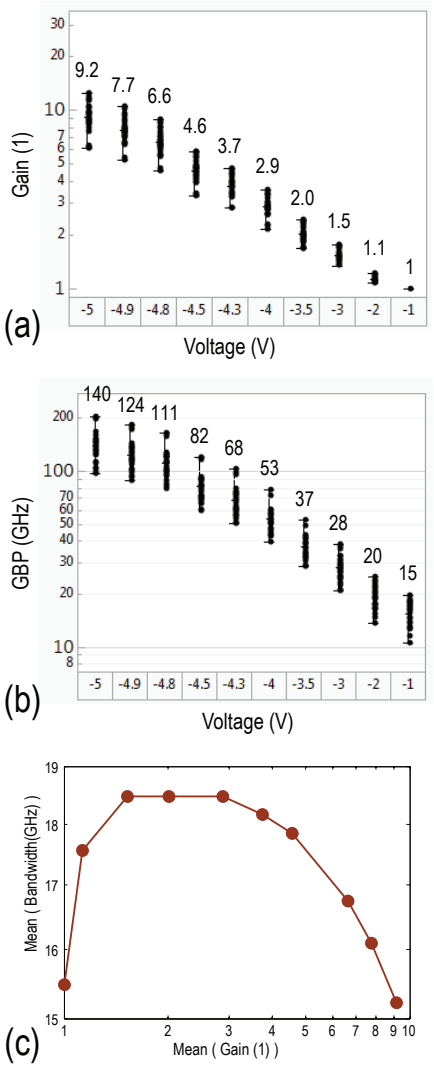

Figure 30: (a) Wafer-scale avalanche gain data extracted from the small-signal RF measurements for various bias voltages. (b) Wafer-scale gain×bandwidth product data. (c) The mean value of the measured 3-dB opto-electrical bandwidth data (at a given reverse bias) as a function of the mean value of avalanche gain data (at the same reverse bias) extracted from small-signal measurements.

1 Introduction

According to a Cisco Global Cloud Index 2014-2019 White Paper [1], annual global data center IP traffic will reach 10.4 zettabytes (863 exabytes [EB] per month) by the end of 2019, up from 3.4 zettabytes (ZB) per year (287 EB per month) in 2014. This is mainly driven by growing multimedia services, Video On Demand, HD television, and the increasing amount of internet users. More than 86 percent of workloads will be processed by cloud data centers, and by 2019, 56 percent of the cloud workloads will be in public cloud data centers, up from 30 percent in 2014 [1]. Large public data centers are required with thousands of servers interconnected with high bandwidth switches. Optical interconnects are emerging as a promising solution offering high throughput, low latency and reduced energy consumption compared to legacy electrical interconnects. Si photonics is a promising technology to enable such optical interconnects by leveraging the mature CMOS manufacturing facilities to provide compact, low-loss and low power consumption integrated optical circuits.

1.1 Optical Interconnects

Large data centers are required with thousands of servers interconnected with high bandwidth switches, as seen in Fig. 1 [2]. Optical interconnects are emerging as a promising solution offering high throughput, low latency and reduced energy consumption compared to legacy electrical interconnects [3]. In the current data centers, the optical interconnects providing the connection between clusters and

the switch (e.g. from Top of Rack Switch to Aggregation Switch, as shown in Fig. 2 [3]), are typically using the lowest-cost solution based on multi-mode fiber with simple but cheap VCSEL-based transceivers. The most widely employed IEEE 802.3 Ethernet standard for this short range (<500 m) is the 100GBASE-SR10 standard. This 100 Gbps standard makes use of 10 separate multi-mode fibers with each a 10 Gbps line rate (operating at 850 nm wavelength). Increasing the bandwidth using this standard (e.g. by using more transceivers in a certain rack) is limited by the available front panel area. Enough front panel area should be open for cooling fans. The increase in line rate from 10 Gbps to 25 Gbps could solve this front area limitation by using only 4 multi-mode fibers instead of 10 (IEEE standard 100GBASESR4). Besides, the required reach of optical interconnects increases due to the growing distance within a data center. Therefore, the newest data centers are upgrading their fiber network to more expensive transceivers but using lower-cost single-mode fiber. A single-mode fiber has a lower dispersion and therefore enables long reach. This upgrade implies the shift to longer wavelengths in the O-band for intra-datacenter links and in the C-band for inter-datacenter links.

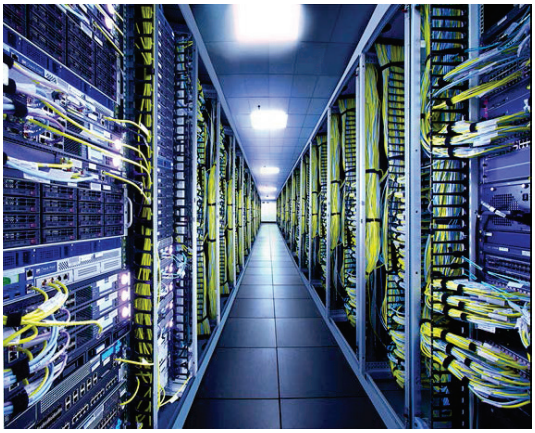

Figure 1.1: Optical interconnects used in the large data centers [2].

1.2 Silicon Photonics

Silicon photonics offers some unique advantages compared with other photonic technology, like InP photonics, $LiNbO_3$ photonics, and silica glass photonics. First, silicon, with a band gap near 1.12 eV, is transparent in the telecom C-band and O-band. The very high refractive index contrast between the silicon core ($\sim$3.45) and the surrounding silicon dioxide cladding ($\sim$1.45) enables optical modes to be strongly confined and guided in silicon waveguides. This very high

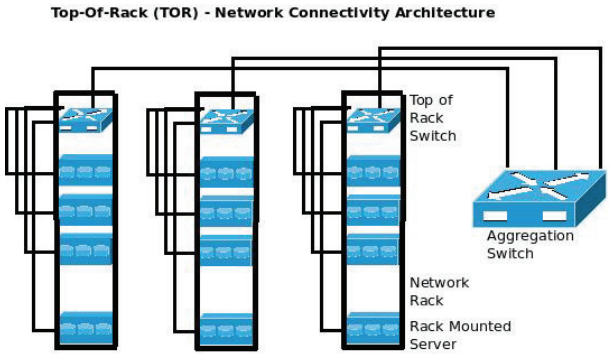

Figure 1.2: Interconnects inside a cluster through the Top of Rack Switch and among the clusters through the Aggregation Switch [3].

refractive index contrast allows passive silicon waveguide structures with cross-sectional dimensions of only a few hundred nanometers and single-mode waveguides to have a bending radius below 5 μm. A schematic of a silicon photonics waveguide is shown in Fig. 3. The waveguide consists of a silicon core and a silica cladding. Second, Si photonics allow optical devices to be made cheaply using standard semiconductor fabrication techniques and integrated with microelectronic chips.

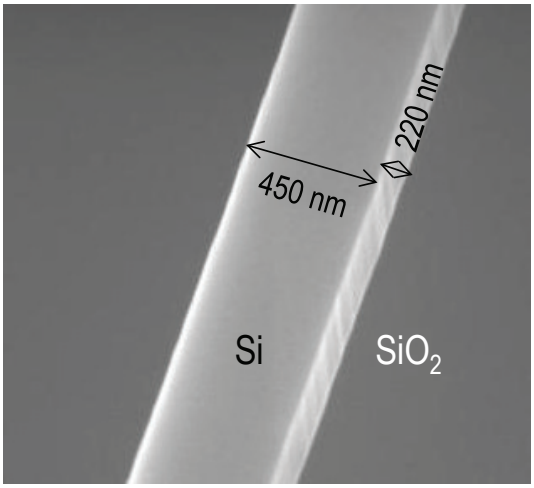

Figure 1.3: A Si photonics waveguide in the Si/SiO2 material system.

Although the linear electro-optic effects traditionally used in semiconductor

materials for electro-refraction are very weak in silicon, the free carrier plasma dispersion effect has been exploited to realize high-speed Si Mach-Zehnder and microring optical modulators [4–8].

As for the optical detection, germanium is selectively grown on Si to realize photodetectors. Selectively Ge epitaxy on Si has been reported with low threading dislocation density, and Ge p-i-n photodetectors have been reported with a 3-dB opto-electrical bandwidth over 40 GHz and a responsivity over 0.8 A/W [9–13]. For the optical source, heterogeneously integrating III-V on Si through wafer bonding and selectively growing III-V on Si to realize single-mode lasers have been reported [14–18].

imec Si Photonics Platform A good description of the imec Si photonics platform can be found in [19], which is summarized as follows. It starts from 200 mm silicon-on-insulator (SOI) wafers with a nominal Si thickness of 220 nm on top of a 2 μm buried oxide. The top Si layer is etched to 3 depths using three 193 nm lithography levels: full etch, a 70 nm shallow etch, and a 150 nm deep etch. Afterwards, a high density plasma (HDP) oxide is deposited to fill narrow trenches. This HDP oxide is then polished using chemical-mechanical polishing (CMP), selective to the hard-mask used to pattern the three levels. This realizes the imec Si photonics Passive-Platform technology as shown in Fig. 4 [20].

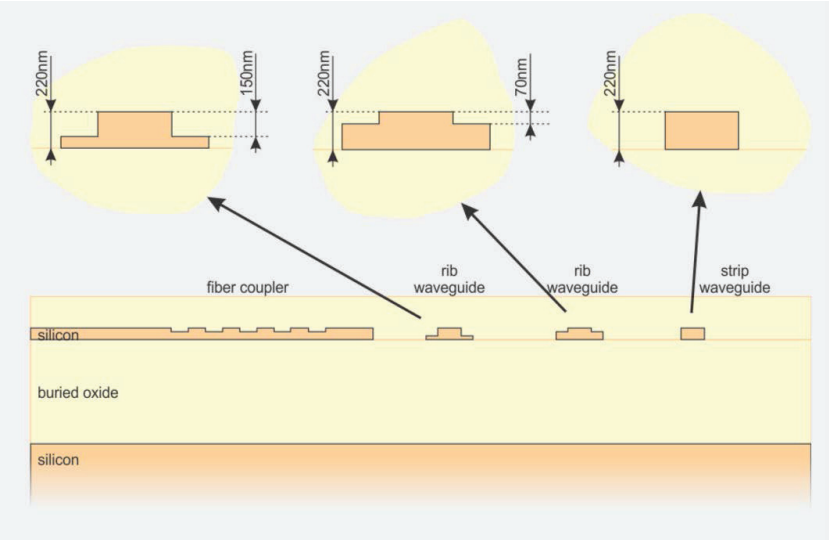

Figure 1.4: imec Si photonics Passive-Platform technology [20].

This Passive-Platform technology creates a flat starting surface for the ad-

vanced passives levels. It consists of a gate oxide grown on top of the exposed Si layer followed by a 160 nm poly Si layer deposition. This 160 nm poly Si layer is patterned using 193 nm lithography. Similar to the first three etches in Si, a HDP oxide is used to fill the narrow trenches, and a similar CMP process is used to planarize the oxide. The Si is then doped using three n-type and three p-type implant levels. The poly Si is doped using two additional implant steps. Both the Si and poly-Si implantations are annealed using a spike anneal at 1075°C.

The Ge mesas are then selectively grown in trenches formed on top of the Si layer, followed by a Ge CMP step. Both n-type and p-type implants are available for the planarized Ge. The Ge junctions are annealed at 550°C. The contact regions on top of Si and poly-Si are selectively silicided using a local Ni-silicidation process.

The germanium epitaxy details can be found in [21] and is summarized here. The germanium is grown in a vapor phase epitaxy (VPE) reactor. H_2 and N_2 carrier gases have a typical flow of 20-50 standard liters per minute, and 1% GeH_4 diluted in H_2 is used as the Ge precursor. 200 mm Si (001) wafers are cleaned with imec clean mixture followed by 30 s dip in 2% hydrofluoric acid (HF) to remove the chemical oxide. The wafer is then dried with isopropanol to remove any water residue. Next, the wafer is purged in N_2 for 60 min. Before the Ge growth, the Si wafer receives a bake at or above 850°C in H_2 ambient to remove remaining native oxide on the Si surface. The Ge growth temperatures vary from 350°C up to 600°C. The Ge growth conditions are 450°C at 760 Torr with GeH_4 partial pressure of 0.3 Torr, which gives a growth rate of 30 nm/min on blanket Si (001) substrates and the root mean square (RMS) roughness of $\sim$ 1 nm for 1 μm thick Ge layers.

The back-end of line process uses a 1μm PMD stack on top of the silicon waveguides, and W plugs to create the electrical contacts to the silicide on the highly doped Si, poly-Si and Ge. On top of the PMD stack, the W heaters are formed, after which a Cu metal is introduced. This realizes the imec Si photonics Full-Platform technology as shown in Fig. 5 [24], and more info on this platform can be found in [20, 22–25].

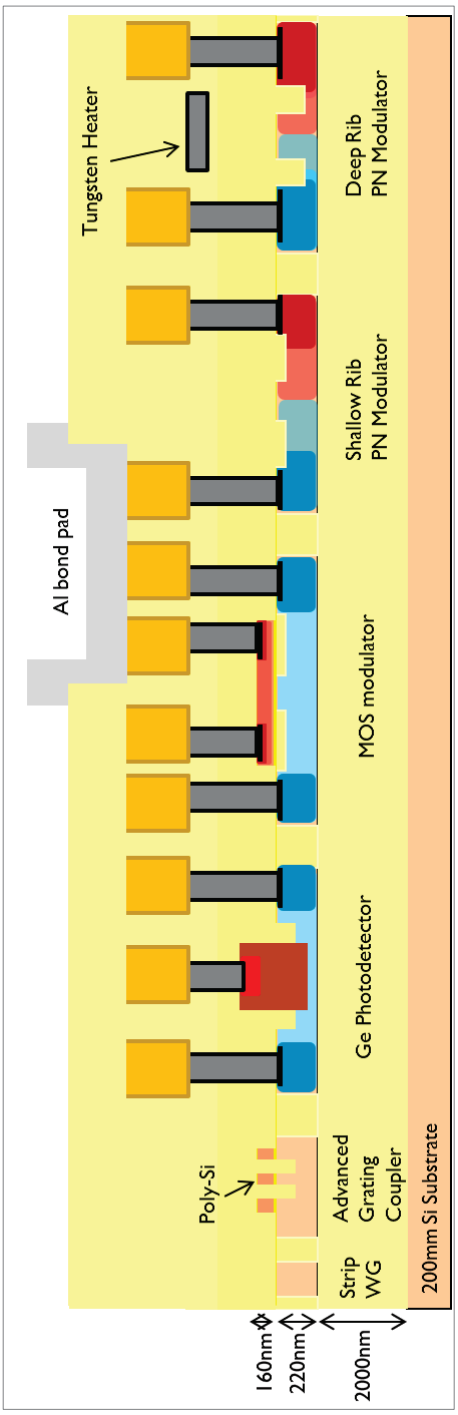

Figure 1.5: imec Si Photonics Full-Platform technology [24].

1.3 Optical transceivers

Fiber optic data links work similar to the diagram shown in Fig. 6(a). They consist of a transmitter on one end of a fiber and a receiver on the other end. Most systems operate by transmitting in one direction on one fiber and in the reverse direction on another fiber for full duplex operation.

Most systems use an ”optical transceiver” which includes both a transmitter and receiver in a single module, as shown in Fig. 6(b). The transmitter takes an electrical input and converts it to an optical output from a laser diode or LED. The light from the transmitter is coupled into the fiber with a connector and is transmitted through the fiber optic cable plant. The light from the end of the fiber is coupled to a receiver where a detector converts the light into an electrical signal, which is then conditioned properly for use by the receiving equipment. Fig. 6(c) illustrates a commercial optical transceiver showing the functional units in a standard form factor.

1.3.1 Si photonics optical transceiver

An on-off keying (OOK) 4-channel CWDM Si photonics optical transceiver was demonstrated by imec with a line rate of 20 Gbps [26], as shown in Fig. 7. It comprises of a 40 nm CMOS electrical transceiver flip-chiped on a 130 nm Si photonics optical interposer. The 130 nm Si photonics optical interposer consists of 4-channel micro-ring modulators, a 4-channel micro-ring WDM demultiplexer and 4-channel Ge p-i-n photodetectors. A fiber-to-chip grating coupler is used as the interface for coupling light from a single-mode optical fiber to a single mode Si waveguide. The high-speed optical signal generated from the transmitter is coupled into a single-mode fiber and transmitted over 2 km before being coupled into the receiver. The TE polarization and TM polarized light is coupled into two orthogonal single mode waveguide using a 2-D grating coupler. Both the TE and TM polarization of the optical signal go through a 4-channel micro-ring WDM demultiplexer, and the TE and TM component in the same channel are fed to the 2 ports of one Ge p-i-n photodetector.

The key performance metrics of the optical components used in this Si photonics optical interposer were annotated in Fig. 7. A complete set of performance metrics of the optical components in the process design kit (PDK) provided by the imec Si photonics Full-Platform can be found in [24].

1.3.2 Power efficiency of the Si photonics optical transceiver

The power efficiency is the key performance metric of a Si photonic optical transceiver. The power efficiency can be grouped into 4 parts: the power consumed by the RF

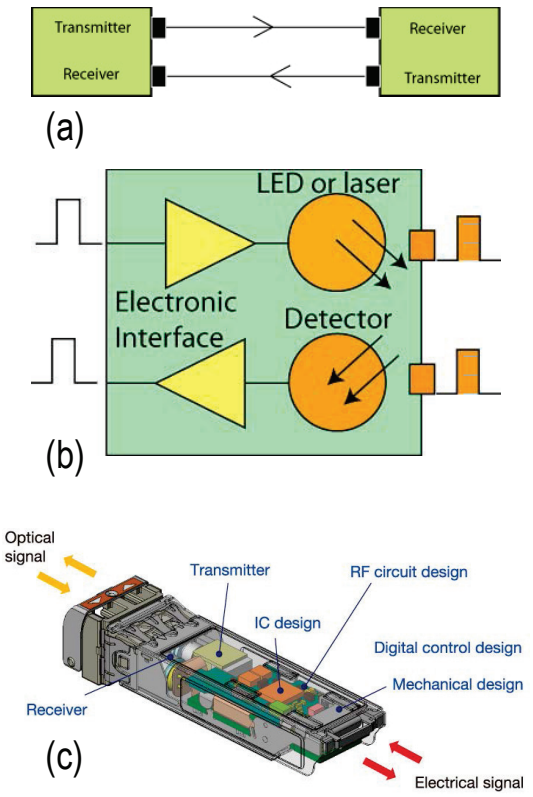

Figure 1.6: (a) A typical fiber optic data link. (b) The functional block diagram of a fiber optical transceiver. (c) A commercial optical transceiver cartoon showing the functional units in a standard form factor.

drivers in the optical transmitter, the power consumed by the trans-impedance amplifiers (TIAs) in the optical receiver, the power consumed by the laser providing the CW light to the optical transmitter, and the power consumed by the micro heaters for the thermal control. For error-free transmission with a bit error rate of 1×10^{-12}, the measured power efficiency of the Si photonics optical transceiver is shown in Fig. 8. The total power efficiency is 5.05 pJ/bit, and laser consumes 35% of the power. This is larger than that consumed by the RF drivers, the TIAs, and the micro heaters. This is because the laser has to provide a sufficiently high output power such that there is enough optical power detected by the optical receiver to overcome the electronic noise and the signal quality degradation for error-free reception.

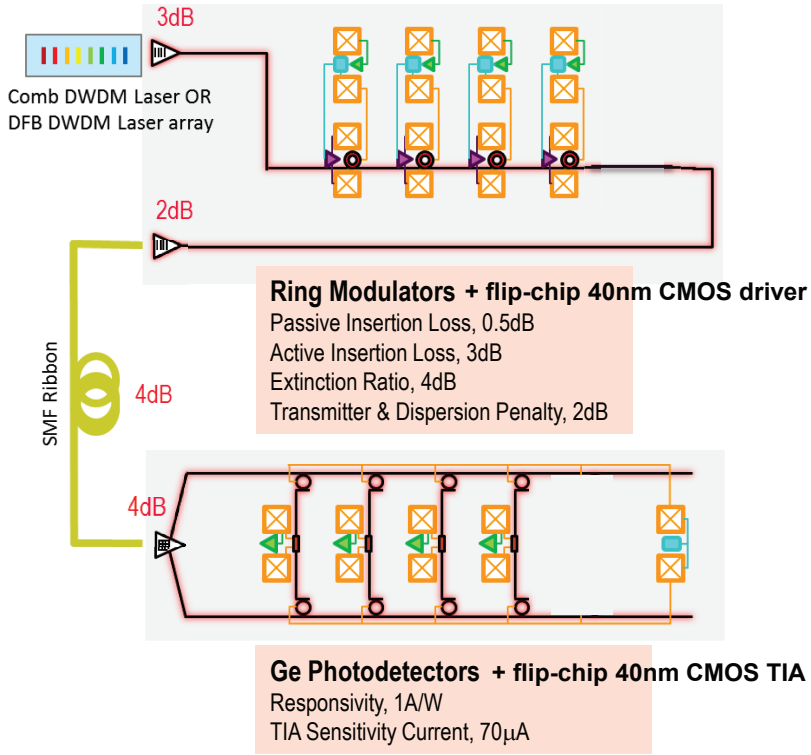

Figure 1.7: On-off keying 4×20 Gbps CWDM Si photonics optical transceiver demonstrated by imec [26].

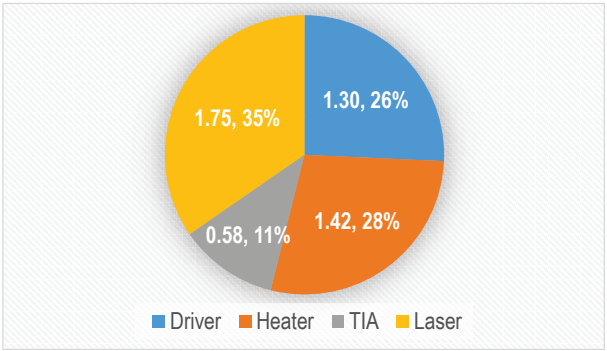

Figure 1.8: power efficiency of the on-off keying 4λ×20 Gbps CWDM Si photonics optical transceiver. unit: pJ/bit

RF driver The optical modulation process in the transmitter can be interpreted as a charging/discharging of the modulator seen as a capacitor by the RF driver. The power consumption of the optical transmitter (RF driver) can be roughly estimated by Eq. 1 , where P_{drv} represents the driver power consumption (without any load) required to buffer (strengthen) the input data stream in order to provide the required peak-to-peak voltage (V_{pp}) to the optical modulator with a load C_{mod} at the modulation speed (*BR*). The second part of this equation describes the power consumed by the modulator.

$$P_{Tx} = P_{drv} + C_{mod} \cdot V_{pp}^2 \cdot (BR/2) \tag{1.1}$$

TIA The power consumption in an optical receiver is mainly the power consumed by the TIA to provide a large trans-impedance gain converting the weak current signal to a voltage signal that can be detected by the decision circuit.

Laser The power consumption of the laser (P_{laser}) can be determined from its output power (P_{out}) and its wall-plug efficiency (η) as in Eq. 2.

$$P_{laser} = P_{out}/\eta \tag{1.2}$$

Thermal control Both the micro-ring modulators and micro-ring WDM demultiplexer are thermal and process sensitive, and they need to be thermally controlled to operate. This is achieved using a tungsten heater to tune the temperature of the micro-rings to compensate the process and the ambient temperature variations. The power consumed by this thermal control (P_T) can be calculated as the product of the bias voltage applied on the heater (V_T) and the current flow through the heater (I_T), as in Eq. 3.

$$P_T = V_T \cdot I_T \tag{1.3}$$

1.3.3 Improving the power efficiency by leveraging a high sensitivity optical receiver

The design target for the power efficiency of the Si-photonics optical transceiver is 1 pJ/bit [27]. One effective approach to improve the power efficiency of the Si photonics optical transceiver, as shown in the pie chart in Fig. 9, is to increase the optical receiver sensitivity. Therefore, a smaller amount of optical power will be required at the optical receiver side for error-free reception, and so less optical power is required from the transmitter side and thus from the laser. Assuming a 6 dB sensitivity improvement at the receiver side could lead to an overall 26% power efficiency improvement by solely reducing the power consumption by the laser.

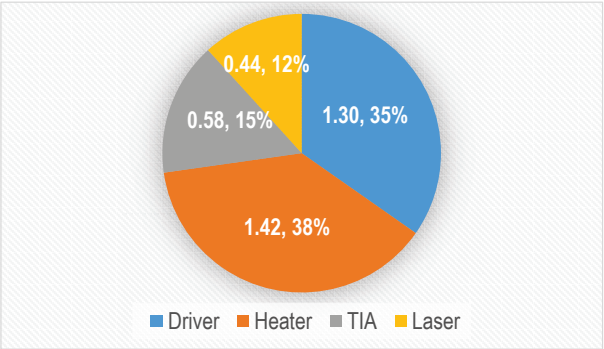

Figure 1.9: power efficiency of the Si photonics optical transceiver assuming a 6 dB sensitivity improvement at the receiver side.

In the optical domain, constructing such high-sensitivity optical receivers require high performance photodetectors (high bandwidth, high responsivity and low dark current). This is the motivation behind this PhD thesis.

1.4 Germanium waveguide photodetectors

The strong optical absorption of germanium in the fiber optics telecommunication window (C-band and O-band), as seen in Fig. 10 [28] makes it suitable for highly sensitive near-infrared optical detectors. In the past fifteen years, the use of Ge in optical detector applications has focused on hetero-epitaxial growth of Ge on silicon.

1.4.1 Ge p-i-n photodetectors

A 3-D cartoon of a waveguide Ge p-i-n photodetector is shown in Fig. 11. Incident light is coupled from a single-mode Si waveguide to the Ge waveguide using a Si waveguide taper. The active region is a p-i-n diode consisting of an intrinsic (I, i.e., undoped) region in between a P+ and an N+-doped region. Most of the photons are absorbed in the intrinsic region. A bias voltage is applied on the p-i-n diode, and the generated photo-carriers are efficiently collected by drifting along the built electric field, contributing to an external photocurrent, as schematically shown in Fig. 12 [29].

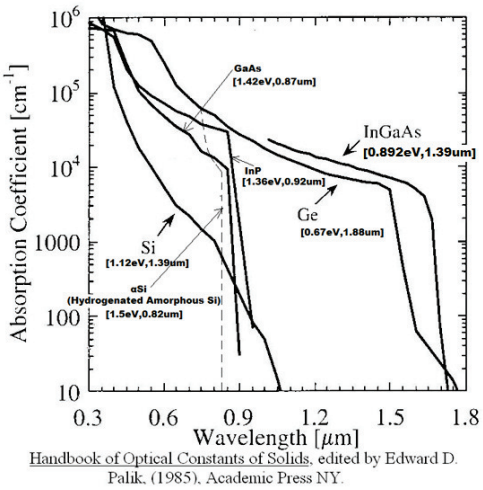

Figure 1.10: Optical absorption coefficient of common semiconductors [28].

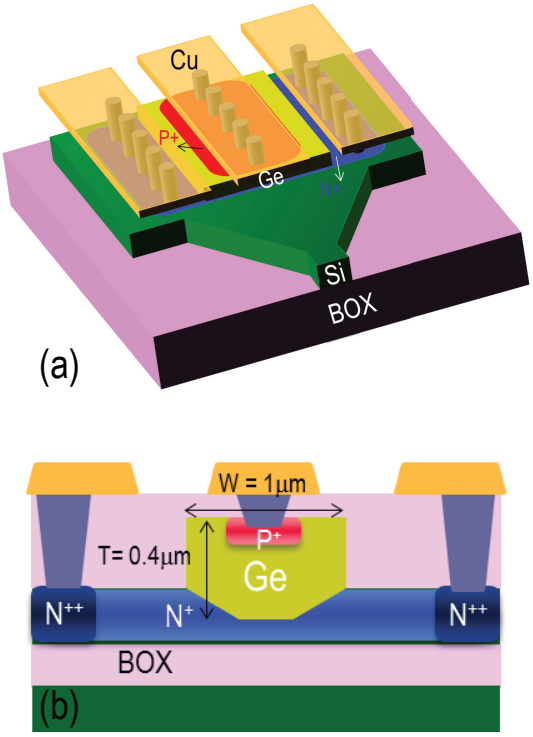

Figure 1.11: (a) A 3-D cartoon of a waveguide Ge-on-SOI photodetector. (b) Cross sectional schematic of the photodetector.

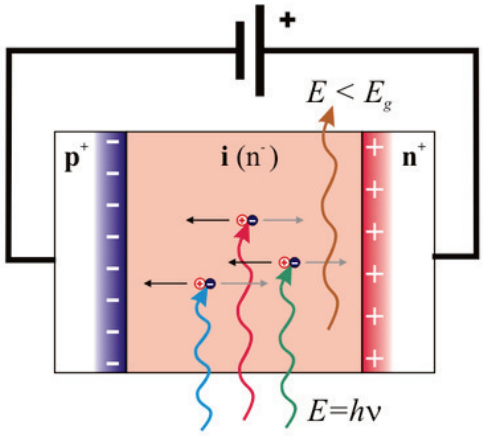

Figure 1.12: The schematic diagram illustrating light absorption and generated photo-carriers collection in a p-i-n photodiode [29].

1.4.1.1 Performance metrics

The performance metrics of a Ge waveguide p-i-n photodetector are responsivity (R), response speed, dark current (I_D) and operation voltage. An ideal Ge waveguide p-i-n photodetector has a high responsivity, a high response speed and a low dark current operating at a low bias voltage.

Responsivity Responsivity represents the capability of a p-i-n photodetector to convert an optical signal into an electric current (known as a photocurrent). It is defined as the ratio of the generated photocurrent and incident optical power, determined in the linear region of the response [30]. A related figure of merit is quantum efficiency, defined as the converted electron to incident photon ratio. In the wavelength region where the photon energy is somewhat above the Ge bandgap energy, responsivity can be expressed as in Eq. 4,

$$R = \eta \cdot \frac{q}{hf} \tag{1.4}$$

where hf is the photon energy, η is the quantum efficiency, and q the elementary charge. The calculated responsivity as a function of wavelength assuming a unit quantum efficiency is shown in Fig. 13.

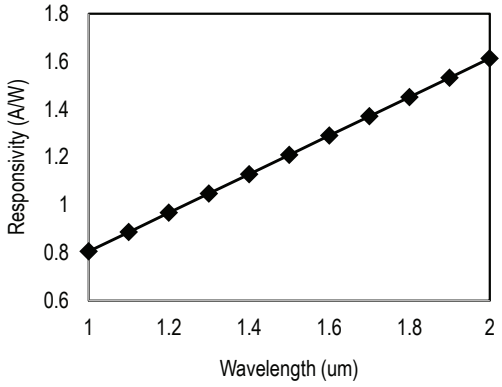

Figure 1.13: Responsivity as a function of wavelength assuming unit quantum efficiency.

Response speed Response speed represents the capability of a p-i-n photodetector to respond to a fast modulated optical signal. The figure of merit is the 3-dB opto-electrical bandwidth (f_{3dB}), which is determined by a combination of 3 factors, i.e., RC-constant, photo- carrier transit time, and diffusion of the generated photo-carriers.

Dark current Dark current is the small electric current that flows through a p-i-n photodetector when no photons are entering the device. This small electric current is due to the random generation of electrons and holes within the depletion region of the device. This charge generation rate is related to specific crystallographic defects within the depletion region, which is created in the Ge epitaxy on Si due to the 4% lattice mismatch.

Operation voltage A bias voltage builds an electric field in the depletion region that sweeps out all the photo-carriers within their lifetime, and thus the photodetector is able to respond to a fast-modulated optical signal. The operation voltage of a Ge p-i-n photodetector is generally required to be around -1 V for CMOS compatibility.

1.4.1.2 State of the art

Ge waveguide p-i-n photodetectors integrated on the Si photonics platform have been studied extensively, and various device structures have been developed [9–13, 31–39]. Fig. 14 summarizes the state of the art Ge p-i-n photodetectors that have been reported, in which responsivity versus the 3-dB O/E bandwidth and dark current versus the 3-dB O/E bandwidth are shown separately. Intel reported

the first Ge (vertical) p-i-n photodetector with a dark current lower than 1 μA [31]. This evanescently coupled p-i-n photodetector adopts a Ge layer of 0.8 μm thick, 7.4 μm wide and 50 μm long, showing a 3-dB O/E bandwidth of 31.3 GHz with a responsivity of 0.89 A/W at 1550 nm at -2 V bias. Kotura reported a butt-coupled horizontal p-i-n Ge photodetector integrated with a large cross-section SOI waveguide [32]. The photodetector has an active area of 0.8 μm$\times$10 μm, showing a 3-dB O/E bandwidth more than 32 GHz and a responsivity of 1.1 A/W at 1550 nm at -1 V bias. LETI reported a butt-coupled vertical p-i-n Ge photodetector adopting a 0.4 μm thick, 3μm wide and 15 μm long Ge layer [9]. The 3-dB O/E bandwidth is 42 GHz with a responsivity of 1A/W at 1550 nm at -4 V bias. Sandia National Laboratory reported an evanescently coupled Ge (vertical) p-i-n photodetector adopting a compact 1.3 μm$\times$4 μm Ge layer showing ultralow dark current of 3 nA [11]. The 3-dB O/E bandwidth is 45 GHz with a responsivity of 0.8 A/W at 1550 nm at -2 V bias. Kotura reported an evanescently coupled Ge (vertical) p-i-n photodetector on a 0.25 μm SOI platform with optimized metal contacts layout on Ge improving the responsivity to 0.95 A/W at 1550 nm [10]. The 3-dB O/E bandwidth is 36 GHz at -1 V bias. Luxtera reported design improvements for evanescently coupled Ge (lateral) p-i-n photodetectors [34]. Such a 10 μm long photodetector achieves $>$0.8 A/W responsivity over the entire C-band at -1 V bias, with a device capacitance of $<$7 fF. The University of Delaware reported a Si-contacted evanescently coupled lateral p-i-n Ge photodetector [37]. The metal contacts on Ge were removed, and the photodetector shows a very high responsivity of 1.14 A/W with a 3-dB O/E bandwidth of 20 GHz at 1550 nm at -4 V bias. UC Berkeley reported a novel waveguide coupling scheme where a Ge diode grown via rapid melt growth is wrapped around a silicon waveguide [39]. A 4 fF PIN photodiode is demonstrated with 0.95 A/W responsivity at 1550 nm, 6 nA dark current, and nearly 9 GHz bandwidth. IHP reported a Si-contacted evanescently coupled lateral p-i-n Ge photodetector integrated in a BiCMOS platform. The 3-dB O/E bandwidth is over 70 GHz and the responsivity is 1 A/W at 1550 nm, with a dark current of about 100 nA at -1 V bias [12].

It can be seen from Fig. 14 (a) that vertical p-i-n photodetectors [9–11] show a good responsivity and O/E bandwidth combination. the responsivity is over 0.8 A/W with the O/E bandwidth around 40 GHz. The lateral p-i-n photodetectors [32, 37] show a very high responsivity close to the quantum limit while the O/E bandwidth is relatively low, below 20 GHz.

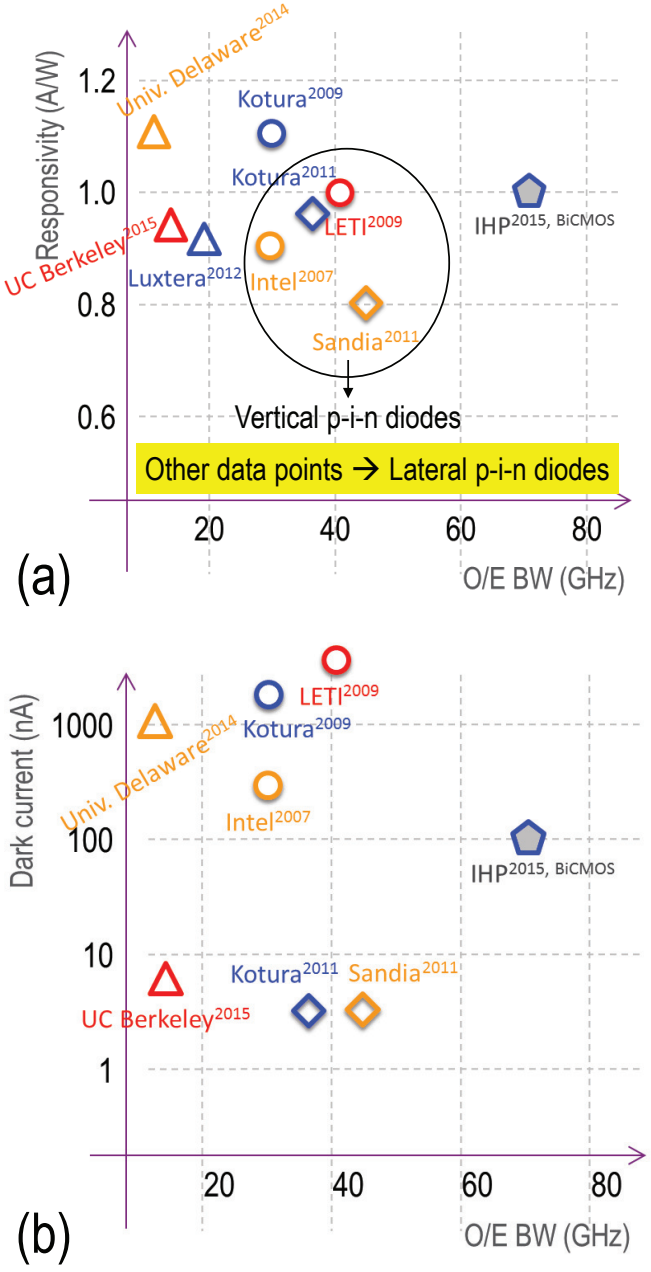

Figure 1.14: State-of-the-art of Ge p-i-n photodetectors. (a) Responsivity versus the 3-dB O/E bandwidth, and (b) dark current versus the 3-dB O/E bandwidth.

1.4.2 High-sensitivity optical receiver design

An optical receiver is schematically shown in Fig. 15 [40], which includes a photodetector, a TIA, a filter, a main amplifier (MA), and the following decision circuit. The sensitivity of an optical receiver is mainly determined by the photodetector and the TIA performance. The electrical signal generated by an optical receiver can be illustrated as in Fig. 16. I_1 and I_0 are the current generated by the p-i-n photodetector and entering the TIA at bit 1 and bit 0 level, respectively. The noise performance of the TIA is represented by an input-referred (RMS) noise current i_n. This i_n is defined such that, together with a noiseless TIA, it reproduces the output noise of the actual noisy TIA, as shown in Fig. 17 [40]. σ_1 and σ_0 are the standard deviation at bit 1 and bit 0 level respectively (assuming a normal distribution). This normal distribution results from the input-referred (RMS) noise current of the TIA and the shot noise current from the p-i-n photodetector.

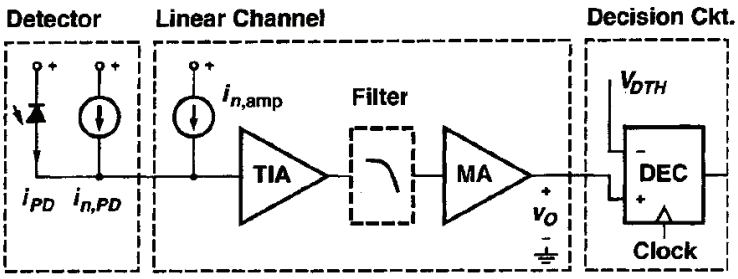

Figure 1.15: Basic optical receiver model [40]

The signal quality of the electrical data generated by an optical receiver can be theoretically calculated by the figure of merit, Q factor, as shown in Eq. 5. In the equation, $i_{S,1/0}$ is the shot noise current from a p-i-n photodetector at bit 1 and bit 0 level, respectively. i_n is the input-referred (RMS) noise current of the TIA. The relationship between Q factor and bit error rate, both characterizing the signal quality, is shown in Fig. 18. As for error-free reception with a bit error rate of 1×10^{-12}, the Q factor has to be $\sim$7.

$$Q = \frac{I_1 - I_0}{\sigma_1 + \sigma_0} = \frac{I_1 - I_0}{\sqrt{i_{s,1}^2 + i_n^2} + \sqrt{i_{s,0}^2 + i_n^2}} \tag{1.5}$$

p-i-n photodetector optical receiver The shot noise in the current generated by a Ge p-i-n photodetector is expressed in Eq. 6 for the bit 1 and bit 0 level, respectively. In the equation, q is the elementary charge and B is the noise bandwidth. The Q factor is derived from Eq. 5 to Eq. 7. In the equation, R is the responsivity

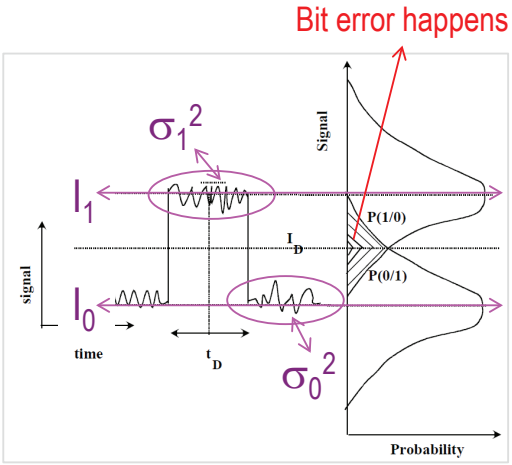

Figure 1.16: The schematic diagram illustrating the signal quality of the electrical data flowing out of an optical receiver.

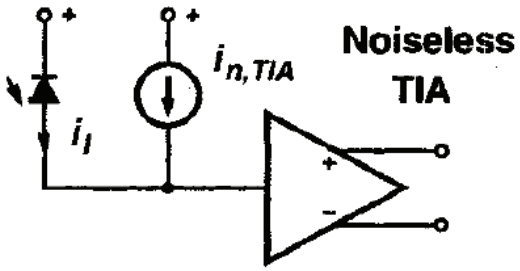

Figure 1.17: The schematic diagram illustrating the TIA input-referred (RMS) noise current definition [40].

of the p-i-n photodetector, P_1 and P_0 is the input optical power received by the Ge p-i-n photodetectors at bit 1 and bit 0 level, respectively. *B* is the noise bandwidth of the optical receiver, i_n is the input referred noise current of the TIA. It can be seen that, in order to achieve a higher sensitivity (that is a higher Q factor), the photodetector responsivity should be as high as possible.

$$i_{S,1/0} = \sqrt{2q \cdot I_{1/0} \cdot B} \tag{1.6}$$

$$Q = \frac{\sqrt{R} \cdot (P_1 - P_0)}{\sqrt{2q \cdot P_1 \cdot B + i_n^2/R} + \sqrt{2q \cdot P_0 \cdot B + i_n^2/R}} \tag{1.7}$$

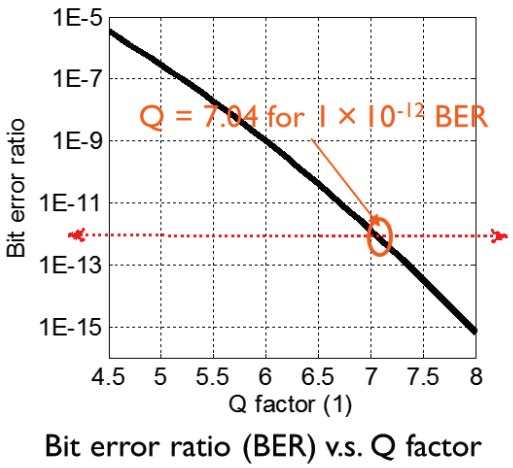

Figure 1.18: bit error rate as a function of the Q factor.

The dark current of the p-i-n photodetector was not considered in the above analysis. It should be low enough such that the shot noise in the dark current is well below the input-referred (RMS) noise current of the TIA (i_n), and thus it does not degrade the optical receiver sensitivity. The shot noise in the dark current, also governed by Eq. 6, was calculated as shown in Fig. 19(a) assuming a receiver bandwidth of 10 GHz. It can be seen that when this shot noise current becomes comparable to the input-referred (RMS) noise current of TIA, the optical receiver sensitivity starts to degrade, as shown in Fig. 19(b). The input-referred (RMS) noise current is assumed to 1 μA in this modeling. This sensitivity degradation occurs when the dark current gets larger than 10 μA, and thus the p-i-n photodetector dark current should be lower than this value.

The responsivity of a Ge p-i-n photodetector is not larger than 1.25 A/W at 1550 nm wavelength governed by the quantum limit. Assuming a TIA input-referred (RMS) noise current of 1 μA, which is a practical value for a 10 Gbps TIA, the highest achievable sensitivity at a bit error rate of 1×10^{-12} from the constructed optical receiver is $\sim$-21 dBm. In order to build an optical receiver with a higher sensitivity, either a semiconductor optical amplifier (SOA) is needed to optically pre-amplify the input optical signal or an avalanche photodetector is needed to electrically amplify the photocurrent to overcome the input-referred noise current in the TIA. As no SOAs are available on the Si photonics platform, leveraging the internal gain in Ge avalanche photodetectors is the only way to further enhance the optical receiver sensitivity, which will be introduced in the next section.

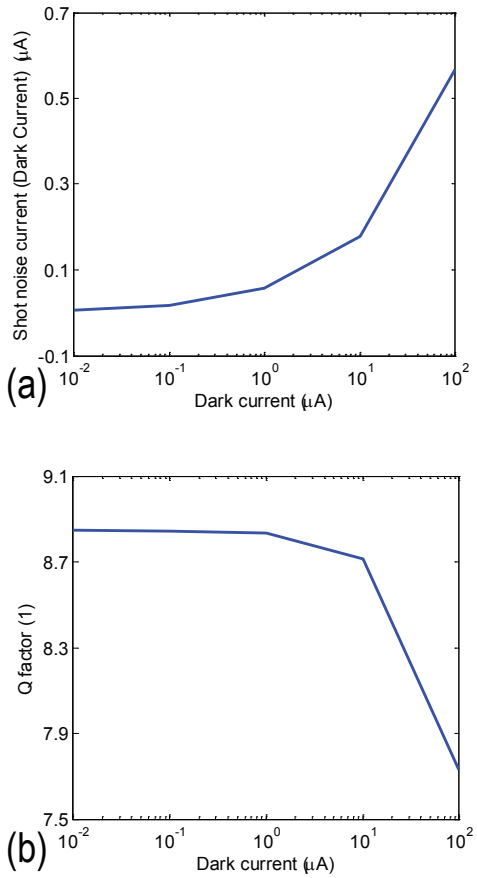

Figure 1.19: (a) Shot noise in the dark current, governed by Eq. 4. (b) Sensitivity degradation from the shot noise in the dark current.

1.4.3 Avalanche photodetectors

A Ge avalanche photodetector (APD) can be thought of as a photodetector that provides a built-in first stage of gain through avalanche multiplication over a Ge p-i-n photodetector [43]. It is normally operated at a high reverse bias voltage just below breakdown. In this regime, photo-carriers (both electrons and holes) are accelerated in the strong internal electric field and obtain high energy. These high-energy primary photo-carriers are able to generate secondary carriers through the impact ionization process, as shown in Fig. 20 [41]. Avalanche multiplication effectively amplifies the photocurrent by a significant factor that is the avalanche

gain. Therefore, avalanche photodetectors can be used for very sensitive detectors, which need less electronic signal amplification in the TIA and are thus less susceptible to electronic noise.

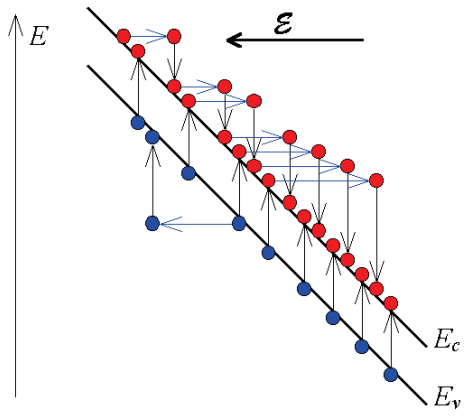

Figure 1.20: Schematic diagram illustrating the impact ionization process [41].

Compared to a Ge p-i-n photodetector, a Ge APD has a complex active region, as schematically shown in Fig. 21 [42]. This Ge/Si APD adopts a Separated-Absorption-Charge-Multiplication (SACM) structure, where the incoming light is absorbed in the absorption layer (Ge), and the generated photo-carriers are amplified in the multiplication layer (Si). The charge layer in between controls the electric field profile ensuring that there is a much stronger electric field confined in the multiplication layer than that in the absorption layer. Ge/Si SACM APDs leverage both the strong light absorption in Ge and the excellent low avalanche excess noise in Si, showing a very high sensitivity [44–47].

1.4.3.1 Performance metrics

A Ge APD has the same performance metrics of responsivity, response speed, dark current and operation voltage as those of a Ge p-i-n photodetector. Besides, it has 3 more performance metrics, i.e. avalanche gain, excess noise factor, and gain$\times$bandwidth product.

Primary responsivity Primary responsivity is the responsivity when a low bias is applied to a Ge APD and no avalanche multiplication occurs. In this regime, a Ge APD operates as a Ge p-i-n photodetector.

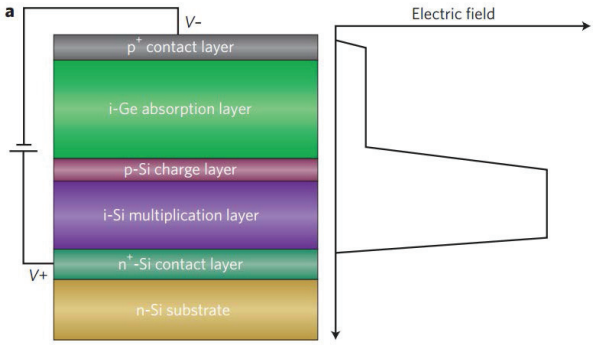

Figure 1.21: Schematic diagram of a SACM Ge/Si APD and the electric field profile [42].

Avalanche gain Avalanche gain is the multiplication factor of the avalanche multiplication amplifying the photocurrent when a high bias is applied to a Ge APD.

Dark current Similar to that of a Ge p-i-n photodetector, dark current is the electric current that flows through a Ge APD when no photons are entering the device. Avalanche multiplication amplifies dark current as well as the photocurrent, and thus there can be a very large dark current flowing through a Ge APD.

Excess noise factor The excess noise factor is a measure of the noise generated in the avalanche multiplication compared to an ideal noiseless multiplier. Avalanche multiplication is stochastic in nature because every electron-hole pair generated at a given distance in the depletion region is independent and does not experience the same multiplication [49]. As the avalanche gain fluctuates, the mean-square value of the gain $< M^2 >$ is greater than the square of the mean $< M >^2$. The avalanche excess noise is characterized by a noise factor *F(M)* that is define as in Eq. 8:

$$F(M) = \frac{< M^2 >}{< M >^2} = \frac{< M^2 >}{M^2} \tag{1.8}$$

This avalanche excess noise factor strongly depends on the ratio of electron impact ionization coefficient to hole impact ionization coefficient (*k*-value) and on the low-frequency avalanche gain (*M*), as expressed in Eq. 9 [49]. The excess noise factor as a function of the (low-frequency) avalanche gain of common bulk semiconductors is shown in Fig. 22 [48]. It can be seen that, compared to that in bulk Ge and InP, the avalanche multiplication process in bulk Si generate a much

lower noise at the same multiplication gain. This makes Si an excellent material to construct an avalanche photodetector.

$$F = M[1 - (1 - k)(\frac{M - 1}{M})^2] \tag{1.9}$$

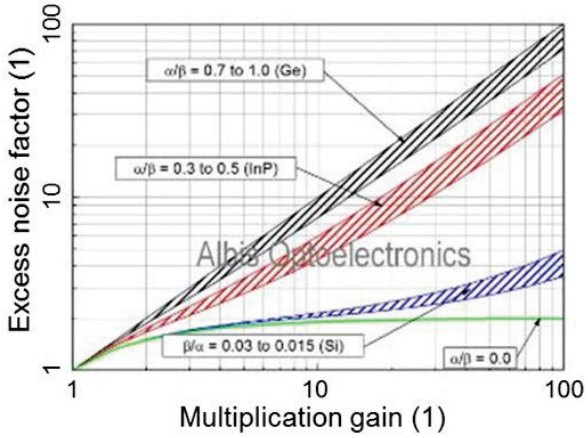

Figure 1.22: Excess noise factor as function of the avalanche gain of common semiconductors [48].

The total shot noise (including avalanche excess noise) $i_{S,1/0}$ in the current generated by a Ge APD is expressed in Eq. 10 at bit '1' and bit '0' level, respectively. In the equation, *q* is the elementary charge, *B* is the noise bandwidth, *F(M)* is the avalanche excess noise factor. The shot noise (avalanche excess noise) strongly depends on the *k*-value, as seen in Fig. 23(a) assuming a I_1 of 5 μA, a I_0 of 0.5 μA and a bandwidth *B* of 10 GHz.

$$i_{s,1/0} = \sqrt{2q \cdot I_{1,0} \cdot M^2 \cdot F(M) \cdot B} \tag{1.10}$$

The Q factor of the electrical signal generated by a Ge APD optical receiver is further derived in Eq. 11. In the equation, *R* is the primary responsivity, i_n is the input referred noise current of the TIA. When there is no avalanche gain in the Ge APD (operating at a low bias), it behaves as a Ge p-i-n photodetector. As the bias voltage is increased, the avalanche gain (*M*) amplifies the primary photocurrent, and the signal quality gets boosted (Q factor rises). However, as the avalanche gain further increases beyond a certain value, the signal quality degrades instead. This is because the avalanche multiplication amplifies the noise current as well as the signal current, and when the noise current becomes comparable to the input-referred (RMS) noise current of the TIA, the overall signal to noise ratio

of the electrical signal starts to fall, as seen in Fig. 23(b). Therefore, there is an optimal avalanche gain that can be leveraged to achieve the largest sensitivity improvement.

$$Q = \frac{R \cdot (P_1 - P_0)}{\sqrt{2q \cdot R \cdot P_1 \cdot F(M) \cdot B + i_n^2/M^2} + \sqrt{2q \cdot R \cdot P_1 \cdot F(M) \cdot B + i_n^2/M^2}} \tag{1.11}$$

Since the highest avalanche sensitivity improvement is obtained when the noise current generated from the avalanche multiplication gets comparable to the input-referred noise current of the TIA, a higher avalanche gain can be leveraged to boost the optical receiver sensitivity more for the case with a lower *k*-value than the case with a higher k-value, as seen in Fig. 23 (b). Therefore, in order to achieve a highly sensitive optical receiver, a low k-value together with a large avalanche gain are preferred.

Response speed At low bias voltages when there is no gain, similar to a Ge p-i-n photodetector, the 3-dB opto-electrical bandwidth of a Ge APD is determined by a combination of 3 factors, i.e., RC-constant, photo-carrier transit time, and diffusion of the generated photo-carriers. Besides, when the avalanche multiplication process is occurring, the avalanche build-up time is another factor limiting the O/E bandwidth. The regenerative avalanche process results in the presence of a large number of carriers in the high-field region long after the primary electrons/holes have traversed through that region [49]. The higher the avalanche gain is, the longer time it takes to build up the avalanche process, and when the light is switched off, the longer time the avalanche process persists. This avalanche build-up time normally becomes the main factor limiting the O/E bandwidth of a Ge APD when the avalanche gain gets larger than the reciprocal of the k-value. In this regime, the 3-dB O/E bandwidth drops inversely proportional to the avalanche gain as shown in Fig. 24 [49].

Gain·bandwidth product The linear region in Fig. 24 indicates that the product of the 3-dB O/E bandwidth and avalanche gain is constant in this regime. This gain·bandwidth product is a comprehensive figure of merit representing the avalanche performance of an APD.

Operation voltage Compared to a Ge p-i-n photodetector, a Ge APD normally operates at a much higher bias voltage to generate a strong internal electric field to initiate the avalanche multiplication process. A Ge p-i-n photodetector is required to operate at -1 V bias for CMOS compatibility. Ge APDs normally operate at a much higher bias voltage with strong electric field confined in the multiplication region to generate large avalanche gain. The design target is -5 V.

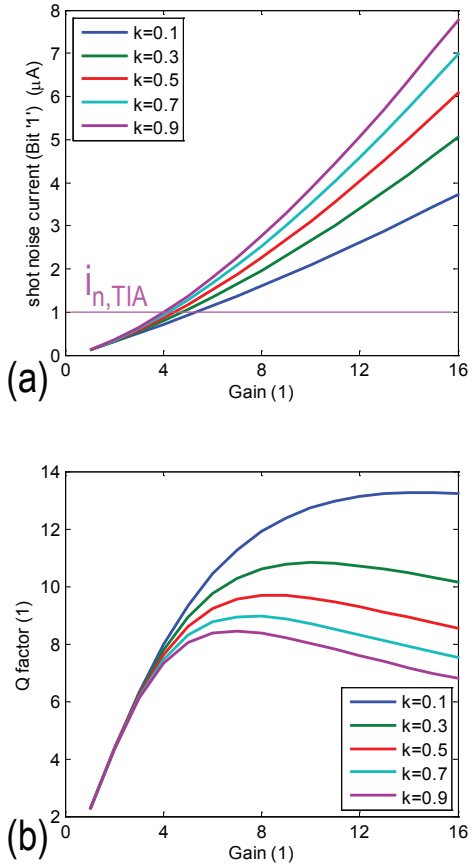

Figure 1.23: (a) The shot noise in the current at bit 1 level as a function of the avalanche gain for various k-values. (b) The Q factor as a function of the avalanche gain for various k values.

1.4.3.2 Non-local Field Avalanche Theory

A good description of the non-local field avalanche theory can be found in [53], which is summarized here. The impact ionization is a stochastic process, and it can best be described in terms of the probability distribution function *(pdf) p(x)*, which is the probability per unit length that a carrier ionizes a distance x from the injection point or the point where it was created by another impact ionization event. For the local field theory, as shown in Fig. 25(a), the *pdf* for electrons has the form $p(x) = \alpha^{-1} \cdot exp(-\alpha x)$. The noise power spectral density *pdf* for a mean gain $\langle \mathrm{M} \rangle$ and a mean photocurrent $\langle I_{ph} \rangle$ is given by the expression

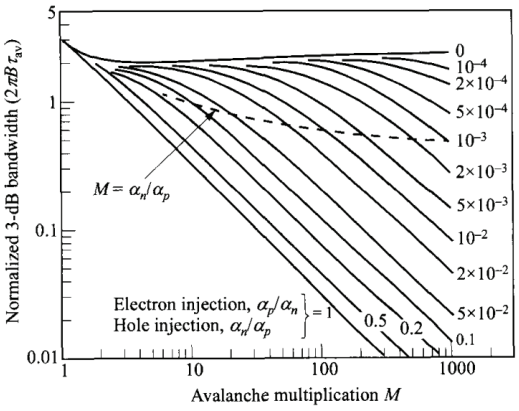

Figure 1.24: 3-dB O/E bandwidth drop with increasing avalanche gain for different k values [49].

$\varphi = 2q \cdot I_{ph} \cdot < M >^2 \cdot F(M)$. ***F(M)*** is the excess noise factor, which arises from the random nature of impact ionization. It is well known that the impact ionization is nonlocal, in that, carriers injected into the high-field region are cool and require a certain distance to attain a sufficient energy to ionize [54]. This also applies to carriers immediately after the ionization, because their final states are typically near the band edge. The distance in which essentially no impact ionization occurs is frequently referred to as the "dead space" for electrons (holes).

For the case with a thin multiplication region, the nonlocal nature of the impact ionization, as manifested in the "dead space", reduces the excess noise. With strong fields encountered in the thin multiplication regions, the *pdf* must be modified to account for the fact that $p(x) \sim 0$ for $x <$ the dead space. Fig. 25(b) illustrates qualitatively how incorporating the dead space alters the *pdfs*. We observe that the dead space length decreases with an increasing field. This is because at the strongest field the carrier transport becomes quasi-ballistic, and the dead space length is, to good approximation, equal to E_{th}/qF , where E_{th} is the threshold energy for impact ionization, q is the electron charge, and F is the electric field strength. We also note that the pdf also narrows significantly with the increasing field. Since the width of the pdf decreases faster than the reduction in the dead space, the net result is that the ionization process becomes more deterministic which reduces the variation in *M*.

Fig. 26 shows the calculated gain distributions for two $Al_{0.48}In_{0.52}As$ APDs with multiplication layer thickness of 1.0 μm (dashed line) and 0.1 μm (solid line) [55]. These APDs have the same average gain, $M \sim 20$, but the excess noise factors are 6.9 and 4.0 for the 1.0 and 0.1 μm APDs, respectively. The gain

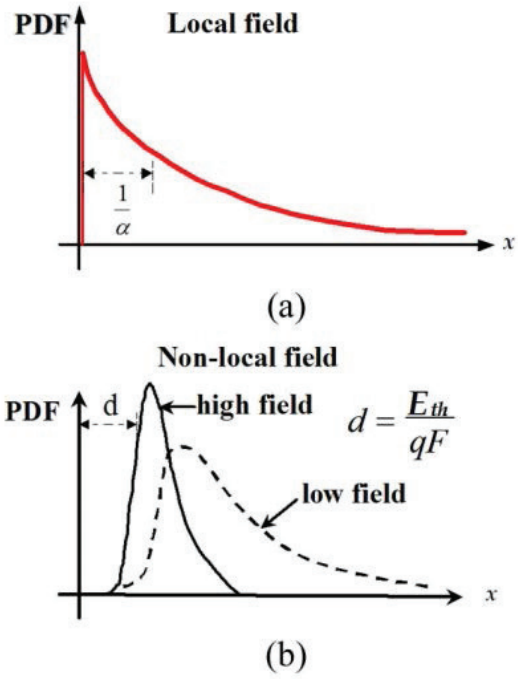

Figure 1.25: PDFs for (a) the local field model and (b) inclusion of the dead space for high field (solid line) and low field (dashed line) [53].

distribution of the 1.0-μm APD is broader than that of the 0.1-μm device. This illustrates the benefit of using a thin multiplication region to make the avalanche multiplication process more deterministic. and thus to reduce the avalanche excess noise.

1.4.3.3 State of the art

A great amount of research has been devoted to developing high sensitivity Si/Ge APDs as shown in Fig. 27. Intel researchers [44] demonstrated high sensitivity vertical-illumination Si/Ge APDs (-28 dBm receiver sensitivity for a bit error rate (BER) of 1×10^{-12} at 10 Gbps) by leveraging the superior avalanche performance of silicon and using germanium for light absorption. The device operates at a bias voltage of about 25 V, due to the 500 nm thick Si multiplication layer used. IBM researchers [50] demonstrated high avalanche performance in germanium (effective k-value of $\sim$0.2 and a gain·bandwidth product (GBP) of $\sim$300 GHz) at a low bias voltage of 3 V by generating strongly non-uniform electric fields in a 30 nm thin Ge multiplication region. The constructed optical receiver shows

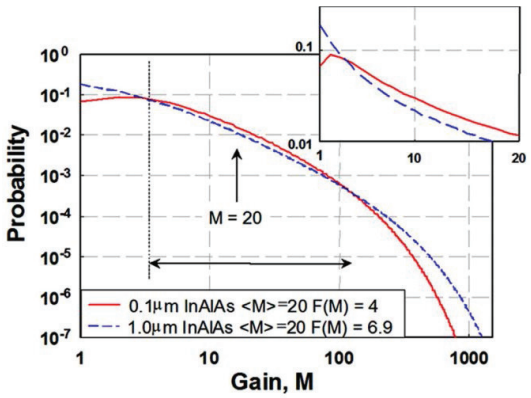

Figure 1.26: Comparison of the gain distribution curves for $Al_{0.48}In_{0.52}As$ APDs having multiplication region widths of 1.0 μm (dashed line) and 0.1 μm (solid line). The average gain for both APDs is $M \sim 20$, but the excess noise factors for the 1.0- and 0.1-μm APDs are 6.9 and 4, respectively [55].

-13.9 dBm absolute sensitivity for a 1×10^{-9} BER at 10 Gbps, limited by the intrinsic large dark current of the metal-semiconductor-metal design. Researchers from UParisSud [51] reported Ge lateral p-i-n junction waveguide APDs with a 500 nm wide Ge multiplication region, showing a GBP of 180 GHz at -7 V. HP lab researchers [52] reduced the break-down voltage of separated-absorption-charge-multiplication Si/Ge APDs to -10 V by adopting an 100 nm thin Si multiplication layer, which shows a GBP of 290 GHz.

1.5 Motivation of this PhD thesis

The motivation of this PhD thesis is to explore high performance Ge p-i-n and avalanche photodetectors, using which highly sensitive optical receivers can be constructed. These high sensitivity optical receivers greatly improve the power efficiency and therefore power consumption of Si photonics optical transceivers.

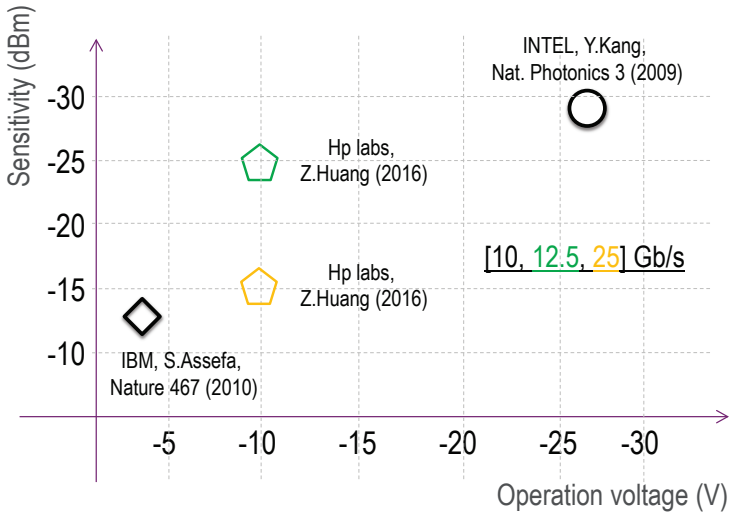

Figure 1.27: State-of-the-art Ge/Si APDs, absolute sensitivity versus operation voltage.

References

[1] *Cisco Global Cloud Index: Forecast and Methodology, 20142019 White Paper*. Technical report, Cisco, 2016.

[2] *http://www.abb.com/cawp/seitp202/d0d7d254a8d286d9c1257dfd004cd3b6.aspx*.

[3] Christoforos Kachris and Ioannis Tomkos. *A survey on optical interconnects for data centers*. IEEE Communications Surveys and Tutorials, 14(4):1021–1036, 2012.

[4] Ansheng Liu, Richard Jones, Ling Liao, Dean Samara-Rubio, Doron Rubin, Oded Cohen, Remus Nicolaescu, and Mario Paniccia. *A high-speed silicon optical modulator based on a metal-oxide-semiconductor capacitor.* Nature, 427(6975):615–8, 2004.

[5] Qianfan Xu, Bradley Schmidt, Sameer Pradhan, and Michal Lipson. *Micrometre-scale silicon electro-optic modulator.* Nature, 435(7040):325–7, 2005.

[6] G. T. Reed, G. Mashanovich, F. Y. Gardes, and D. J. Thomson. *Silicon optical modulators*. Nature Photonics, 4(8):518–526, 2010.

[7] Jianfeng Ding, Hongtao Chen, Lin Yang, Lei Zhang, Ruiqiang Ji, Yonghui Tian, Weiwei Zhu, Yangyang Lu, Ping Zhou, and Rui Min. *Low-voltage, high-extinction-ratio, Mach-Zehnder silicon optical modulator for CMOS-compatible integration*. Optics Express, 20(3):3209–3218, 2012.

[8] Jianfeng Ding, Hongtao Chen, Lin Yang, Lei Zhang, Ruiqiang Ji, Yonghui Tian, Weiwei Zhu, Yangyang Lu, Ping Zhou, Rui Min, and Mingbin Yu. *Ultra-low-power carrier-depletion Mach-Zehnder silicon optical modulator*. Optics Express, 20(7):7081, 2012.

[9] Laurent Vivien, Johann Osmond, Jean-Marc Fédéli, Delphine Marris-Morini, Paul Crozat, Jean-François Damlencourt, Eric Cassan, Y Lecunff, and Suzanne Laval. *42 GHz p.i.n Germanium photodetector integrated in a silicon-on-insulator waveguide.* Optics Express, 17(8):6252–7, 2009.

[10] Shirong Liao, Ning-Ning Feng, Dazeng Feng, Po Dong, Roshanak Shafiiha, Cheng-Chih Kung, Hong Liang, Wei Qian, Yong Liu, Joan Fong, John E Cunningham, Ying Luo, and Mehdi Asghari. *36 GHz submicron silicon waveguide germanium photodetector.* Optics Express, 19(11):10967–10972, 2011.

[11] Christopher T. DeRose, Douglas C. Trotter, William a. Zortman, Andrew L. Starbuck, Moz Fisher, Michael R. Watts, and Paul S. Davids. *Ultra compact 45 GHz CMOS compatible Germanium waveguide photodiode with low dark current*. Optics Express, 19(25):24897, 2011.

[12] Stefan Lischke, Dieter Knoll, Christian Mai, Lars Zimmermann, Anna Peczek, Marcel Kroh, Andreas Trusch, Edgar Krune, Karsten Voigt, and A. Mai. *High bandwidth, high responsivity waveguide-coupled germanium p-i-n photodiode*. Optics Express, 23(21):27213, 2015.

[13] H Chen, P Verheyen, P De Heyn, G Lepage, J De Coster, S Balakrishnan, P Absil, W Yao, L Shen, G Roelkens, and J Van Campenhout. *-1 V bias 67 GHz bandwidth Si-contacted germanium waveguide p-i-n photodetector for optical links at 56 Gbps and beyond*. Opt. Express, 24(5):4622–4631, mar 2016.

[14] T Komljenovic, S Srinivasan, E Norberg, M Davenport, G Fish, and J E Bowers. *Widely Tunable Narrow-Linewidth Monolithically Integrated External-Cavity Semiconductor Lasers*. IEEE Journal of Selected Topics in Quantum Electronics, 21(6):214–222, nov 2015.

[15] Y H Jhang, K Tanabe, S Iwamoto, and Y Arakawa. *InAs/GaAs Quantum Dot Lasers on Silicon-on-Insulator Substrates by Metal-Stripe Wafer Bonding*. IEEE Photonics Technology Letters, 27(8):875–878, apr 2015.

[16] Zhechao Wang, Bin Tian, Marianna Pantouvaki, Weiming Guo, Philippe Absil, Joris Van Campenhout, Clement Merckling, and Dries Van Thourhout. *Room Temperature InP DFB Laser Array Directly Grown on (001) Silicon*. Nature Photonics, 9(12):837–842, 2015.

[17] S. Keyvaninia, M. Muneeb, S. Stankovi?, P. J. Van Veldhoven, D. Van Thourhout, and G. Roelkens. *Ultra-thin DVS-BCB adhesive bonding of III-V wafers, dies and multiple dies to a patterned silicon-on-insulator substrate*. Optical Materials Express, 3(1):35–46, 2013.

[18] Gunther Roelkens, Amin Abassi, Paolo Cardile, Utsav Dave, Andreas de Groote, Yannick de Koninck, Sören Dhoore, Xin Fu, Alban Gassenq, Nannicha Hattasan, Qiangsheng Huang, Sulakshna Kumari, Shahram Keyvaninia, Bart Kuyken, Lianyan Li, Pauline Mechet, Muhammad Muneeb,

Dorian Sanchez, Haifeng Shao, Thijs Spuesens, Ananth Subramanian, Sarah Uvin, Martijn Tassaert, Kasper van Gasse, Jochem Verbist, Ruijun Wang, Zhechao Wang, Jing Zhang, Joris van Campenhout, Xin Yin, Johan Bauwelinck, Geert Morthier, Roel Baets, and Dries van Thourhout. *III-V-on-Silicon Photonic Devices for Optical Communication and Sensing*. Photonics, 2(3):969–1004, 2015.

[19] Peter Peter Verheyen, Marianna Pantouvaki, Joris Van Campenhout, Philippe P Absil, Hongtao Chen, Peter De Heyn, Guy Lepage, Jeroen De Coster, Pieter Dumon, Adil Masood, Dries Van Thourhout, Roel Baets, and Wim Bogaerts. *Highly Uniform 25 Gb/s Si Photonics Platform for High-Density, Low-Power WDM Optical Interconnects*. In Advanced Photonics for Communications, page IW3A.4. Optical Society of America, 2014.

[20] *http://www.europractice-ic.com/SiPhotonics_technology_imec_passives.php*.

[21] Gang Wang. *Ge and InP selective epitaxial growth on Si substrates for advanced CMOS devices*. PhD thesis, KATHOLIEKE UNIVERSITEIT LEUVEN, 2011.

[22] Philippe P Absil, Peter Verheyen, Peter De Heyn, Marianna Pantouvaki, Guy Lepage, Jeroen De Coster, and Joris Van Campenhout. *Silicon photonics integrated circuits: a manufacturing platform for high density, low power optical I/O's*. Opt. Express, 23(7):9369–9378, apr 2015.

[23] Philippe P Absil, Peter De Heyn, Hongtao Chen, Peter Verheyen, Guy Lepage, Marianna Pantouvaki, Jeroen De Coster, Amit Khanna, Youssef Drissi, Dries Van Thourhout, and Joris Van Campenhout. *Imec iSiPP25G silicon photonics: a robust CMOS-based photonics technology platform*, 2015.

[24] *http://www.europractice-ic.com/SiPhotonics_technology_imec_ISIPP25G.php*.

[25] Marianna Pantouvaki, Peter De Heyn, Rakowski Michal, Peter Verheyen, Snyder Brad, Ashwyn Srinivasan, Hongtao CHEN, Jeroen De Coster, Guy Lepage, Philippe Absil, and Joris Van Campenhout. *50Gb/s Silicon Photonics Platform for Short-Reach Optical Interconnects*. In Optical Fiber Communication Conference, page Th4H.4. Optical Society of America, 2016.

[26] M Rakowski, M Pantouvaki, P De Heyn, P Verheyen, M Ingels, H Chen, J De Coster, G Lepage, B Snyder, K De Meyer, M Steyaert, N Pavarelli, J S Lee, P O'Brien, P Absil, and J Van Campenhout. *A 4x20Gb/s WDM ring-based hybrid CMOS silicon photonics transceiver*. In 2015 IEEE International Solid-State Circuits Conference - (ISSCC) Digest of Technical Papers, pages 1–3, feb 2015.

[27] David A B Miller. *Device requirements for optical interconnects to silicon chips*. Proceedings of the IEEE, 97(7):1166–1185, 2009.

[28] Edward D. Palik, editor. *Handbook of Optical Constants of Solids*. Academic Press NY, 1985.

[29] *https://de.wikipedia.org/wiki/Pin-Diode*.

[30] *https://www.rp-photonics.com/responsivity.html*.

[31] Tao Yin, Rami Cohen, Mike M Morse, Gadi Sarid, Yoel Chetrit, Doron Rubin, and Mario J Paniccia. *31 GHz Ge n-i-p waveguide photodetectors on Silicon-on-Insulator substrate.* Optics express, 15(21):13965–13971, 2007.

[32] Dazeng Feng, Shirong Liao, Po Dong, Ning Ning Feng, Hong Liang, Dawei Zheng, Cheng Chih Kung, Joan Fong, Roshanak Shafiiha, Jack Cunningham, Ashok V. Krishnamoorthy, and Mehdi Asghari. *High-speed Ge photodetector monolithically integrated with large cross-section silicon-on-insulator waveguide*. Applied Physics Letters, 95(26), 2009.

[33] Laurent Vivien, Andreas Polzer, Delphine Marris-Morini, Johann Osmond, Jean Michel Hartmann, Paul Crozat, Eric Cassan, Christophe Kopp, Horst Zimmermann, and Jean Marc Fédéli. *Zero-bias 40Gbit/s germanium waveguide photodetector on silicon*. Optics Express, 20(2):1096, 2012.

[34] Guoliang Li, Ying Luo, Xuezhe Zheng, Gianlorenzo Masini, Attila Mekis, Subal Sahni, Hiren Thacker, Jin Yao, Ivan Shubin, Kannan Raj, John E Cunningham, and Ashok V Krishnamoorthy. *Improving CMOS-compatible Germanium photodetectors.* Optics express, 20(24):26345–50, 2012.

[35] Ari Novack, Mike Gould, Yisu Yang, Zhe Xuan, Matthew Streshinsky, Yang Liu, Giovanni Capellini, Andy Eu-Jin Lim, Guo-Qiang Lo, Tom Baehr-Jones, and Michael Hochberg. *Germanium photodetector with 60 GHz bandwidth using inductive gain peaking*. Optics Express, 21(23):28387–28393, 2013.

[36] Tsung-Yang Liow. *Waveguide Ge/Si Avalanche Photodetector with a Unique Low-Height-Profile Device Structure*. In Optical Fiber Communication Conference, page M2G.6. Optical Society of America, 2014.

[37] Yi Zhang, Shuyu Yang, Yisu Yang, Michael Gould, Noam Ophir, Andy Eu-Jin Lim, Guo-Qiang Lo, Peter Magill, Keren Bergman, Tom Baehr-Jones, and Michael Hochberg. *A high-responsivity photodetector absent metal-germanium direct contact*. Optics Express, 22(9):11367, 2014.

[38] Hong Tao Chen, Peter Verheyen, Peter De Heyn, Guy Lepage, Jeroen De Coster, Philippe Absil, Gunther Roelkens, and Joris Van Campenhout. *High-Responsivity Low-Voltage 28-Gb/s Ge p-i-n Photodetector With Silicon Contacts*. J. Lightwave Technol., 33(4):820–824, feb 2015.

[39] Ryan Going, Tae Joon Seok, Jodi Loo, Kyle Hsu, and Ming C. Wu. *Germanium wrap-around photodetectors on Silicon photonics*. Optics Express, 23(9):11975, 2015.

[40] Eduard Säckinger, editor. *Broadband Circuits for Optical Communications*. WILEY, 2005.

[41] B. Van Zeghbroeck. *Principles of Semiconductor Devices*. 2011.

[42] Jurgen Michel, Jifeng Liu, and Lionel C Kimerling. *High-performance Ge-on-Si photodetectors*. Nature Photonics, 4(8):527–534, 2010.

[43] *https://en.wikipedia.org/wiki/Avalanche_photodiode*.

[44] Yimin Kang, Han-Din Liu, Mike Morse, Mario J Paniccia, Moshe Zadka, Stas Litski, Gadi Sarid, Alexandre Pauchard, Ying-Hao Kuo, Hui-Wen Chen, Wissem Sfar Zaoui, John E Bowers, Andreas Beling, Dion C McIntosh, Xiaoguang Zheng, and Joe C Campbell. *Monolithic germanium/silicon avalanche photodiodes with 340 GHz gain-bandwidth product*. Nat Photon, 3(1):59–63, jan 2009.

[45] Yimin Kang, Zhihong Huang, Yuval Saado, Joe Campbell, Alex Pauchard, John Bowers, and Mario Paniccia. *High Performance Ge/Si Avalanche Photodiodes Development in Intel*. In Optical Fiber Communication Conference/National Fiber Optic Engineers Conference 2011, page OWZ1. Optical Society of America, 2011.

[46] M Huang, T Shi, P Cai, L Wang, S Li, W Chen, C y. Hong, and D Pan. *25Gb/s normal incident Ge/Si avalanche photodiode*. In 2014 The European Conference on Optical Communication (ECOC), pages 1–3, sep 2014.

[47] Mengyuan Huang, Pengfei Cai, Su Li, Liangbo Wang, Tzung-i Su, Liyuan Zhao, Wang Chen, Ching-yin Hong, and Dong Pan. *Breakthrough of 25Gb/s Germanium on Silicon Avalanche Photodiode*. In Optical Fiber Communication Conference, page Tu2D.2. Optical Society of America, 2016.

[48] Hektor Meier. *The Avalanche Photodiode Blog Part 1: Avalanche Multiplication*, 2013.

[49] Kwok K. Ng Simon M. Sze. *Physics of Semiconductor Devices*. 3rd editio edition, 2006.

[50] Solomon Assefa, Fengnian Xia, and Yurii a Vlasov. *Reinventing germanium avalanche photodetector for nanophotonic on-chip optical interconnects.* Nature, 464(7285):80–84, 2010.

[51] Léopold Virot, Paul Crozat, Jean-Marc Fédéli, Jean-Michel Hartmann, Delphine Marris-Morini, Eric Cassan, Frédéric Boeuf, and Laurent Vivien. *Germanium avalanche receiver for low power interconnects*. Nature Communications, 5:4957, 2014.

[52] Raymond G. Beausoleil Zhihong Huang, Di Liang, Charles Santori, Marco Fiorentino. *Low-voltage Si-Ge Avalanche photodiode*. Technical report, HP Laboratories, 2015.

[53] Joe C. Campbell. *Recent advances in telecommunications avalanche photodiodes*. In Journal of Lightwave Technology, volume 25, pages 109–121, 2007.

[54] Y. Okuto and C. R. Crowell. *Ionization coefficients in semiconductors: A nonlocalized property*. Physical Review B, 10(10):4284–4296, 1974.

[55] J.C. Campbell, Stephane Demiguel, Feng Ma Feng Ma, A. Beck, Xiangyi Guo Xiangyi Guo, Shuling Wang Shuling Wang, Xiaoguang Zheng Xiaoguang Zheng, Xiaowei Li Xiaowei Li, J.D. Beck, M.A. Kinch, Andrew Huntington, L.A. Coldren, Jean Decobert, and Nadine Tscherptner. *Recent advances in avalanche photodiodes*. IEEE Journal of Selected Topics in Quantum Electronics, 10(4):777–787, 2004.

2

Vertical p-i-n Germanium Waveguide Photodetectors

A germanium waveguide p-i-n photodetector is a critical building block in silicon photonics optical interconnects. They have been extensively researched, and various device structures have been developed [1–15]. A vertical p+(Ge)-i(Ge)-n+(Si) hetero-junction, as shown in Fig. 1, is widely adopted to construct such a photodetector [1–3, 5, 6, 12, 13], showing promising device performance.

A vertical p+(Ge)-i(Ge)-n+(Si) waveguide photodetector using a nominally 400 nm thick and 1 μm wide Ge layer existed at the start of this PhD thesis. It is referred to as a VPIN GePD hereafter. In this chapter, the simulation/modeling and characterization of a 15 μm long VPIN GePD will be discussed. The methodology in the simulation, modeling and characterization presented in this chapter is the foundation for developing advanced Ge waveguide p-i-n [16–18] and avalanche photodetectors [19, 20] in this PhD thesis.

2.1 Optical simulation

The VPIN GePD responsivity is determined by 3 processes, i.e. the light coupling from the 220 nm single-mode Si waveguide to the Ge waveguide, the light absorption process and the photo-carrier collection process. The light coupling and absorption process will be discussed in this section through optical simulation, and quantum efficiency was obtained assuming photo-carriers fully collec-

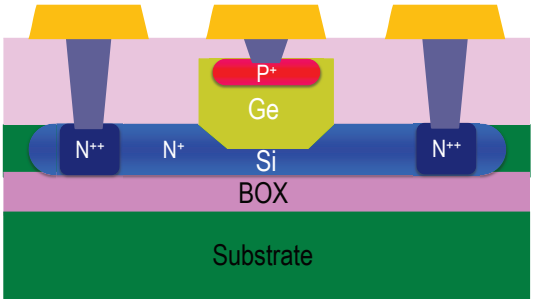

Figure 2.1: Cross sectional schematic of a vertical p+(Ge)-i(Ge)-n+(Si) Ge photodetector, VPIN GePD.

tion. The photo-carrier collection process will be discussed in section 2, Electrical simulation.

The optical simulation was implemented using *FiMMWave* from *Photon Design*. A 3-D schematic diagram of the VPIN GePD is shown in Fig. 2. Light is coupled from a 220 nm thick single-mode Si waveguide (450 nm wide) to the Ge waveguide using a Si waveguide taper. Fig. 3 shows the light transmission path from the single-mode Si waveguide to the Ge waveguide. The incoming light in the single-mode Si waveguide is guided by a linear Si taper maintaining the single mode condition to the interface between Si waveguide and Ge waveguide. Afterwards, the single-mode light passes the Si waveguide / Ge waveguide interface and it is absorbed in the Ge waveguide. The Ge layer is 400 nm thick and 1 μm wide, and the Si is 100 nm thick underneath the Ge layer. All the dimensions of the simulated structure were annotated in Fig. 3.

Fig. 4 shows the simulated structure built in Fimmwave. The launch condition in the simulation is the fundamental mode (TE polarization) of the Si waveguide at the Ge/Si interface assuming a sufficient long linear waveguide taper, which is not included in the simulation. 20 optical modes are assumed in the Ge waveguide and a Ge material absorption coefficient of 5000 cm^{-1} is adopted. The power coupling coefficients, S_{x1}, from the fundamental mode in the Si waveguide to the 20 optical modes in the Ge waveguide are shown Fig. 5(a). As the light is absorbed by the Ge as well as by the metal contact on Ge, the Ge absorption efficiency (the share of the light absorbed by Ge) was calculated by performing another simulation assuming a Ge material absorption coefficient of 0. The Ge absorption efficiency,ς, for the modes with a high power coupling coefficient (mode 1, mode 9, mode 10) are shown in Fig. 5(b), as a function of the metal contact recess depth. The quantum efficiency, η, was calculated from the Ge absorption in these 3 modes assuming fully photo-carriers absorption as shown in Fig. 5(c). It can be seen that a deeper recessed metal absorbs more light and thus the simulated quantum efficiency is

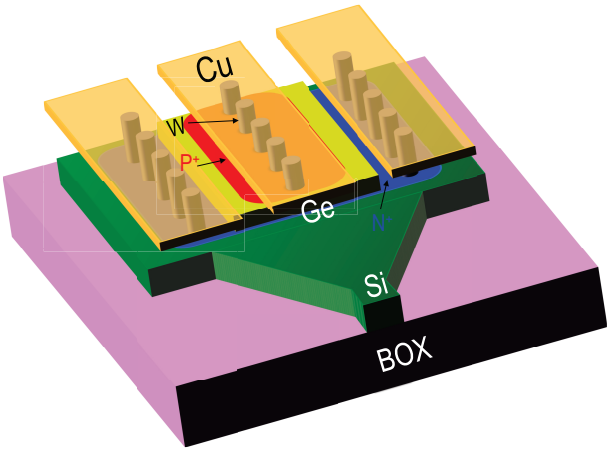

Figure 2.2: 3-D schematic diagram of a VPIN GePD.

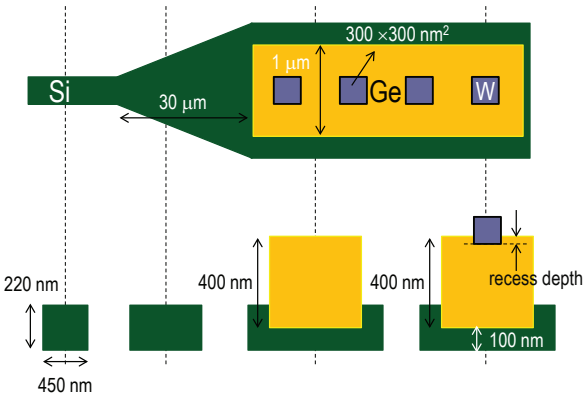

Figure 2.3: Schematic diagram illustrating the light transmission path from the single-mode Si waveguide to the Ge waveguide.

lower.

These optical modes are shown in Fig. 6 (a)-(c) for the case with a 20 nm metal contact recess depth in Ge, and the light transmission from the Si waveguide to the Ge waveguide is shown in Fig. 6(d).

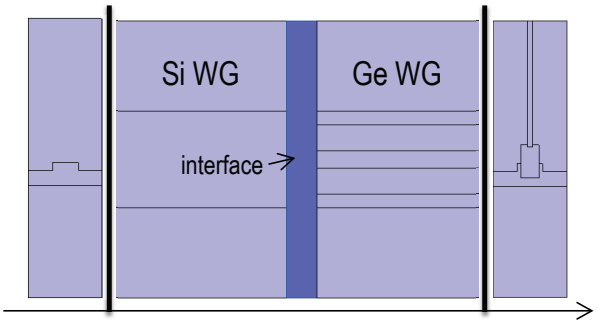

Figure 2.4: Structure built in Fimmwave to simulate light transmission from Si waveguide to Ge waveguide.

2.2 Electrical simulation

The photo-carrier collection process is the collection of the generated photo-carriers drifting along the electric field contributing to an external photocurrent. This largely depends on the electric field distribution in the active region of the VPIN GePD. In order to collect all the photo-carriers generated by the Ge layer, a relatively strong electric field in the active region is required. Photo-carrier pairs are separated by this electric field, and both electrons and holes drift across the depletion layer leading to a current flow in the external circuit. This electric field should be able to sweep out all the photo-generated carriers within their lifetime.

The doping profile in the Ge layer measured by secondary ion mass spectrometry (SIMS) in the VPIN GePD is shown in Fig. 7(a). It can be seen that the doping concentration drops quickly to $\sim 2 \times 10^{17}\ cm^{-3}$ in the center of the Ge layer 100 nm away from the Ge/Si interface. This residual doping is introduced by the ion implantation tail. The doping distribution simulated using *Sentaurus Process* (Monte Carlo ion implantation simulation calibrated by the SIMS data) in the VPIN GePD (2.2 μm wide Ge layer) is shown in Fig. 7(b). The doping profile along the A-A cut in Fig. 7(b) is also shown in Fig. 7(a) for comparison.

The simulated electric field distribution in the VPIN GePD (1 μm wide Ge layer) using *Sentaurus Device* is shown in Fig. 8(a), and the electric field profile along the A-A cut is shown Fig. 8(b). This heterogeneous Ge/Si VPIN diode configuration confines the electric field in the lower part of the Ge layer. At -1 V bias, the electric field is as strong as $\sim 8.5 \times 10^4$ V/cm in the bottom 100 nm of the Ge layer. The energy band diagram of the VPIN GePD along the A-A cut at 0 V and -1 V are shown in Fig. 8(c). It can be seen that, when a 1 V reverse bias is applied on the VPIN GePD, the depletion region mainly extends into the Ge layer. The depletion region width is 200 nm wide.

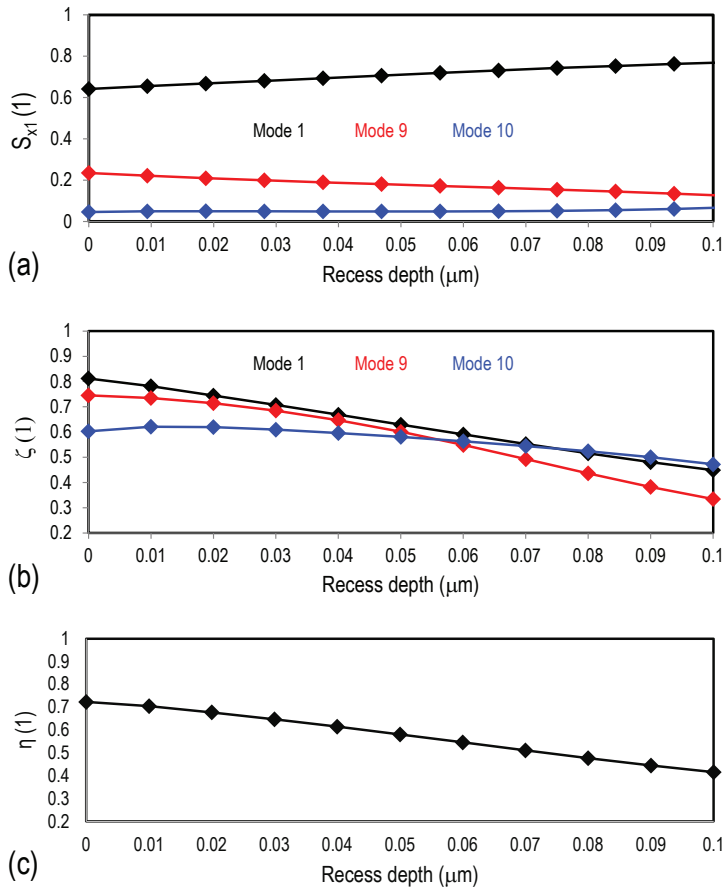

Figure 2.5: (a) Simulated power coupling coefficient from the fundamental mode in the Si waveguide to the various modes in Ge waveguide as a function of the metal contact recess depth in Ge. (b) The Ge absorption efficiency as a function of the metal contact recess depth in Ge for the modes in Ge waveguide with a high power coupling coefficient. (c) The calculated quantum efficiency from the Ge basorption in mode 1, mode 9 and mdoe 10.

2.3 Wafer-scale static measurements

The static performance of the VPIN GePD (responsivity and dark current) was characterized at 200 mm wafer scale. A fiber grating coupler is used as the interface for coupling light from a single-mode fiber to a 220 nm single-mode Si waveguide. A reference waveguide besides the VPIN GePD is used to de-embed the insertion loss of the fiber grating coupler. The optical insertion loss in the measurement system was carefully calibrated, and thus the received optical power

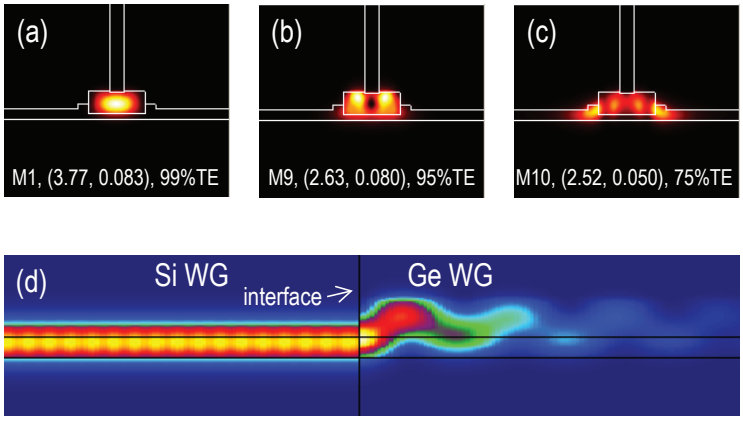

Figure 2.6: (a)-(c) The optical modes in the Ge waveguide with a high power coupling coefficient, (d) light transmission from Si waveguide to the Ge waveguide.

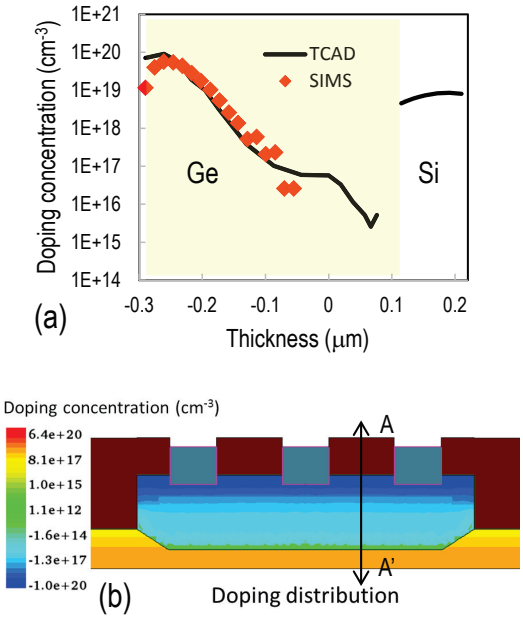

Figure 2.7: (a) Boron doping profile in the Ge layer in VPIN GePDs measured by SIMS, and doping profile from TCAD simulation along A-A cut. (b) Doping distribution in a baseline VPIN GePD with a 1 μm wide Ge layer generated from TCAD simulation (Monte-Carlo ion implantation simulation).

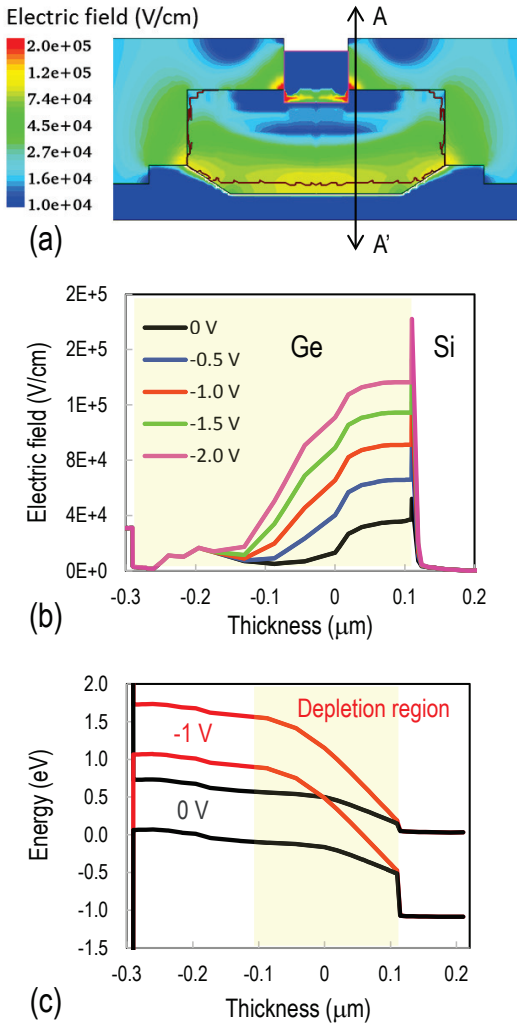

Figure 2.8: (a) Simulated electric field distribution in the baseline VPIN GePD at -1 V bias. (b) Electric field profile extracted along the A-A' cut at various bias voltages. (c) Simulated energy -band diagram along the A-A cut at 0 V and -1 V bias.

by the VPIN GePD in the static measurements can be determined. Both the dark current and light current were measured using a *Keithley* source meter, which also provides a bias voltage to the VPIN GePD using a DC probe. This way, the responsivity and dark current of a single VPIN GePD were measured. A 200 mm wafer was fixed on the chuck in the measurement system, and a motion controller

was used to move the chuck die by die such that the VPIN GePDs were measured at wafer scale.

Static measurement data A typical current-voltage characteristic of a 15 μm long VPIN GePD is shown in Fig. 9(a). As the bias voltage was increased from 0 to -3 V, the photocurrent measured at 1565 nm with a received optical power of -15.9 dBm was almost constant owing to the relatively strong built-in electric field that is capable of sweeping out the majority of photo-generated carriers within their lifetime. The dark current is 11 nA at -1 V, and the measured responsivity is 0.4 A/W. Wafer-scale dark current data of the VPIN GePD are shown in Fig. 9(b). The average dark current is 11 nA and 19 nA at -1 and -2 V bias, respectively.

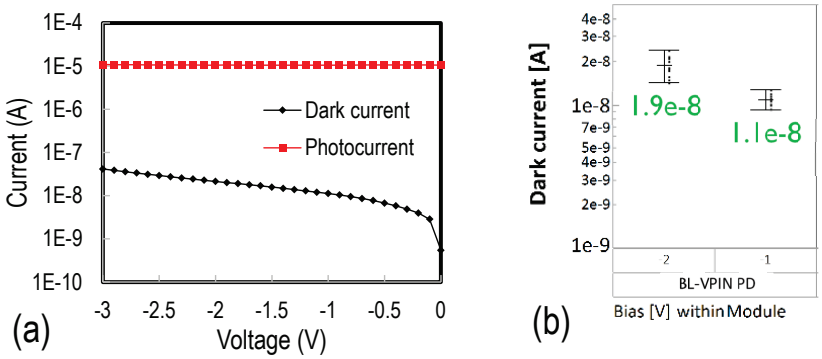

Figure 2.9: (a) A typical current-voltage characteristic of a 15 μm long VPIN GePD. (b) Wafer-scale dark current data of the VPIN GePD at -1 and -2 V bias. The mean of the wafer-scale data is annotated explicitly in the graph.

In Fig. 10(a), a contour plot of the wafer-scale responsivity data of the VPIN GePD at $\sim$1560 nm wavelength at -1 V bias is shown. The mean responsivity value is 0.4 A/W with a standard deviation of 0.05 A/W. The responsivity wavelength dependence from 1505 nm to 1580 nm of the VPIN GePD at -1.2 V bias is shown in Fig. 10(b). The responsivity is 0.6 A/W at 1505 nm, mainly limited by the light absorption from the metal contact plugs on Ge. It drops to 0.4 A/W at 1580 nm owing to both the reduced Ge material absorption coefficient and the increased light absorption from metal contact plugs. This increased metal light absorption is due to the increased modal overlap with metal contact plugs at long wavelength.

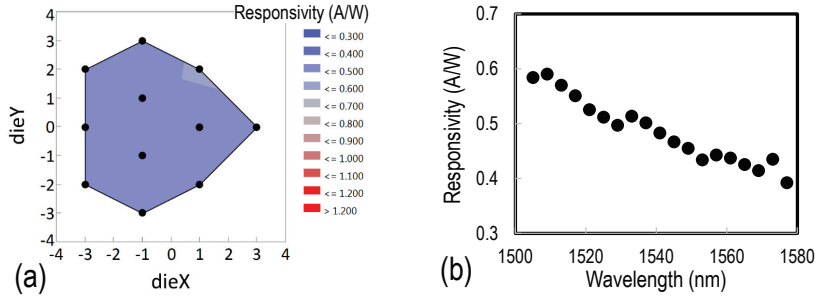

Figure 2.10: (a) Wafer-scale responsivity data at 1567 nm of the VPIN GePD at -1 V bias. (b) Responsivity as a function of wavelength of the VPIN GePD at -1 V bias.

2.4 Wafer-scale small-signal measurements

The small-signal performance of the VPIN GePD was characterized at 200 mm wafer scale. A 50 GHz vector network analyzer (VNA) and a 50 GHz lightwave component analyzer (LCA) were used to measure the small-signal transmission parameter (S_{21}) and reflection parameter (S_{22}). A *Keithley* source was used to provide a bias voltage to the VPIN GePD using a 50 GHz RF probe connected to a 50 GHz bias-tee, and the photocurrent was also monitored by this power source to determine the received optical power used in the small-signal measurements. The VNA, the LCA, the biasT, the RF probe, and the RF cables were carefully calibrated, and the RF signal attenuations and delays related to them were de-embedded. This way, the small-signal performance of a single VPIN GePD was measured. A 200 mm wafer was fixed on the chuck in the measurement system, and a motion controller was used to move the chuck die by die such that the VPIN GePDs were measured at wafer scale.

Small-signal measurement data Typical small-signal transmission parameters (S_{21}) of a 15 μm long VPIN GePD measured at 1550 nm are shown in Fig. 11(a). It shows a very high 3 dB O/E bandwidth of 42 GHz at 0 V and up to $\sim$50 GHz when the bias was increased to -1 V bias. The wafer-scale 3-dB O/E bandwidth data of the VPIN GePD is shown in Fig. 11(b). The average 3-dB O/E bandwidth value is 48 GHz and 49 GHz at -1 and -2 V bias, respectively.

2.5 Photodiode capacitance modeling

The capacitance of the vertical p+(Ge)-i(Ge)-n+(Si) junction was extracted by constructing an equivalent circuit model and numerically fitting the experimen-

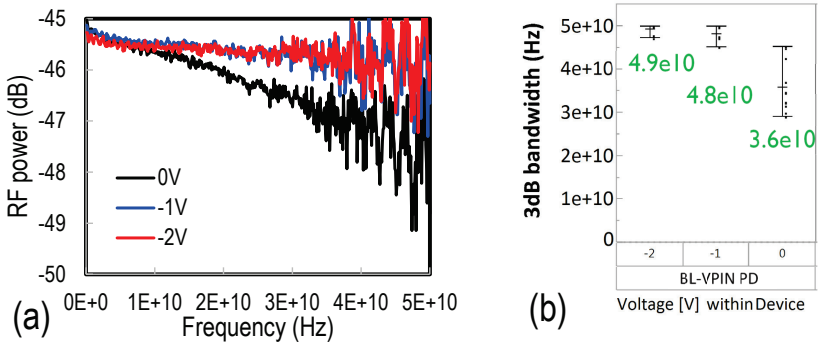

Figure 2.11: (a) Small-signal transmission parameter (S_{21}) of the VPIN GePD at 1550 nm. (b) Wafer-scale opto-electrical 3-dB bandwidth of the VPIN GePD at 0, 1 and 2 V bias. The mean of the wafer-scale data is annotated explicitly in the graph.

tal small-signal reflection parameter (S_{22}). The small-signal reflection parameter (S_{21}) can be expressed as a function of the equivalent impedance of the VPIN GePD (Z) as shown in Eq. 1, where the 50 (Ω) is the characteristic impedance of the RF probe used in the small-signal measurements. By fitting the experimental S_{22} parameter, the electrical components in the equivalent circuit model of the VPIN GePD were determined.

$$S_{22} = (Z - 50\Omega)/(Z + 50\Omega) \tag{2.1}$$

2.5.1 VPIN GePD equivalent circuit model

The constructed circuit model of the VPIN GePD is shown in Fig. 12(a). In the circuit model, C_j is the capacitance of the reverse biased p-i-n junction. R_{s1} (P-type contact on Ge) and R_{s2}/R_{s3} (N-type contact on Si) are the series resistance related to the p-i-n junction. C_{OX1}/C_{OX2} and R_{si} are related to the current path through the silicon substrate and the buried oxide (BOX). C_{m1}/C_{m2} represents the metal pad capacitance. This circuit model was simplified to an equivalent one as shown in Fig. 12(b).

It should be mentioned that this equivalent circuit model in Fig. 12(b)was not a direct deduction from Fig. 12(a). However, as the impact of the parasitic branch from the buried-in oxide and Si substrate is very small and can be safely neglected, consistent photodiode capacitance and series resistance data were obtained using this circuit.

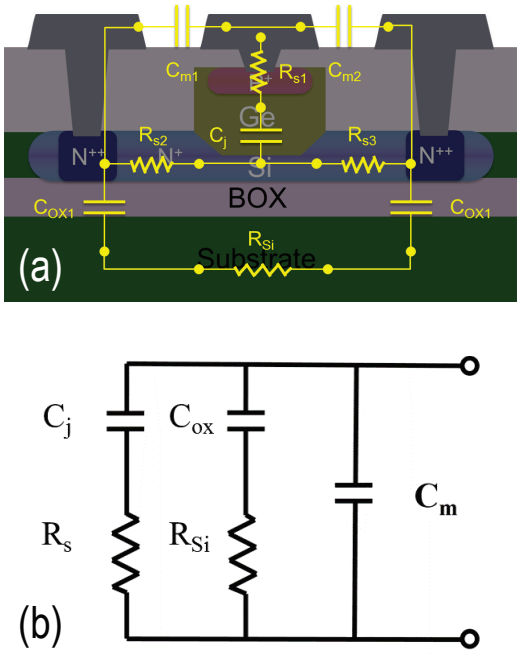

Figure 2.12: (a). VPIN GePD circuit model. (b) Simplified equivalent circuit model of the VPIN GePD.

2.5.2 VPIN junction capacitance extraction

With the equivalent circuit model in Fig. 12(b), the equivalent impedance of the VPIN GePD (Z) was expressed as a function of the electrical component in this circuit model. By numerically fitting both the real and imaginary part of the experimental S_{22} parameter as function of frequency, the components in the equivalent circuit model were determined, including the VPIN junction capacitance.

One example of the experimental and fitted real/imaginary part of the S_{22} parameter is shown in Fig. 13. The extracted VPIN junction capacitance (C_j) data and series resistance (R_s) data of the VPIN GePD are shown in Fig. 14(a) and Fig. 14(b). The mean junction capacitance value is 6.8 fF and 6.2 fF at -1 V and -2 V, respectively. The mean series resistance value is 45 Ω and 43 Ω at -1 V and -2 V, respectively. The metal pad capacitance is 7 fF. As consistent wafer-scale parasitic C_{OX}, R_{Si} data were not obtained, they were not shown.

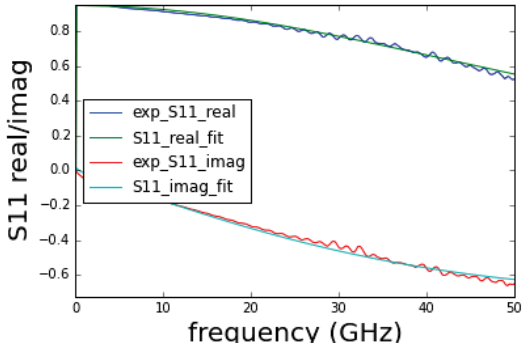

Figure 2.13: Experimental and fitted real/imaginary part of the small-signal reflection parameter (S_{22})

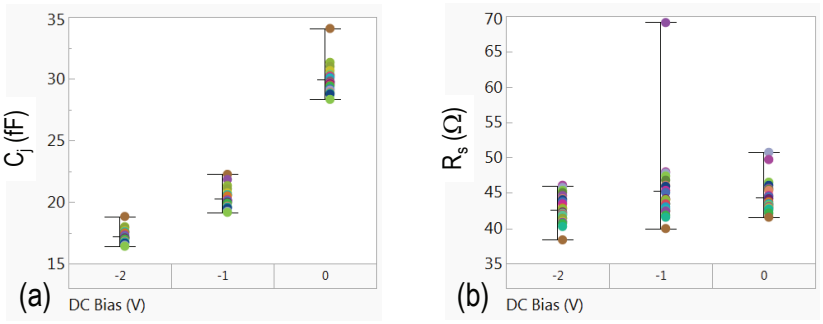

Figure 2.14: (a) Variability plot of the p-i-n junction capacitance data extracted from the fitting. (b) Variability plot of the series resistance data extracted from the fitting.

2.6 Opto-electrical bandwidth analysis

The 3-dB O/E bandwidth of the VPIN GePD (f_{3dB}) is limited by a combination of three factors: (1) RC-constant ($f_{3db,RC}$) (2) transit time ($f_{3dB,transit}$), and (3) diffusion of the generated photo-carriers ($f_{3dB,diffusion}$) as expressed in Eq. 2 [21].

$$f_{3dB} = \sqrt{\frac{1}{1/f_{RC}^2 + 1/f_{transit}^2 + 1/f_{diffu}^2}} \tag{2.2}$$

RC-constant The RC-constant normally sets the O/E bandwidth upper limit of a p-i-n photodetector. Solving the frequency response of the VPIN GePD equivalent circuit, as shown in Fig. 12 (b), assuming a 50 Ω load reveals that the RC-constant

limited 3-dB O/E bandwidth is ∼90 GHz and ∼100 GHz at -1 V and -2 V bias, respectively.

Transit time Photo carriers require a finite time to traverse the depletion layer before being collected. This transit-time limited 3-dB O/E bandwidth is shown in Eq. 3, in which τ_{PD} is the transit time and ν_S is the drifting velocity, W_D is the depletion region width. The details to derive Eq. 3 are described in [22].

$$f_{3dB,transit} = 1/(2\pi \times \tau_{PD}), \tau_{PD} = W_D/\nu_S \tag{2.3}$$

The depletion region width of the VPIN GePD is ∼200 nm at -1 V bias, as seen from Fig. 4(c). Using an electron/hole drift velocity of 6.5×10^6 cm/s [23, 24], the transit-time limited 3-dB O/E bandwidth is calculated to be 130 GHz at -1 V bias.

Diffusion of photo carriers Photo carriers generated outside the depletion region of the VPIN GePD (in the p+ doped region in the Ge layer) must diffuse to the depletion region before being collected by drifting along the electric field. This results in some time delay and limits the 3-dB O/E bandwidth.

2.7 Dark current analysis in VPIN GePDs

The dark current analysis in VPIN GePDs to be presented in this section was published in [18]. The dark current of the VPIN GePD originates from the material defects in the Ge layer. These defects include the misfit defects around the Ge/Si interface, the dislocation defects in the Ge layer linked to the misfit defects, and the surface defects on the Ge sidewall and top surface due to the improper passivation. They will become active current leakage channels under high electric field, governed by the Shockley-Read-Hall process.

In this section, a dark current analysis in the VPIN GePDs will be presented. In the analysis, surface leakage current and bulk leakage current were separated, and their activation energies were extracted. Surface leakage current originating from the minority carrier generation on the Ge layer sidewalls, governed by the Shockley-Read-Hall process and enhanced by the trap-assisted-tunneling process, was identified as the main contribution to the dark current of the VPIN GePDs at room temperature.

2.7.1 Dark current analysis

A schematic diagram illustrating and simplifying the dark current analysis of VPIN GePDs is shown in Fig. 15. The dark current (I_{dark}) is divided into 2 parts, i.e. the

surface leakage current and the bulk leakage current. The surface leakage current (I_{surf}) originates from the generation of minority carriers on the Ge layer surface due to the poor passivation quality of silicon dioxide. The non-passivated dangling bonds introduce a high interface-state density at Ge/SiO2 interfaces [25]. Since the top part of the Ge layer is implanted with boron, the interfacial defects at the Ge top surface/SiO2 interface are not electrically active, and only the interfacial defects on the Ge layer sidewall are considered for the surface leakage current in the analysis. The bulk leakage current (I_{bulk}) originates from the generation of minority carriers in the depletion region in the Ge layer along with the intrinsic bulk diffusion current. The surface leakage current is governed by the Shockley-Read-Hall (SRH) process ($J_{SRH,surf}$). It is proportional to the structure perimeter *P*, ($2\times(L+W)$), with *L* the length of the structure and *W* the width of the structure. The bulk leakage current has contributions from both the SRH process ($J_{SRH,bulk}$) and the diffusion process (J_{diff}). Both of them are proportional to the area of the device *S*, ($L \times W$) under the assumption that the Ge layer is wide enough to ignore corner effects.

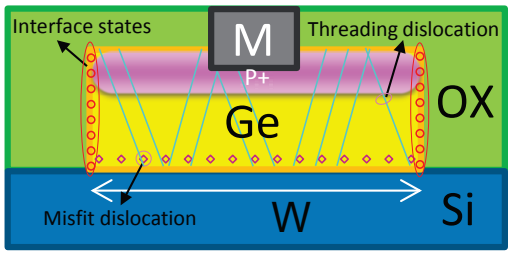

Figure 2.15: Schematic diagram illustrating the dark current modeling of VPIN GePDs.

The expression for the dark current (Eq. 4) can be reformulated as in Eq. 5. This reveals that the dark current to perimeter (I_{dark}/P) ratio scales linearly proportional to the area to perimeter ratio (*S/P*). The bulk leakage current density (J_{bulk}) can be determined by extracting the slope of this linear relationship. By dividing by the structure area (*S*), Eq. 4 can be reformulated as in Eq. 6. The dark current to area ratio (I_{dark}/S) scales linearly proportional to the perimeter to area ratio (*P/S*), the slope of which is the surface leakage current density (J_{surf}).

$$I_{dark} = I_{surf}+I_{bulk} = P\cdot J_{surf}+S\cdot J_{bulk} = P\cdot J_{SRH,surf}+S\cdot(J_{SRH,bulk}+J_{diff}) \tag{2.4}$$

$$I_{dark}/P = S/P \cdot J_{bulk} + J_{surf} \tag{2.5}$$

$$I_{dark}/S = P/S \cdot J_{surf} + J_{bulk} \tag{2.6}$$

2.7.2 Dark current measurement data and dark current modeling

Six VPIN GePD test structures, numbered from 1 to 6, in the design of experiment (DoE) have a Ge layer width of [0.6, 1.8, 4.2, 9.0, 16.2, 29.4] μm (exponentially scaling) and are 15 μm long, with a nominal Ge layer thickness of 400 nm. Temperature dependent current-voltage measurements were carried out on the VPIN GePD structures in the DoE at 200 mm wafer scale from 25°C to 125°C with a step of 25°C. Wafer-scale dark current data measured at 25°C for the 0.6 μm and 29.4 μm wide VPIN GePDs at various bias voltages are shown in Fig. 16 (a). The 0.6 μm wide Ge structure exhibits a mean dark current value of 8.8 nA and 53 nA at -1 V and -2 V, respectively. It increases to a mean value of 92 nA and 542 nA as the Ge layer width is scaled to 29.4 μm. It can be seen that there are some outlier dark current data points for the 29.4 μm wide Ge device, which is attributed to the inferior material quality in the large area Ge devices [26–28]. These outlier data points were removed from the dark current modeling. Fig. 16(b) shows the wafer-scale dark current data at -1 V for the 0.6 μm and 29.4 μm wide VPIN GePDs at various measurement temperatures. The mean dark current value of a 0.6 μm wide Ge structure is 8.8 nA and 179 nA measured at 25°C and 125°C. It rises to 92 nA and 2453 nA as the Ge layer is scaled to 29.4 μm width. Fig. 16(c) shows the wafer-scale dark current data at -1 V measured at 25°C and 125°C for the devices with varying Ge layer width. It should be mentioned that the different data point colors corresponding to VPIN GePDs at the different dies of the measured wafer. This convention applies to the following wafer-scale data in this paper.

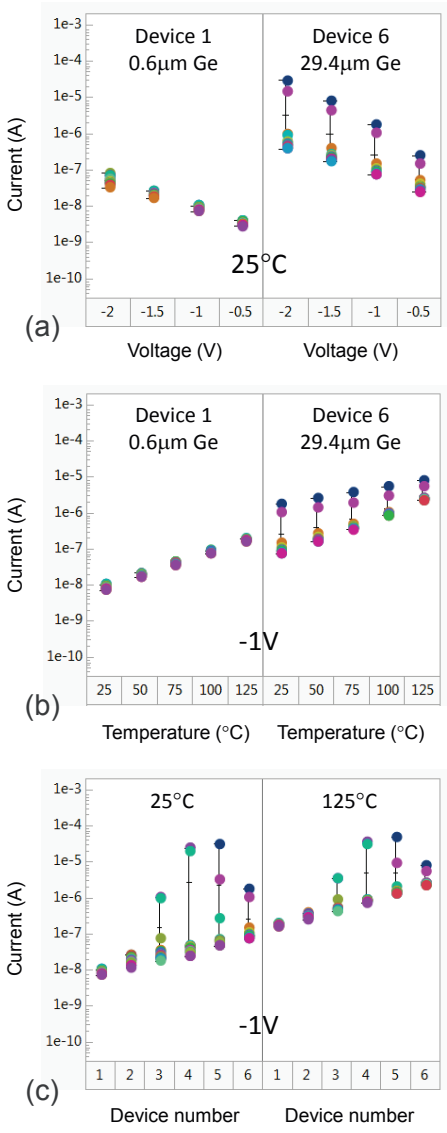

Figure 2.16: (a) Wafer-scale dark current data measured at 25°C at various bias voltages for the 0.6 µm and 29.4 µm wide VPIN GePDs. (b) Wafer-scale dark current data at -1 V at various measurement temperatures for the 0.6 µm and 29.4 µm wide VPIN GePDs. (c) Wafer-scale dark current data at -1 V for the devices with various Ge layer width measured at 25°C and 125°C.

The dark current to perimeter ratio (I_{dark}/P) as a function of area to perimeter

(*S/P*) ratio, measured at 25°C and 125°C is shown in Fig. 17(a) and Fig. 17(b), respectively. The area to perimeter ratio is [0.3, 0.8, 1.6, 2.8, 3.9, 5.0] μm for device 1 to 6, respectively. As mentioned in Section II, the linear relationship between them is valid under the assumption that the Ge layer is wide enough. In this paper, the linear fitting was done on the data of the devices with a Ge layer width of [4.2, 9.0, 16.2, 29.4] μm.

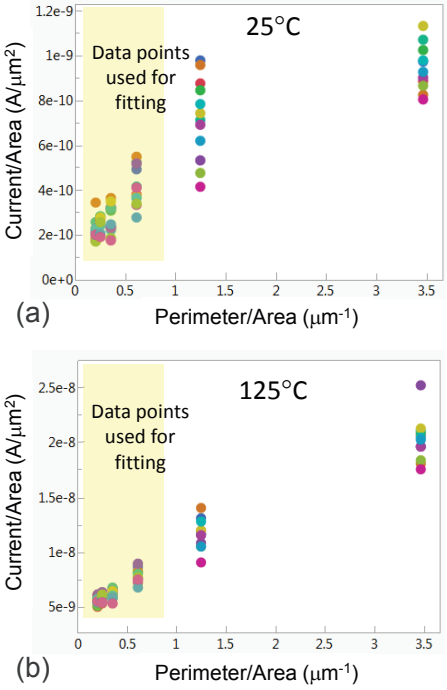

Figure 2.17: Wafer-scale data of dark current to perimeter ratio as a function of the area to perimeter ratio measured at (a) 25°C and (b) 125°C.

It can be seen that there is a larger spread in the data points measured at 25°C than those measured at 125°C. Considering the different temperature dependence of the SRH process related leakage current and diffusion current, as discussed below, the larger spread at 25°C indicates that there is a larger spread in the SRH process related leakage current at low temperature. This may result from the spread in the interface-state density on the Ge layer sidewall or the misfit/threading dislocations density inside the Ge layer at wafer scale.

The dark current to area ratio (I_{dark}/S) as a function of perimeter to area (*P/S*) ratio, measured at 25°C and 125°C is shown in Fig. 18(a) and Fig. 18(b), respectively. The perimeter to area ratio is [3.47, 1.24, 0.61, 0.35, 0.26, 0.20] μ

m^{-1} for device 1 to 6, respectively. Similar to extracting bulk leakage current density, the linear fitting was done on the data of the devices with a Ge layer width of [4.2, 9.0, 16.2, 29.4] μm.

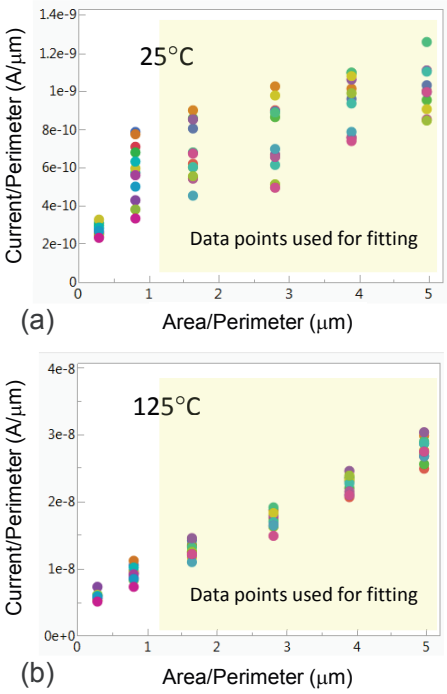

Figure 2.18: Wafer-scale data of dark current to area ratio as a function of the perimeter to area ratio measured at (a) 25°C and (b) 125°C.

Extracting the slope of the linear relationship in Eq. 2 and Eq. 3 using data of the VPIN GePD devices die by die generates surface leakage current density (J_{surf}) data and bulk leakage current density (J_{bulk}) data at wafer scale, as shown in Fig. 19(a) and Fig. 19(b). At 25°C, the mean value of surface leakage current density and bulk leakage current density is 0.5 nA/μm and 0.1 nA/μm^2, respectively. It rises to 5.5 nA/μm and 4.5 nA/μm^2 as the temperature is increased to 125°C.

2.7.3 Activation energy extraction

2.7.3.1 p-i-n diode leakage current theory

The diffusion current density can be expressed as in Eq. 7 for a reverse biased VPIN GePD. In the equation, q is the elementary charge, $n_{i,Ge}$ and $n_{i,Si}$ is the

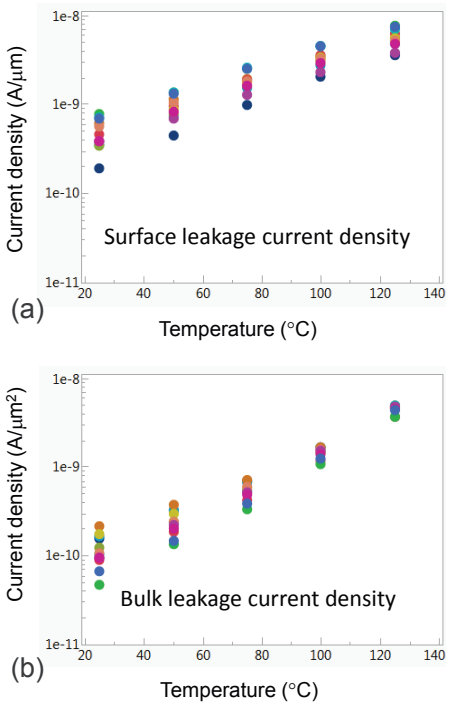

Figure 2.19: Wafer-scale (a) surface leakage current density data extracted from the slope of Eq. 3 and (b) bulk leakage current density data extracted from the slope of Eq. 2 using data of the devices die by die as a function of measurement temperature.

intrinsic carrier concentration in Ge and Si, N_D and N_A is the donor and acceptor doping concentration, D_n and D_p is the electron and hole diffusion coefficient, L_n and L_p is the electron and hole diffusion length, $E_{bg,Ge}$ is the Ge bandgap. As seen in Fig. 7(a), the n-type doping concentration in Si underneath the Ge layer is $5 \times 10^{18} cm^{-3}$ and quite uniform. As seen in Fig. 8(c), at -1 V bias, the depletion region extends 200 nm from the Ge/Si interface into the Ge layer, up to where the p-type doping concentration reaches $\sim 1 \times 10^{17} cm^{-3}$. Therefore, the diffusion current in the vertical p-i-n junction is dominated by the (minority) electron diffusion current in the quasi-neutral region in the Ge. The generation of minority carriers on the Ge layer sidewall can be expressed as in Eq. 8 for a reverse biased VPIN GePD. In the equation, q is the elementary charge, $n_{i,Ge}$ is the intrinsic carrier concentration in Ge, *S* is the surface recombination velocity on the Ge layer sidewall and *t* is the thickness of the depletion region. The generation of minority carriers in the depletion region (in Ge) can be expressed as in Eq. 9 for a reverse biased VPIN GePD. In the equation, q is the elementary charge, $n_{i,Ge}$ is

the intrinsic carrier concentration in Ge, τ_G is the minority carrier lifetime in the depletion region and *t* is the thickness of the depletion region.

$$j_{diff} = \frac{q \cdot D_p \cdot n_{i,Si}^2}{L_p N_D} + \frac{q \cdot D_n \cdot n_{i,Si}^2}{L_n N_A} \approx \frac{q \cdot D_p \cdot n_{i,Si}^2}{L_p N_D} \sim exp(\frac{-E_{bg,Ge}}{kT}) \quad (2.7)$$

$$j_{SRH,surf} = q \cdot S \cdot n_{i,Ge} \cdot t \sim exp(\frac{-E_{bg,Ge}}{2kT}) \quad (2.8)$$

$$j_{SRH,bulk} = q\frac{n_{i,Ge}}{\tau_G} \cdot t \sim exp(\frac{-E_{bg,Ge}}{2kT}) \quad (2.9)$$

The trap-assisted-tunneling (TAT) process, occurring along with the SRH process where there is a strong electric field, is considered as an enhancement to the SRH-related minority carrier generation for both the Ge layer sidewall leakage current ($J_{SRH,surf}$) and bulk leakage current ($J_{SRH,bulk}$). It can be described by the Hurkx model [29, 30], as given in Eq. 10 and Eq.11. In Eq.10, τ_{SRH} is the Shockley-Read-Hall carrier lifetime in the depletion region or the inverse of the surface recombination velocity on the Ge layer sidewall. $\tau_{SRH,TAT}$ is the equivalent carrier lifetime taking the enhancement from the TAT process into consideration. In Eq.11, *kT* is the thermal energy, q is the elementary charge, $\hbar$ is the reduced Planck constant, and m^* is the tunneling effective mass of the carriers. ΔE_T is related to the trap level and equals $E_{bg,Ge}/2$ for midgap states. *E* is the local electric field.

$$\tau_{SRH,TAT} = \tau_{SRH}/(1+\Gamma) \quad (2.10)$$

$$\Gamma = \frac{\Delta E_T}{kT}\int_0^1 exp[\frac{\Delta E_T}{kT}u - \frac{4}{3}\frac{\sqrt{2m^*}(\Delta E_T)^{3/2}}{q\hbar|E|}u^{3/2}]du \quad (2.11)$$

The natural logarithm of j_{diff}, $j_{SRH,surf}$ and $j_{SRH,bulk}$ scales linearly proportional to the natural logarithm of the intrinsic carrier concentration in Ge ($n_{i,Ge}$) and therefore scales linearly proportional to the reciprocal of temperature (*1/T*), without considering the enhancement of the TAT process. The activation energy can be extracted from the slope of this linear relationship. It is the Ge bandgap ($E_{bg,Ge}$) and half of the Ge bandgap ($E_{bg,Ge}/2$) for the diffusion current density and the SRH process related current density respectively. With the TAT process taken into consideration, the temperature dependence of the TAT enhancement factor Γ also contributes to the activation energy of the SRH-related leakage current density. Since TAT has a negative activation energy [20], it will lower the overall activation energy below half of Ge bandgap.

2.7.3.2 Activation energy data

Fig. 20(a) and Fig. 20(b) show the wafer-scale data in an Arrhenius plot for the surface leakage current density and bulk leakage current density, respectively. It can be seen that, while there is a linear relationship for the surface leakage current density, the data for the bulk leakage current density largely deviates from a linear relationship. This is because both the SRH process related leakage current and diffusion current contribute comparably to the bulk leakage current and they have different activation energy, while only the SRH related leakage current contributes to surface leakage current.

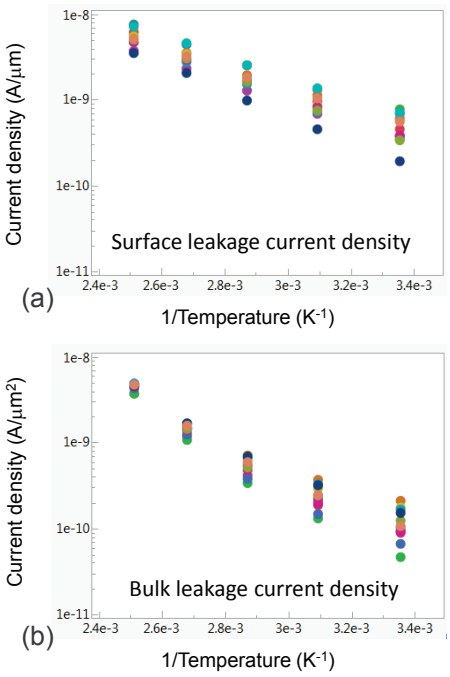

Figure 2.20: Arrhenius plot of wafer-scale (a) surface leakage current density data and (b) bulk leakage current density data at -1.0 V bias as a function of the inverse of the measurement temperature.

In order to differentiate the contribution of the SRH process related leakage current and diffusion current in the bulk leakage current over the measured temperature range, the activation energy is extracted as a function of temperature using data at 2 adjacent temperature points, as shown Fig. 21(b). The same exercise is done for surface leakage current for reference, as shown in Fig. 21(a). The surface leakage current shows an activation energy between 0.2∼0.3 eV. This value is be-

low half of the Ge bandgap ($E_{bg,Ge}/2$), which is attributed to the influence of trap-assisted-tunneling (TAT) occurring under relatively strong electric field [31–33]. The bulk leakage current activation energy increases from 0.2-0.3 eV to about 0.6 eV as the temperature is increased from 25°C to 125°C. This is because at low temperature, the SRH-related minority carrier generation in the depletion region in Ge dominates over the diffusion current density, exhibiting an activation energy value similar to that of the surface leakage current. As the measurement temperature is increased, there is a larger contribution from the diffusion current to the bulk dark current, resulting in a higher activation energy, close to the Ge bandgap ($E_{bg,Ge}$).

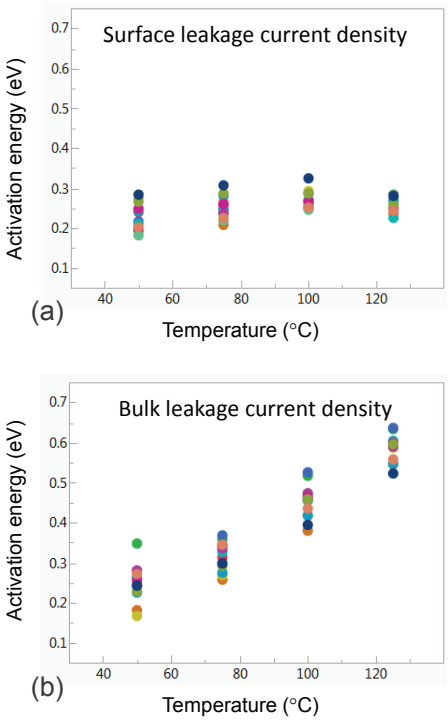

Figure 2.21: Wafer-scale activation energy data of (a) surface leakage current density and (b) bulk leakage current density as a function of measurement temperature.

2.7.4 Discussion

The dark current and its 2 contributing components, surface leakage current and bulk leakage current, of the 1.8 μm wide VPIN GePD in the DoE are shown in Fig. 22, as a function of the measurement temperature (at -1 V bias). These dimensions

are close to that in a baseline VPIN GePD device. At 25°C, surface leakage current contributes much more than bulk leakage current to the dark current of the VPIN GePD device. As the temperature is increased, the relative contribution of the bulk leakage current increases. This increase in the bulk leakage current mainly comes from the intrinsic diffusion current, as seen from the activation energy in Fig. 21(b). The fact that, for a baseline VPIN GePD device at room temperature, surface leakage current is contributing much more than bulk leakage current indicates that improving the Ge layer sidewall passivation quality to reduce the interface-state density on the Ge layer sidewall should be able to effectively reduce dark current of the VPIN GePD device. Since surface leakage current contributes much more than bulk leakage current to the dark current of the VPIN GePD device at low temperature, the large spread in the data points measured at 25°C in Fig. 17 (a) can be attributed to the large spread in the interface-state density on the Ge layer sidewall at wafer scale.

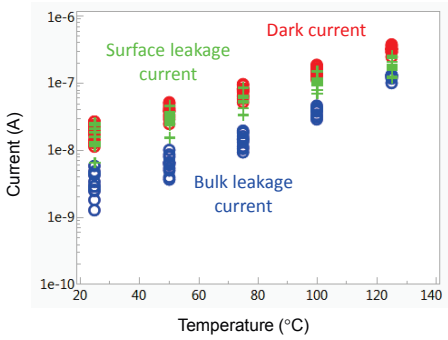

Figure 2.22: Wafer-scale dark current data and its 2 contributing components, surface leakage current and bulk leakage current, of a 1.8 μm wide VPIN GePD device at -1 V bias as a function of measurement temperature.

2.8 Conclusion

An in-depth analysis of the simulation, modeling and characterization of VPIN GePDs are presented. The methodology will be used to develop advanced Ge waveguide p-i-n and avalanche photodetectors, which will be presented in the following chapters.

References

[1] Jifeng Liu, Dong Pan, Samerkhae Jongthammanurak, Kazumi Wada, Lionel C Kimerling, and Jurgen Michel. *Design of monolithically integrated GeSi electro-absorption modulators and photodetectors on a SOI platform.* Optics express, 15(2):623–628, 2007.

[2] Tao Yin, Rami Cohen, Mike M Morse, Gadi Sarid, Yoel Chetrit, Doron Rubin, and Mario J Paniccia. *31 GHz Ge n-i-p waveguide photodetectors on Silicon-on-Insulator substrate.* Optics express, 15(21):13965–13971, 2007.

[3] Laurent Vivien, Johann Osmond, Jean-Marc Fédéli, Delphine Marris-Morini, Paul Crozat, Jean-François Damlencourt, Eric Cassan, Y Lecunff, and Suzanne Laval. *42 GHz p.i.n Germanium photodetector integrated in a silicon-on-insulator waveguide.* Optics Express, 17(8):6252–7, 2009.

[4] Dazeng Feng, Shirong Liao, Po Dong, Ning Ning Feng, Hong Liang, Dawei Zheng, Cheng Chih Kung, Joan Fong, Roshanak Shafiiha, Jack Cunningham, Ashok V. Krishnamoorthy, and Mehdi Asghari. *High-speed Ge photodetector monolithically integrated with large cross-section silicon-on-insulator waveguide*. Applied Physics Letters, 95(26), 2009.

[5] Shirong Liao, Ning-Ning Feng, Dazeng Feng, Po Dong, Roshanak Shafiiha, Cheng-Chih Kung, Hong Liang, Wei Qian, Yong Liu, Joan Fong, John E Cunningham, Ying Luo, and Mehdi Asghari. *36 GHz submicron silicon waveguide germanium photodetector.* Optics Express, 19(11):10967–10972, 2011.

[6] Christopher T. DeRose, Douglas C. Trotter, William a. Zortman, Andrew L. Starbuck, Moz Fisher, Michael R. Watts, and Paul S. Davids. *Ultra compact 45 GHz CMOS compatible Germanium waveguide photodiode with low dark current*. Optics Express, 19(25):24897, 2011.

[7] Laurent Vivien, Andreas Polzer, Delphine Marris-Morini, Johann Osmond, Jean Michel Hartmann, Paul Crozat, Eric Cassan, Christophe Kopp, Horst Zimmermann, and Jean Marc Fédéli. *Zero-bias 40Gbit/s germanium waveguide photodetector on silicon*. Optics Express, 20(2):1096, 2012.

[8] Guoliang Li, Ying Luo, Xuezhe Zheng, Gianlorenzo Masini, Attila Mekis, Subal Sahni, Hiren Thacker, Jin Yao, Ivan Shubin, Kannan Raj, John E Cunningham, and Ashok V Krishnamoorthy. *Improving CMOS-compatible Germanium photodetectors.* Optics express, 20(24):26345–50, 2012.

[9] Ari Novack, Mike Gould, Yisu Yang, Zhe Xuan, Matthew Streshinsky, Yang Liu, Giovanni Capellini, Andy Eu-Jin Lim, Guo-Qiang Lo, Tom Baehr-Jones, and Michael Hochberg. *Germanium photodetector with 60 GHz bandwidth using inductive gain peaking*. Optics Express, 21(23):28387–28393, 2013.

[10] Tsung-Yang Liow. *Waveguide Ge/Si Avalanche Photodetector with a Unique Low-Height-Profile Device Structure*. In Optical Fiber Communication Conference, page M2G.6. Optical Society of America, 2014.

[11] Yi Zhang, Shuyu Yang, Yisu Yang, Michael Gould, Noam Ophir, Andy Eu-Jin Lim, Guo-Qiang Lo, Peter Magill, Keren Bergman, Tom Baehr-Jones, and Michael Hochberg. *A high-responsivity photodetector absent metal-germanium direct contact*. Optics Express, 22(9):11367, 2014.

[12] Peter Peter Verheyen, Marianna Pantouvaki, Joris Van Campenhout, Philippe P Absil, Hongtao Chen, Peter De Heyn, Guy Lepage, Jeroen De Coster, Pieter Dumon, Adil Masood, Dries Van Thourhout, Roel Baets, and Wim Bogaerts. *Highly Uniform 25 Gb/s Si Photonics Platform for High-Density, Low-Power WDM Optical Interconnects*. In Advanced Photonics for Communications, page IW3A.4. Optical Society of America, 2014.

[13] Philippe P Absil, Peter Verheyen, Peter De Heyn, Marianna Pantouvaki, Guy Lepage, Jeroen De Coster, and Joris Van Campenhout. *Silicon photonics integrated circuits: a manufacturing platform for high density, low power optical I/O's*. Opt. Express, 23(7):9369–9378, apr 2015.

[14] Ryan Going, Tae Joon Seok, Jodi Loo, Kyle Hsu, and Ming C. Wu. *Germanium wrap-around photodetectors on Silicon photonics*. Optics Express, 23(9):11975, 2015.

[15] Stefan Lischke, Dieter Knoll, Christian Mai, Lars Zimmermann, Anna Peczek, Marcel Kroh, Andreas Trusch, Edgar Krune, Karsten Voigt, and A. Mai. *High bandwidth, high responsivity waveguide-coupled germanium p-i-n photodiode*. Optics Express, 23(21):27213, 2015.

[16] Hong Tao Chen, Peter Verheyen, Peter De Heyn, Guy Lepage, Jeroen De Coster, Philippe Absil, Gunther Roelkens, and Joris Van Campenhout. *High-Responsivity Low-Voltage 28-Gb/s Ge p-i-n Photodetector With Silicon Contacts*. J. Lightwave Technol., 33(4):820–824, feb 2015.

[17] H Chen, P Verheyen, P De Heyn, G Lepage, J De Coster, S Balakrishnan, P Absil, W Yao, L Shen, G Roelkens, and J Van Campenhout. *-1 V bias 67 GHz bandwidth Si-contacted germanium waveguide p-i-n photodetector for optical links at 56 Gbps and beyond*. Opt. Express, 24(5):4622–4631, mar 2016.

[18] H Chen, P Verheyen, P De Heyn, G Lepage, J De Coster, S Balakrishnan, P Absil, G Roelkens, and J Van Campenhout. *Dark current analysis in high-speed germanium p-i-n waveguide photodetectors*. Journal of Applied Physics, 119(21), 2016.

[19] H T Chen, J Verbist, P Verheyen, P De Heyn, G Lepage, J De Coster, P Absil, X Yin, J Bauwelinck, J Van Campenhout, and G Roelkens. *High sensitivity 10Gb/s Si photonic receiver based on a low-voltage waveguide-coupled Ge avalanche photodetector*. Opt. Express, 23(2):815–822, jan 2015.

[20] H. T. Chen, J. Verbist, P. Verheyen, P. De Heyn, G. Lepage, J. De Coster, P. Absil, B. Moeneclaey, X. Yin, J. Bauwelinck, J. Van Campenhout, and G. Roelkens. *25-Gb/s 1310-nm optical receiver based on a sub-5-V waveguide-coupled germanium avalanche photodiode*. IEEE Photonics Journal, 7(4), 2015.

[21] Y Ishikawa and K Wada. *Near-Infrared Ge Photodiodes for Si Photonics: Operation Frequency and an Approach for the Future*. IEEE Photonics Journal, 2(3):306–320, jun 2010.

[22] Kwok K. Ng Simon M. Sze. *Physics of Semiconductor Devices*. 3rd editio edition, 2006.

[23] C Jacoboni, F Nava, C Canali, and G Ottaviani. *Electron drift velocity and diffusivity in germanium*. Phys. Rev. B, 24(2):1014–1026, jul 1981.

[24] *http://www.ioffe.ru/SVA/NSM/Semicond/Ge/electric.html#Transport*.

[25] J. R. Weber, A. Janotti, P. Rinke, and C. G. Van De Walle. *Dangling-bond defects and hydrogen passivation in germanium*. Applied Physics Letters, 91(14), 2007.

[26] Hsin-Chiao Luan, Desmond R Lim, Kevin K Lee, Kevin M Chen, Jessica G Sandland, Kazumi Wada, and Lionel C Kimerling. *High-quality Ge epilayers on Si with low threading-dislocation densities*. Applied Physics Letters, 75(19), 1999.

[27] Jifeng Liu, Jurgen Michel, Wojciech Giziewicz, Dong Pan, Kazumi Wada, Douglas D Cannon, Samerkhae Jongthammanurak, David T Danielson, Lionel C Kimerling, Jian Chen, F Ömer Ilday, Franz X Kärtner, and John Yasaitis. *High-performance, tensile-strained Ge p-i-n photodetectors on a Si platform*. Applied Physics Letters, 87(10), 2005.

[28] T H Loh, H S Nguyen, R Murthy, M B Yu, W Y Loh, G Q Lo, N Balasubramanian, D L Kwong, J Wang, and S J Lee. *Selective epitaxial germanium on silicon-on-insulator high speed photodetectors using low-temperature ultrathin Si0.8Ge0.2 buffer*. Applied Physics Letters, 91(7), 2007.

[29] G A M Hurkx, H C de Graaff, W J Kloosterman, and M P G Knuvers. *A new analytical diode model including tunneling and avalanche breakdown*. IEEE Transactions on Electron Devices, 39(9):2090–2098, sep 1992.

[30] G A M Hurkx, D B M Klaassen, and M P G Knuvers. *A new recombination model for device simulation including tunneling*. IEEE Transactions on Electron Devices, 39(2):331–338, feb 1992.

[31] E Simoen, F De Stefano, G Eneman, B De Jaeger, C Claeys, and F Crupi. *On the Temperature and Field Dependence of Trap-Assisted Tunneling Current in Ge \hbox {p}ˆ{+}\hbox {n} Junctions*. IEEE Electron Device Letters, 30(5):562–564, may 2009.

[32] Mireia Bargallo Gonzalez, Geert Eneman, Gang Wang, Brice De Jaeger, Eddy Simoen, and Cor Claeys. *Analysis of the Temperature Dependence of Trap-Assisted-Tunneling in Ge pFET Junctions*. ECS Transactions, 34(1):725–730, 2011.

[33] Geert Eneman, Mireia Bargallo Gonzalez, Geert Hellings, Brice De Jaeger, Gang Wang, Jerome Mitard, Kristin DeMeyer, Cor Claeys, Marc Meuris, Marc Heyns, Thomas Hoffmann, and Eddy Simoen. *Trap-Assisted Tunneling in Deep-Submicron Ge pFET Junctions*. Meeting Abstracts, MA2010-01(23):1205, 2010.

3

Advanced Si-contacted Ge Waveguide p-i-n Photodetectors

In this chapter, we report Ge waveguide p-i-n photodetectors without direct metal contacts on Ge nor doping (ion implantation) in Ge, grown on and contacted through a silicon p-i-n diode structure. The Si-contacted Ge p-i-n photodetectors (Si-LPIN GePDs) go through a simpler fabrication process flow since the contact module on Ge is removed. This eliminates the responsivity loss owing to the light absorption from metal plugs on Ge, and therefore a much higher responsivity can be expected.

Two versions of Si-LPIN GePD will be reported in this chapter, which have been published in [1, 2]. They have the same design but different Ge layer thickness, 400 nm and 160 nm. The 400 nm thick Ge Si-LPIN GePD is reported in section 3.2, showing high responsivities larger than 1.0 A/W across the C-band and a high opto-electrical 3-dB bandwidth of 20 GHz at 1550 nm (-1 V bias). The 160 nm thick Ge Si-LPIN GePD is reported in section 3.3, exhibiting a high opto-electrical 3-dB bandwidth over 67 GHz at 1550 nm and a responsivity over 0.7 A/W across the O-band (-1 V bias). The dark current is smaller than 5 nA for both Si-LPIN GePDs at -1 V bias.

3.1 Ge p-i-n photodetector design exploration

The VPIN Ge PD reported in chapter 2 constructed on a heterogeneous p+(Ge)-i(Ge)-n+(Si) junction is the most straightforward photodetector design. Such a heterogeneous vertical Ge/Si junction is widely adopted to construct a Ge p-i-n photodetector [3–9]. Another widely studied Ge p-i-n photodetector design is based on a lateral p+(Ge)-i(Ge)-n+(Ge) LPIN junction with both anode and cathode metal contact on Ge [10, 11], as shown in Fig. 1.

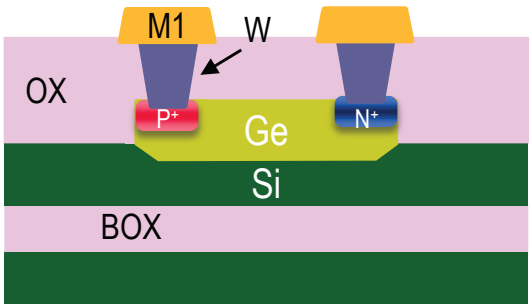

Figure 3.1: A lateral p-i-n Ge photodetector.

The drawbacks of both the VPIN and LPIN junction design is that the metal contact plugs on top of Ge absorb light, which introduces a large responsivity loss. Although intensive research has been done to minimize the responsivity loss by optimizing the contact plug layout on Ge, it is difficult to obtain high responsivity and high O/E bandwidth at the same time. In addition, the process to form a metal contact to germanium is less well developed in standard CMOS foundries, which increases the Si photonics process flow complexity. Hence a photodetector that does not require doping or metallization of germanium is highly desirable.

Fig. 2 shows such a Ge waveguide p-i-n photodetector without direct metal contacts on Ge nor doping (ion implantation) in Ge, grown on and contacted through a silicon p-i-n diode structure. The following of this chapter will focus on such Si-LPIN GePDs.

3.2 400 nm-Ge Si-LPIN GePD

Si-LPIN GePDs were firstly fabricated on the imec Si Photonics Platform using the standard process with a Ge nominal thickness of 400 nm.

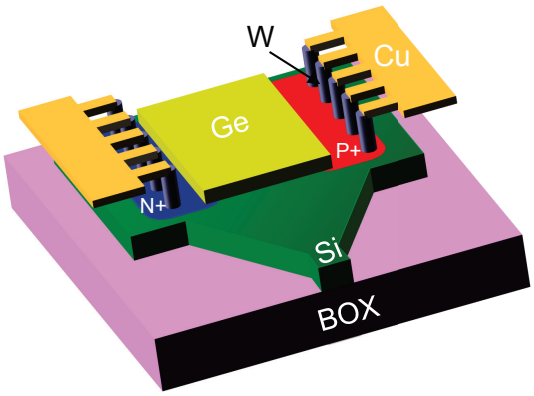

Figure 3.2: 3-D Cartoon of a Si-contacted Ge waveguide p-i-n photodetector.

3.2.1 Device Design and Fabrication

The Si-LPIN GePDs are implemented in imec's fully integrated Si Photonics Platform along with Si modulators [12] and various passive devices. They go through a process flow described in [8]. The cross section of the Si-LPIN photodetectors is schematically shown in Fig. 3(a). In Fig. 3(b), our baseline (BL) germanium photodetector based on a vertical p-i-n junction (VPIN) with P-type via-contact on top of germanium and N-type via contact on the silicon underneath is shown for reference. They are referred to as BL-VPIN photodetectors hereafter. The Si-LPIN GePD Ge layer width was reduced to 0.5 μm. This is because the Si-LPIN GePD O/E bandwidth is limited by transit time. Reducing the Ge width leads to a shorter transit distance and thus a shorter transit time assuming photo-carriers drift in their saturation velocity. This increases the O/E bandwidth. It can be seen that, compared to the BL-VPIN photodetectors configuration, there is no ion implantation in or metal via-plugs on germanium. The Si-LPIN photodiode shares exactly the same doping levels and contact process module of a silicon modulator. This significantly simplifies the silicon photonics process flow and will ultimately reduce the cost of building silicon-based photonic integrated circuits (PICs).

The electric field distribution in Si-LPIN photodetectors and BL-VPIN photodetectors at -1V obtained by numerically solving Poissons equation are shown in Fig. 4. In most of the germanium region, the electric field is stronger than 10^4 V/cm at -1V reverse bias for Si-LPIN photodetectors. It is strong enough for photo-generated carriers to drift at saturation velocity. The electric field is uniform in Si-LPIN photodetectors, while in BL-VPIN photodetectors, the strong electric field is confined to the bottom part of the germanium, where much higher defect density is expected due to the 4% lattice mismatch between germanium and sili-

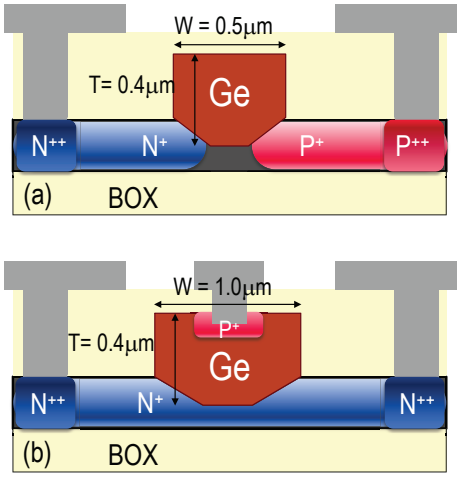

Figure 3.3: Cross sectional schematic with germanium dimensions of (a) Si-LPIN photodetectors and (b) BL-VPIN photodetectors.

con. These defects will become active current leakage channels under high electric field. Thus, lower dark current can be expected for Si-LPIN photodetectors. In addition, considering there is no via-contact metal absorption and free carrier absorption in the heavy doping contact region, much higher responsivity can be expected for Si-LPIN photodetectors.

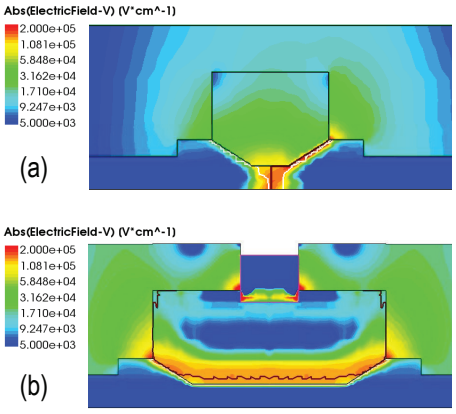

Figure 3.4: Electric field distribution in (a) a Si-LPIN photodetector and (b) a BL-VPIN photodetector at -1 V bias voltage.

3.2.2 Device Characteristics

3.2.2.1 Static measurements

A typical static current-voltage characteristic of a 13.8 μm-long and 0.5 μm-wide Si-LPIN photodetector is shown in Fig. 5(a). The device has a remarkably low dark current of 3 nA at -1V. It is still lower than 10 nA as the bias is increased to -3 V. This is among the lowest dark current values that have been reported for Ge WPDs [7]. The dark current analysis in the Si-LPIN GePD is more complex, which cannot be analyzed as that carried out in Section 2.7 for the VPIN GePD. This has not been fully understood yet. The photocurrent was measured at 1567 nm wavelength with a received optical power of -15.9 dBm. As the bias voltage was increased from 0V to -3V, the photocurrent was almost constant owing to the relatively strong built-in electric field that is capable of sweeping out the majority of photo-generated carriers within their lifetime. The measured responsivity is 1.0 A/W.

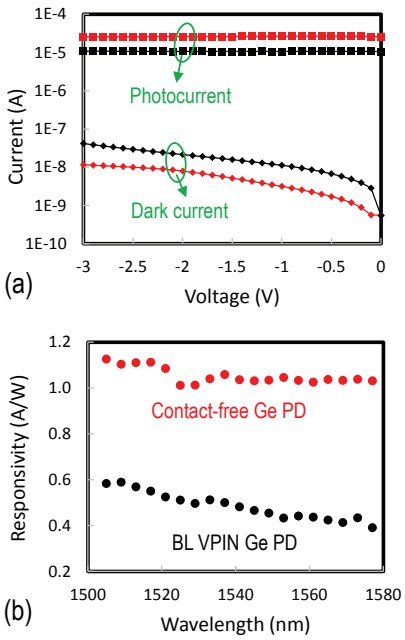

Figure 3.5: (a) Current-voltage characteristics of a 13.8 μm-long and 0.5 μm-wide Si-LPIN photodetector (red curves) and a 13.8 μm-long and 1.0 μm-wide BL-VPIN photodetector (black curves). (b) Responsivity versus wavelength for the Si-LPIN photodetector and the BL-VPIN Ge photodetector.

The dark current and photocurrent of a 13.8 μm-long and 1.0 μm-wide BL-

VPIN photodetector are also shown in Fig. 5(a) for reference. The photocurrent was measured at the same wavelength and under the same input optical power as that for the Si-LPIN photodetector. It can be seen that the Si-LPIN photodetector is capable of obtaining a photocurrent up to ∼2.5 times higher than that of a BL-VPIN device. At the same time, the dark current is 3 times lower than that of the latter.

The responsivity in the wavelength range between 1505 nm and 1580 nm of both devices was further measured and is shown in Fig. 5(b). The Si-LPIN photodetector has a responsivity higher than 1.0 A/W in the whole wavelength range, which is much higher than that measured from the BL-VPIN device (0.4∼0.6 A/W). This is among the best results that have been published for Ge WPDs [5, 6, 13–15].

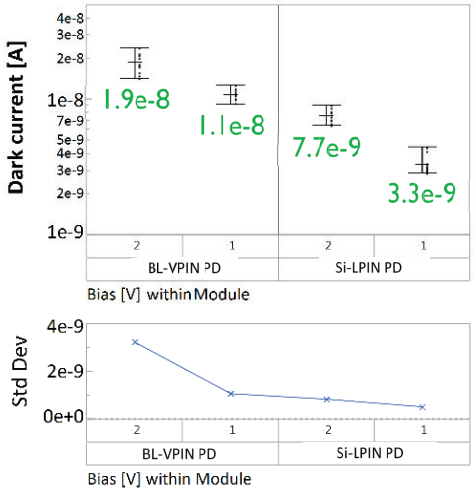

Figure 3.6: Wafer-scale dark current data of the Si-LPIN photodetector and the BL-VPIN photodetector at -1 V and -2 V. The mean of the wafer-scale data is annotated explicitly in the graph; Standard deviations (std Dev) of the wafer-scale data is given separately.

Wafer-scale dark current data of both the Si-LPIN photodetector and the BL-VPIN photodetector at -1 V and -2 V are shown in Fig. 6. The average dark current is 3.3 nA and 7.7 nA respectively, with a standard deviation of 0.5 nA and 0.8 nA, at -1 V and -2 V. In Fig. 7(a) and Fig. 7(b), contour plots of the wafer-scale responsivity data of both the Si-LPIN photodetector and the BL-VPIN photodetector at 1560 nm wavelength are shown. As for reponsivities larger than 0.95 A/W, it shows a yield of 91% for Si-LPIN photodetectors.

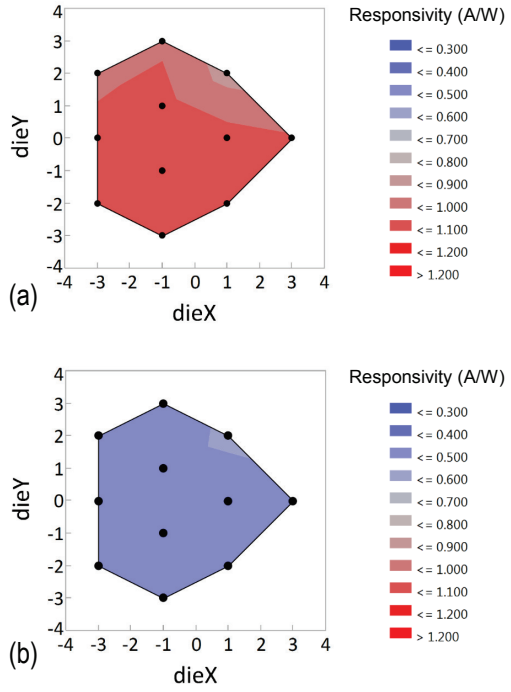

Figure 3.7: Wafer-scale responsivity data at 1567nm for (a) the Si-LPIN photodetector and (b) the BL-VPIN photodetector.

3.2.2.2 Small-signal measurements

Small-signal radio-frequency (RF) measurements were further carried out to characterize the high-speed performance of the devices. S_{21} traces at different bias voltages of the Si-LPIN photodetector are shown in Fig. 8(a). At -1 V, the device has a 3-dB bandwidth of 20 GHz, sufficient for receiving 28 Gbps OOK signals. The low bandwidth of 2.8 GHz at 0 V is due to the long transit time under the relatively low electric field strength in the device at 0 V. The bandwidth is further enhanced to 27 GHz as the bias voltage increases to -2 V.

S_{21} traces of the BL-VPIN photodetector are also shown in Fig. 8(b) for reference. The device has a very high 3 dB bandwidth of 42 GHz at 0 V and up to $\sim$50 GHz when the bias increases to -1 V. It should be noted that 50 GHz is the upper limit of our equipment measurement range. The wafer-scale 3dB bandwidth of both devices at 0 V, -1 V and -2 V is shown in Fig. 9. The average 3 dB bandwidth is 20 GHz and 27 GHz at -1 V and -2 V respectively for the Si-LPIN photodetector. The BL-VPIN photodetector has a much higher bandwidth of 48 GHz and 49 GHz at -1 V and -2 V respectively.

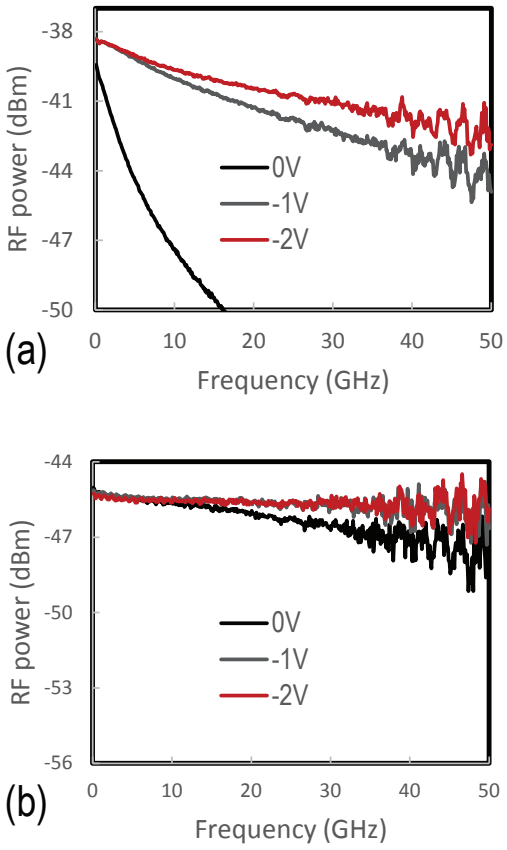

Figure 3.8: S21 traces at different bias voltages from small-signal RF measurements for (a) the Si-LPIN photodetector and (b) the BL-VPIN photodetector.

3.2.2.3 Large-signal measurements

Next, data transmission experiments were carried out. Light from a 1.55 μm laser was modulated with a 28 Gbps non-return to zero (NRZ) pseudo random bit sequence PRBS ($2^{31} - 1$ word length) by an external 44 Gbps $LiNbO_3$ modulator and detected by the Si-LPIN photodetector and BL-VPIN device. The bias voltage was applied to the photodetector using a 50 GHz RF probe connected to a 40 GHz bias-tee. The photocurrent output was measured with an Agilent oscilloscope with a 60 GHz remote sampling head plug-in. Eye diagrams of the Si-LPIN photodetector at -1 V and -2 V are shown in Fig. 10(a) and Fig. 10(b). In Fig. 10(c), the eye diagram of the BL-VPIN photodetector at -1 V is shown for reference. It

can be seen that the rise time and fall time in the eye diagrams of the Si-LPIN photodetector are longer than that in the eye diagram of the BL-VPIN photodetector, limited by the lower opto-electrical bandwidth. The clearly open eyes from the contact-free photodetector with low bias voltage at -1V and -2V indicate high performance data reception at 28 Gbps.

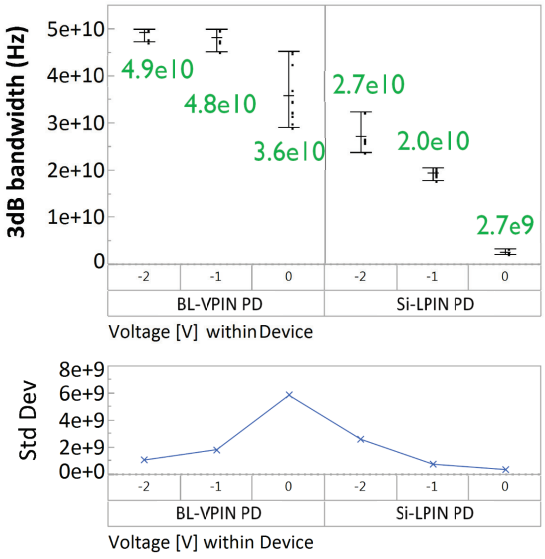

Figure 3.9: Wafer-scale opto-electrical 3dB bandwidth of the Si-LPIN photodetector and the BL-VPIN photodetector at 0V, -1V and -2V. The mean of the wafer-scale data is annotated explicitly in the graph; Standard deviations (std Dev) of the wafer-scale data is given separately.

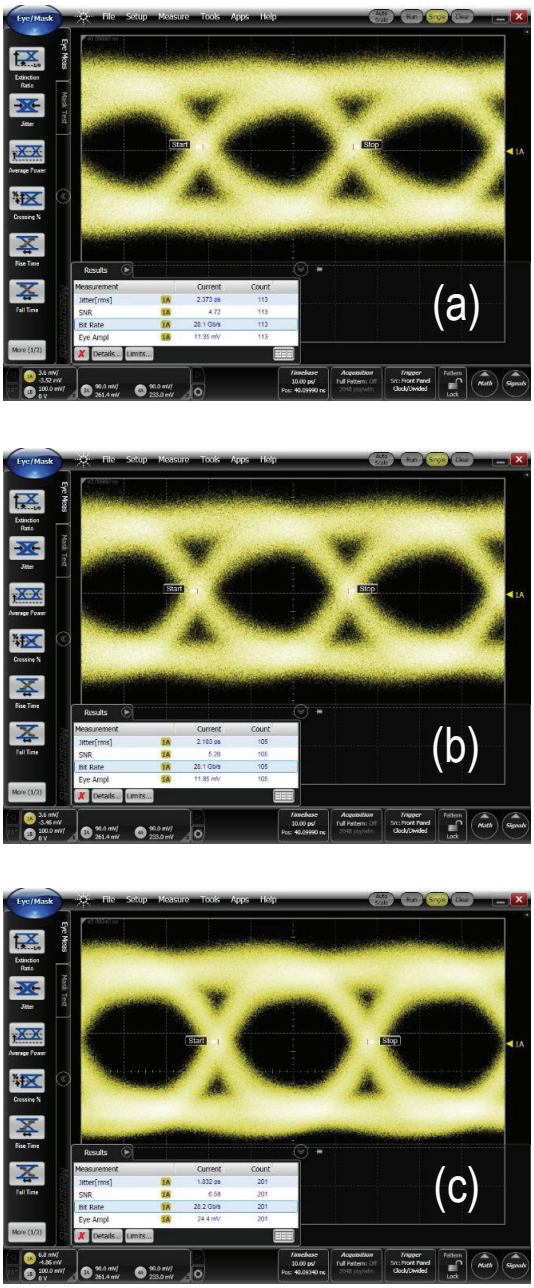

Figure 3.10: 28 Gbps eye diagrams of a Si-LPIN photodetector at (a) -1 V and (b) -2 V. (c). 28 Gbps eye diagram of a BL-VPIN photodetector at -1 V.

3.2.3 Discussion and Outlook

Wafer-scale opto-electrical 3-dB bandwidth data of Si-LPIN photodetectors with different germanium width between 0.4 μm and 0.7 μm are shown in Fig. 11. At 0 V and -1 V, the narrower the germanium width, the higher the 3-dB bandwidth. Since a quasi-lateral p+(Si)-i(Ge)-n+(Si) junction is formed in a Si-LPIN photodetector, changes in germanium width implies a change in the intrinsic region width in the p-i-n junction. The shorter carrier transit distance in the narrower devices results in a shorter transit time under the assumption that carriers drift at saturation velocity. This indicates that the bandwidth is mainly limited by the carrier transit time, which is further confirmed by the fact that the bandwidth increases as the bias voltage is increased (the electric field in the Ge is strengthened). At -2 V, the trend still holds for the last 3 devices, yet, the bandwidth of the first device is similar to that of the second device. This is attributed to the increase of the silicon junction capacitance.

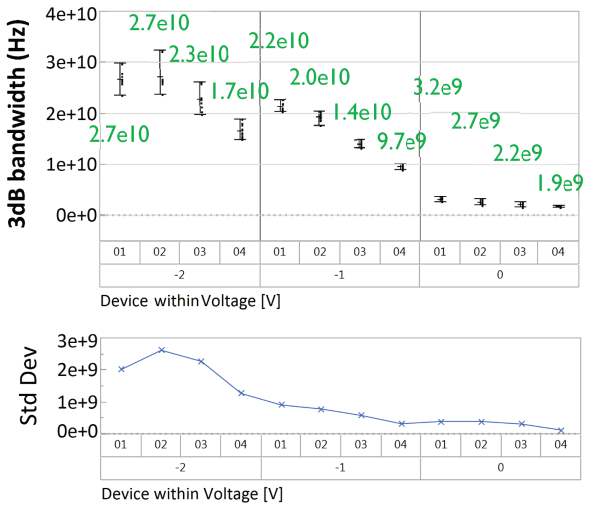

Figure 3.11: Wafer-scale opto-electrical 3dB bandwidth data of 4 Si-LPIN photodetectors with different germanium width at 0V, -1V and -2V. The width of germanium are 0.4 μm (device 01), 0.5 μm (device 02), 0.6 μm (device 03) and 0.7 μm (device 04). The mean of the wafer-scale data is annotated explicitly in the graph; Standard deviations (std Dev) of wafer-scale data variance are given separately.

It can be seen from Fig. 4(a) that electric field strength in the top part of germanium is weaker than that in the bottom. This weak field strength is not sufficient ($< 1 \times 10^4$ V/cm) for carriers to drift at their saturation velocity. At the same time, the carrier drift distance for carriers generated at the top of the germanium

is longer than that at the bottom. Thus, an effective approach to increase the Si-LPIN photodetector bandwidth is to reduce germanium thickness. With stronger electric field strength and shorter transit time after adopting thinner germanium, the dependence on narrower germanium to reduce transit time and thus to obtain high bandwidth can be removed. This will eliminate the upper bandwidth limit imposed by the large capacitance of the p-i-n junction formed in silicon.

3.3 160 nm-Ge Si-LPIN GePD

Although the 400 nm thick Ge Si-LPIN GePD shows high responsivity over 1 A/W across the whole C-band and a very low dark current of 3 nA at -1 V, the opto-electrical 3-dB bandwidth of the device was limited to 20 GHz at 1550 nm wavelength. Since this relatively low O/E bandwidth in the 400 nm thick Ge Si-LPIN GePD is limited by the transit time, a 160 nm thin Ge layer was adopted to reduce the transit time, and the opto-electrical 3-dB bandwidth at -1 V is enhanced to 67 GHz and 44 GHz at 1550 nm and 1310 nm, respectively. The junction capacitance is 6.8 fF at -1 V. The measured responsivity at -1 V is 0.74 A/W and 0.93 A/W at 1550 nm and 1310 nm respectively. The dark current is as low as 4 nA at -1 V. These device properties make it an attractive candidate for Si photonics optical interconnects. 56 Gbps on-off keying data reception is demonstrated with clear open eye diagrams at both 1550 nm and 1310 nm wavelength. The opto-electrical 3-dB bandwidth beyond 67 GHz at higher reverse bias enables even 100 Gbps on-off keying optical receivers.

3.3.1 Device Design and Fabrication

The Si-LPIN GePDs were fabricated in imec's fully integrated Si Photonics Platform along with Si modulators [12] and various passive devices. They go through a process flow described in [8]. Light is coupled from a 220 nm thick single-mode Si waveguide (450nm wide) to the germanium-on-SOI waveguide using a Si waveguide taper together with a 120 nm thick poly-Si taper, as shown in Fig. 12(a). The germanium layer dimensions and doping configuration in the Si-LPIN GePD are shown in Fig. 12(b). The doping distribution in the Si-LPIN GePD is shown in Fig. 13(a), simulated using Sentaurus Process. It should be mentioned that the poly-Si taper almost does not improve the Si-LPIN GePD responsivity. This is because all the light coupled across the SOI WG and Ge-on-Si WG interface will be fully absorbed by Ge. The coupling efficiency between the SOI WG and Ge-on-Si WG is very high (over 95%) without poly-Si taper.

The electric field distribution at -1 V obtained by numerically solving the Poissons equation using Sentaurus Device is shown in Fig. 13(b). In the germanium

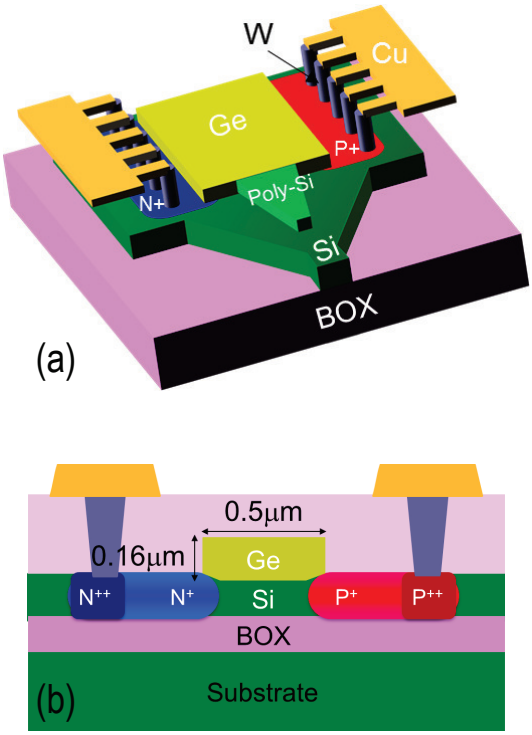

Figure 3.12: (a) 3-D schematic of the Si-LPIN GePD. (b) Cross sectional schematic of the Si-LPIN GePD with a 0.16 μm thick and 0.5 μm wide germanium layer.

region, the electric field is stronger than 10^4 V/cm at -1 V, strong enough for photo-generated carriers to drift at their saturation velocity.

3.3.2 Device Characteristics

3.3.2.1 Static measurements

A typical static current-voltage characteristic of a 14 μm long and 0.5 μm wide Si-LPIN GePD is shown in Fig. 14(a). The device exhibits a dark current as low as 2.5 nA and 3.5 nA at -1 V and -2 V. The light current was measured in the C-band at 1550 nm wavelength and in the O-band at 1310 nm wavelength under a received optical power of -5.8 dBm and -2.5 dBm, respectively. The received optical power is the optical power reaching the photodiode, with the fiber grating coupler insertion loss calibrated out using a reference straight waveguide beside the photodetector. The light current is almost constant from 0 V to -2 V owing to the strong built-in electric field that is capable of sweeping out the majority of the

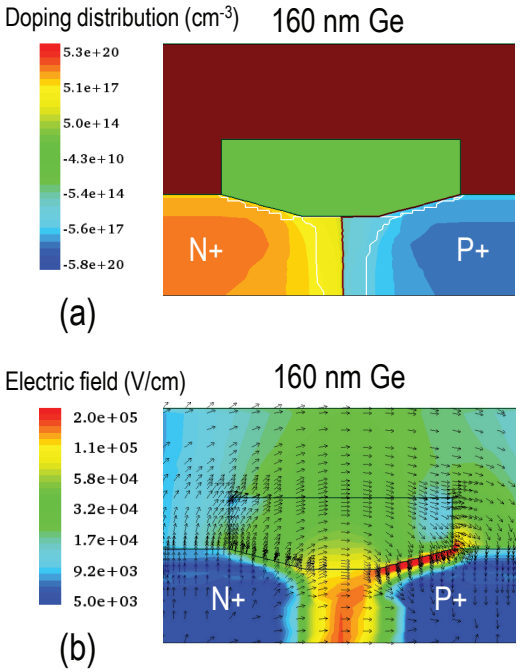

Figure 3.13: (a) Simulated doping distribution in the Si-LPIN GePD using Sentaurus Process. (b) Simulated electric field distribution in the Si-LPIN GePD at -1 V using Sentaurus Device. The electric field direction is annotated in the graph.

photo-generated carriers within their lifetime. The measured responsivity at -1 V is 0.72 A/W and 0.98 A/W at 1550 nm and 1310 nm, respectively.

Wafer-scale dark current data of the Si-LPIN GePD are shown in Fig. 14(b). The mean dark current value is 2.4 nA and 3.6 nA, with a standard deviation of 0.4 nA and 0.8 nA, at 1 V and 2 V, respectively. In Fig. 15(a) and Fig. 15(b), contour plots of the wafer-scale responsivity data of the Si-LPIN GePD at -1 V at 1550 nm and 1310 nm are shown. The mean responsivity value is 0.74 A/W and 0.93 A/W respectively, with a standard deviation of 0.05 A/W.

The wavelength dependence of the responsivity in the C-band and O-band at -1.2 V bias are shown in Fig. 16(a) and Fig. 16(b), respectively. Only responsivity data in a 40 nm optical bandwidth are shown, limited by the optical bandwidth of the fiber-to-chip grating coupler used to interface to the photodetector. The device has a higher responsivity in the O-band than in the C-band, due to the relatively short device length (14 μm) and the higher modal absorption coefficient in the O-band. The higher modal absorption coefficient in the O-band further results from

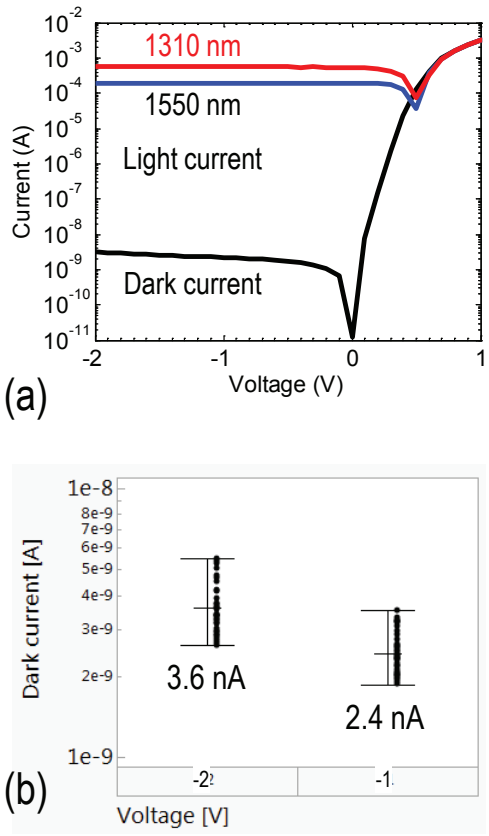

Figure 3.14: (a) A typical I-V characteristic of a 14.2 μm long and 0.5 μm wide Si-LPIN GePD. (b) Variability plot of the wafer-scale dark current data of the Si-LPIN GePD at -1 V and -2 V.

both the higher modal confinement factor in the germanium layer and the stronger material absorption coefficient in the germanium layer in the O-band. The drop in responsivity in the C-band is mainly due to the decrease of the germanium absorption coefficient at longer wavelength, as will be discussed later in section 4. It can be improved by increasing the length of the device (i.e. the germanium layer).

3.3.2.2 Small-signal measurements

Small-signal radio-frequency (RF) measurements were carried out at wafer scale using an Agilent 50 GHz vector network analyzer (*VNA*) N5225A and an Agilent 50 GHz lightwave component analyzer (*LCA*) N4373C to characterize the high-

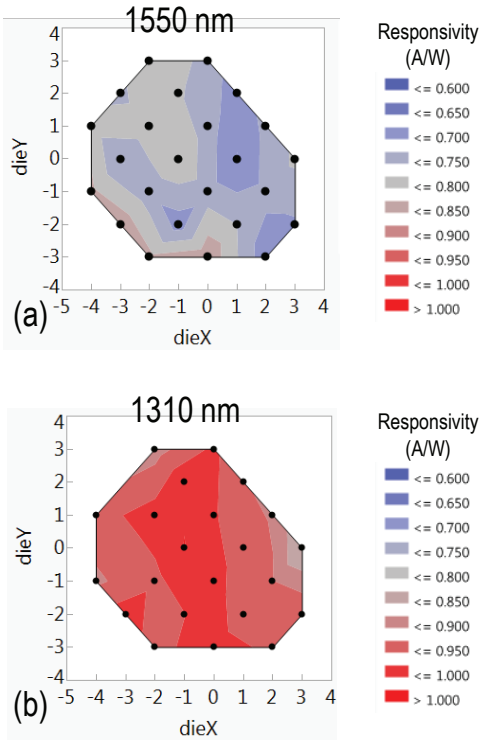

Figure 3.15: Contour plot of the wafer-scale responsivity data of the Si-LPIN GePD at (a) 1550 nm and (b) 1310 nm at -1 V.

speed performance of the Si-LPIN GePD. Typical S_{21} transmission parameters as a function of frequency, at 1550 nm and 1310 nm wavelength, using an received average optical power of -6 dBm and -5 dBm are shown in Fig. 17(a) and Fig. 17(b), respectively. The received average optical power is the average optical power reaching the photodiode. At -1 V, the device shows a 3-dB opto-electrical bandwidth of $>$50 GHz and 45 GHz at 1550 nm and 1310 nm, respectively. The opto-electrical bandwidth is further enhanced to over 50 GHz for both wavelengths as the bias voltage is increased to -2 V. The opto-electrical 3-dB bandwidth data extracted from the wafer-scale measurement S21 curves for both wavelengths are shown in Fig. 17(c). At 1550 nm wavelength, the wafer-scale 3-dB bandwidth is over 50 GHz at both 1 V and 2 V bias voltage. At 1310 nm, the wafer-scale 3-dB bandwidth is over 50 GHz at 2 V. At 1 V, the mean 3-dB bandwidth value is 44 GHz with a standard deviation of 2.2 GHz. The standard deviation of bandwidth for conditions where the bandwidth is beyond 50 GHz could not be measured due

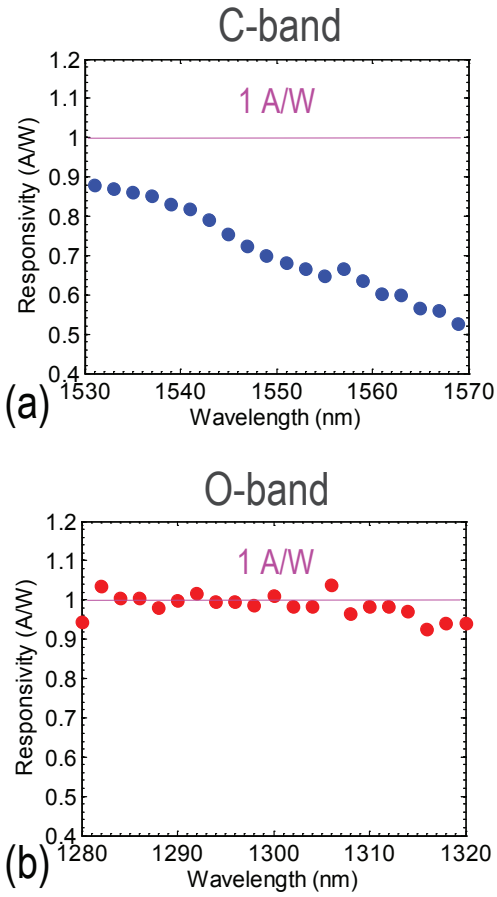

Figure 3.16: Responsivity as a function of wavelength of the Si-LPIN GePD in (a) the C-band and (b) the O-band at -1.2 V bias.

to the bandwidth limitation of the VNA/LCA.

The lower opto-electrical 3-dB bandwidth of the Si-LPIN GePD at 1310 nm can be attributed to the longer carrier transit time at this wavelength. This is because the photo-generated carrier density (in the first absorption length) in the device is much higher at 1310 nm than that at 1550 nm due to the much stronger germanium absorption coefficient at 1310 nm. The electric field is partly screened by the photo-generated carriers. Therefore, the photo-carriers experience a lower drift velocity and so a longer drift time at 1310 nm, leading to a lower bandwidth. This effect is especially pronounced at low bias voltage.

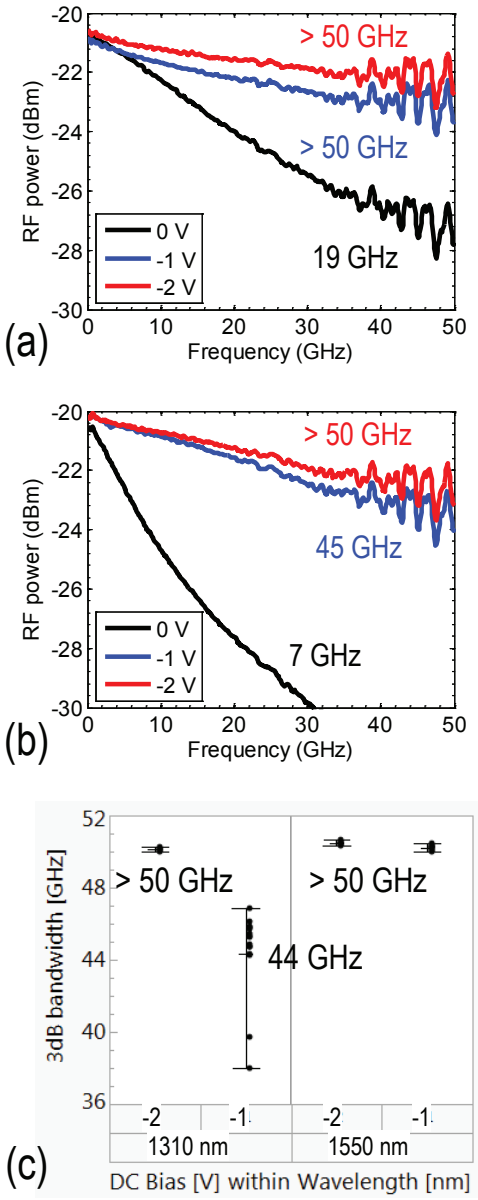

Figure 3.17: Small-signal S_{21} transmission parameter as a function of frequency of the Si-LPIN GePD at (a) 1550 nm and (b) 1310 nm wavelength. (c) Variability plot of wafer-scale opto-electrical 3-dB bandwidth data.

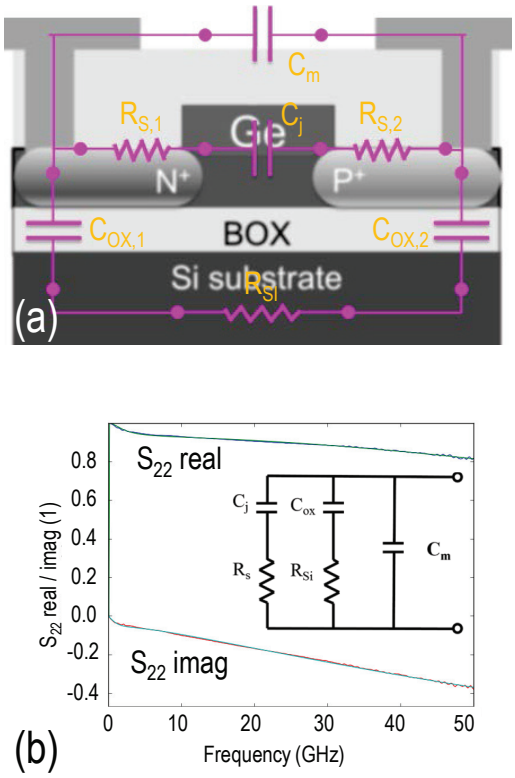

Figure 3.18: (a) Si-LPIN GePD circuit model. (b) Experimental and fitted real/imaginary part of the small-signal S_{22} reflection parameter. The inset is the equivalent circuit model used for the fitting derived from Fig. 18(a).

The photodiode capacitance of the Si-LPIN GePD was extracted by fitting the real/imaginary part of the S_{22} reflection parameters (measured at wafer scale) based on the equivalent circuit model as shown in the inset of Fig. 18(b). This equivalent circuit model was simplified from a physical circuit model of the Si-LPIN GePD as shown in Fig. 18(a). In the equivalent circuit model, C_j is the capacitance of the reverse biased p-i-n junction, and Rs is the series resistance related to the p-i-n junction. C_{OX} and R_{Si} are related to the current path through the silicon substrate and the buried oxide (BOX). C_m represents the metal pad capacitance. The metal pad capacitance C_m is firstly extracted by fitting the S_{22} parameter of an OPEN reference structure, which is 7 fF. Afterwards, using this C_m value, the full S_{22} parameter of the Si-LPIN GePD is fitted to extract the value of other components in the equivalent circuit model. The extracted junction capacitance (C_j) data and series resistance (R_s) data of the Si-LPIN GePD are shown in

Fig. 19(a) and Fig. 19(b). The mean junction capacitance value is 6.8 fF and 6.2 fF at -1 V and -2 V, respectively. The mean series resistance value is 103 Ω and 91 Ω at -1 V and -2 V, respectively. The parasitic capacitance and resistance data are shown in Fig. 19(c) and Fig. 19(d). One example of the experimental and fitted real/imaginary part of the S_{22} parameters is shown in Fig. 18 (b).

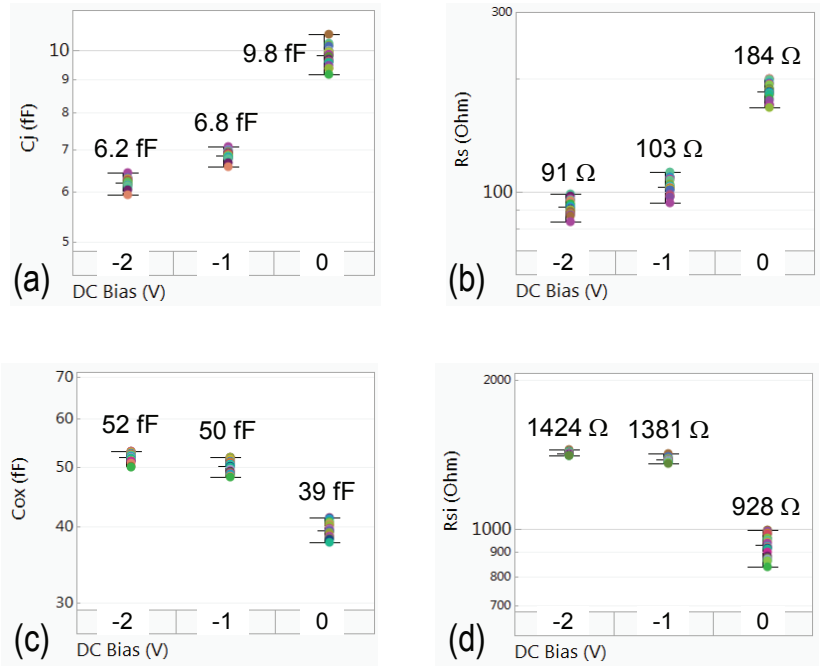

Figure 3.19: (a) Variability plot of the p-i-n junction capacitance data extracted from the fitting. (b) Variability plot of the series resistance data extracted from the fitting.

The opto-electrical bandwidth of the Si-LPIN GePD was further characterized for individual devices using an Agilent 67 GHz VNA E8361A and an Agilent 67 GHz LCA N4373B at 1550 nm wavelength at Eindhoven University of Technology. The measured S_{21} curves using an average received optical power of -5.5 dBm are shown in Fig. 20(a). At -1 V, the device shows a 3-dB opto-electrical bandwidth of 67 GHz, and the bandwidth is enhanced to beyond 67 GHz as the bias voltage is increased to -2 V and -3 V. The dip around 15 GHz and the fast roll off between 64∼67 GHz appearing on the S_{21} curves are attributed to the calibration of the VNA together with RF cables and RF probe used in the experiment. The impact of the optical input power on the opto-electrical bandwidth of the Si-LPIN GePD was also characterized using an Erbium-doped Fiber Am-

plifier (EDFA) together with a Variable Optical Attenuator (VOA) to control the input optical power. The measured opto-electrical 3-dB bandwidth as a function of the input optical power is shown in Fig. 20(b). A drop in the bandwidth can be observed at higher optical input powers, which is attributed to a screening of the internal electrical field in the photodetector due to the photo-generated carriers. This effect is especially pronounced at low bias voltages. It can be seen that at a bias voltage larger than -1 V, there is almost no drop of 3-dB bandwidth under an input optical power smaller than 1.3 mW.

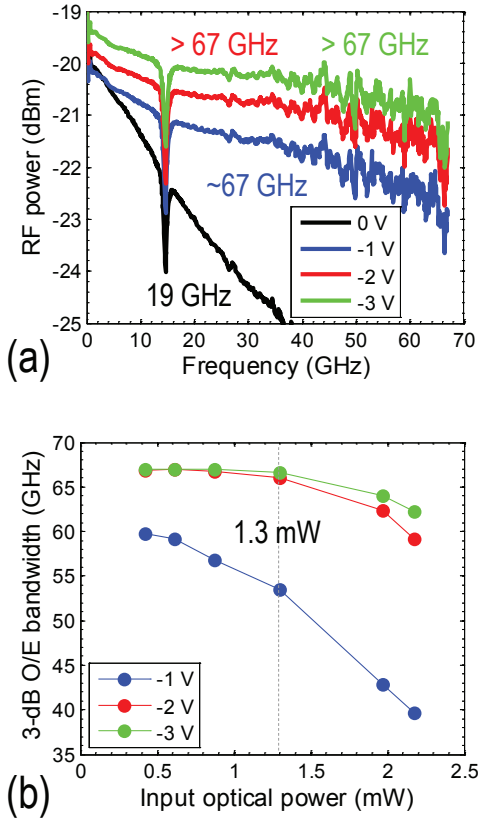

Figure 3.20: (a) Small-signal S21 transmission parameter as a function of frequency of the Si-LPIN GePD at 1550 nm. (b) Measured 3-dB opto-electrical bandwidth as a function of input optical power at 1550 nm.

3.3.2.3 56 Gbps large-signal measurements

On-off keying data reception experiments were implemented. A $(2^{31} - 1)$ long optical non-return to zero (NRZ) pseudo random bit sequence (PRBS) data pattern at 50 Gbps and 56 Gbps, generated by a commercial $LiNbO_3$ modulator at 1550 nm was launched into the Si-LPIN GePD (56 Gbps is the upper limit of the pulse pattern generator operation range). A -1 V bias voltage was applied to the photodetector using a 50 GHz RF probe connected to a 40 GHz bias-tee. The output electrical data was measured with an Agilent infiniium sampling oscilloscope with a 60 GHz remote sampling head plug-in. The 50 Gbps and 56 Gbps reference transmitter eyes at 1550 nm wavelength are shown in Fig. 21(a-b). The electrical eye diagrams from the Si-LPIN photodetector at -1 V are shown in Fig. 21(c-d). The same experiment was also implemented at 1310 nm wavelength as shown in Fig. 22(a-d). The clear open electrical eye diagrams from the Si-LPIN GePD at -1 V indicate the high quality data reception performance of the Si-LPIN GePD at 56 Gbps, in both the C-band and O-band.

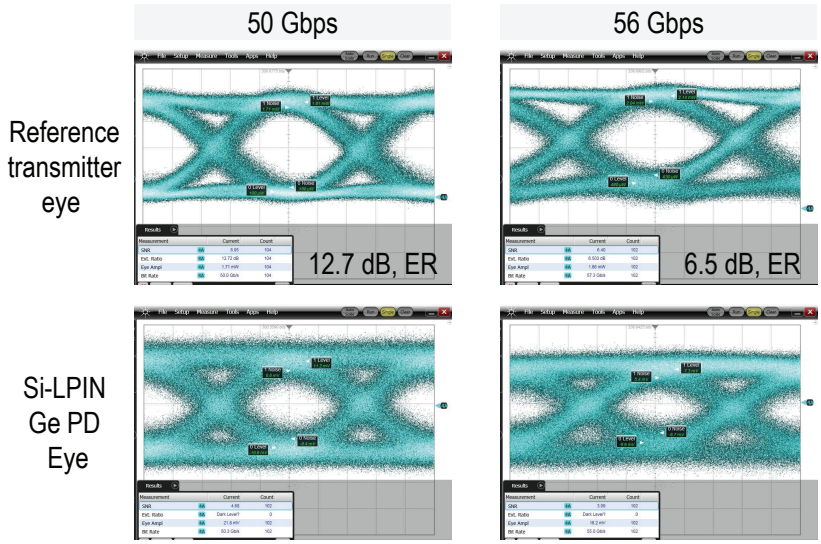

Figure 3.21: The optical eye generated from a 1550 nm commercial $LiNbO_3$ Mach-Zehnder modulator at (a) 50 Gb/s and (b) 56 Gb/s. The corresponding electrical eye from the Si-LPIN GePD at -1 V bias at (c) 50 Gb/s and (d) 56 Gb/s.

3.3.2.4 100 Gbps Large-signal measurements

The data reception performance was also characterized at 1550 nm wavelength using an on-off keying (OOK) return-to-zero (RZ) pseudo-random-bit-sequence

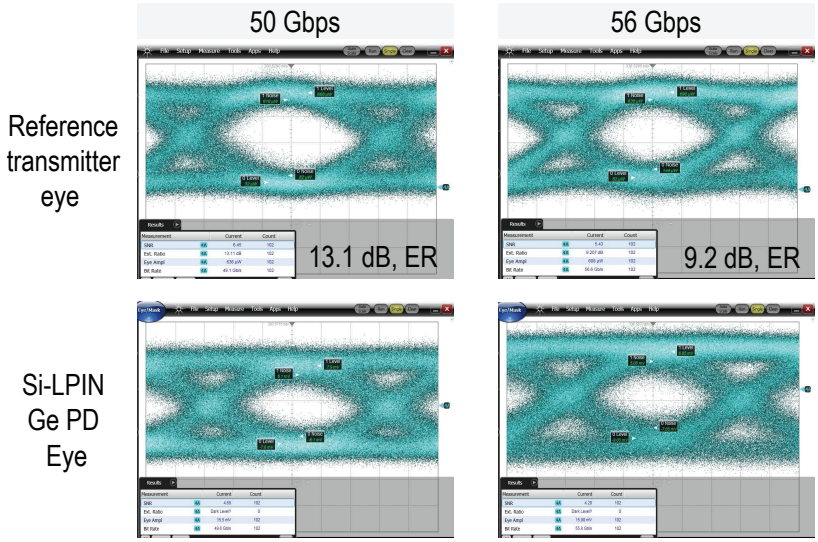

Figure 3.22: The optical eye generated from a 1310 nm commercial $LiNbO_3$ Mach-Zehnder modulator at (a) 50 Gb/s and (b) 56 Gb/s. The corresponding electrical eye from the Si-LPIN GePD at -1 V bias at (c) 50 Gb/s and (d) 56 Gb/s.

(PRBS) data pattern at 80 Gbps and 100 Gbps, respectively at Technical University of Denmark. Schematic diagrams illustrating the experimental setup generating the optical OOK RZ data stream at 80 Gbps and 100 Gbps are shown in Fig. 23(a) and Fig. 23(b) [16, 17]. Optical pulses from a 10 GHz mode-locked laser (MLL) are on-off keying (OOK) modulated by a commercial Mach-Zehnder modulator at 10 Gbps. The modulated pulses are temporally multiplexed 3 times with delays of 50 ps, 25 ps and 12.5 ps to generate the 80 Gbps data stream. For the 100 Gbps data stream generation, the modulated pulses are firstly multiplexed 2 times with delays of 40 ps and 20 ps. The generated optical pulses are then multiplexed with the original 10 Gbps optical pulses with an 80-ps delay forming a 50 Gbps OOK signal. This is finally multiplexed with a 10-ps delay to create the targeted data rate of 100 Gbps. The OTDM data stream is injected in the silicon waveguide using a C-band fiber-to-chip grating coupler. A bias voltage was applied to the Si-LPIN GePD using a 67 GHz Picoprobe RF probe with a 50 Ω terminator connected to a 65 GHz SHF bias-tee. The electrical output is measured with an Agilent Infiniium sampling oscilloscope with a 70 GHz remote sampling head plug-in.

The reference eye diagram of the 80 Gbps PRBS data pattern measured using a 70 GHz commercial p-i-n photodetector (u2t XPDV-3120R) is shown in Fig. 24(a). The extinction ratio of the transmitted data stream is 12.7 dB. The electrical eye diagrams from the Si-LPIN GePD at -1 V and -2 V are shown in Fig. 24(b)

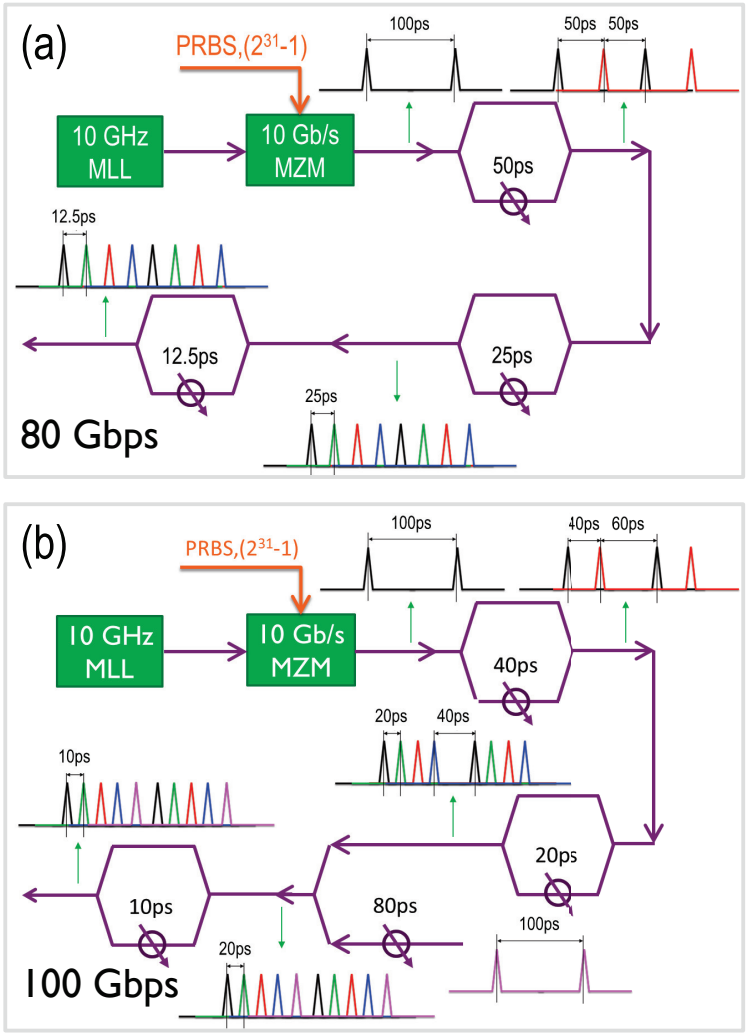

Figure 3.23: Schematic diagrams illustrating the experimental set up generating the optical OOK RZ data streams at (a) 80 Gbps and (b) 100 Gbps. MLL: mode-lock laser; MZM: Mach-Zehnder modulator.

and Fig. 24(c), respectively. Fig. 25(a-c) show the eye diagrams measured in the 100 Gbps data reception experiment. The extinction ratio of the transmitted data stream is 14.6 dB in this case. The average waveguide-coupled optical power used in both the 80 Gbps and 100 Gbps experiment is 0.62 mW. The corresponding 3-dB O/E bandwidth of the Si-LPIN GePD is 59 GHz at -1 V as seen in Fig. 20(b). This explains the bandwidth limitation at -1 V bias especially in the 100 Gbps eye

diagram. This bandwidth limitation is overcome by biasing the device at -2 V, where the Si-LPIN GePD exhibits a 3-dB O/E bandwidth beyond 67 GHz.

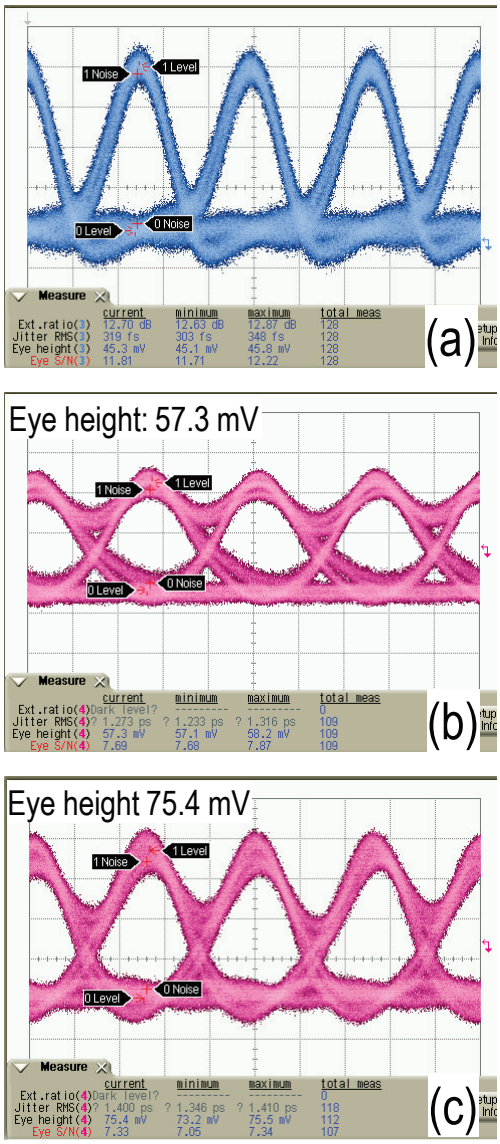

Figure 3.24: The 80 Gbps RZ eye diagram measured using (a) a 70 GHz commercial p-i-n photodetector (u2t XPDV 3120R), (b) the Si-LPIN GePD at -1 V bias, (c) the Si-LPIN GePD at -2 V bias.

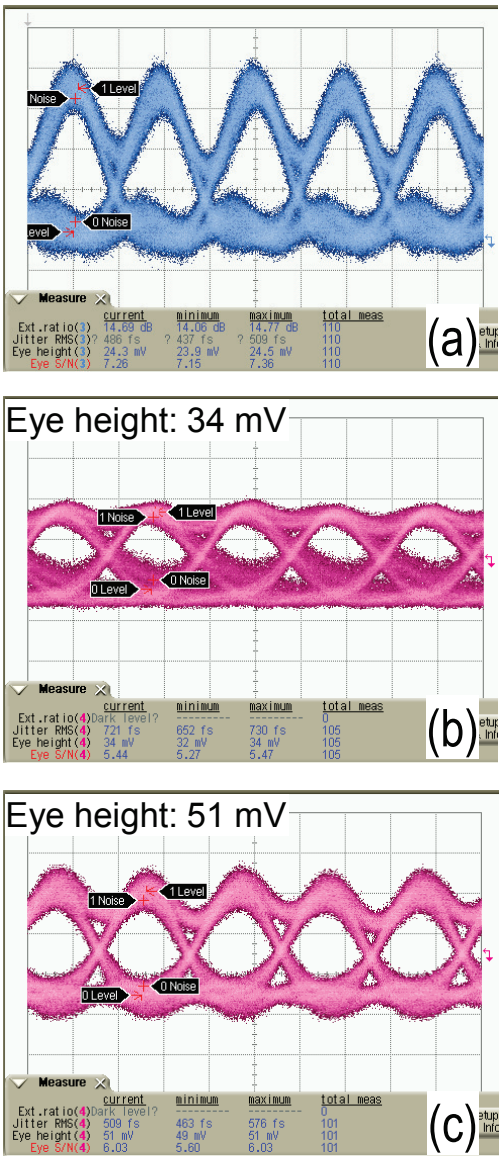

Figure 3.25: The 100 Gbps RZ eye diagram measured using (a) a 70 GHz commercial p-i-n photodetector (u2t XPDV 3120R), (b) the Si-LPIN GePD at -1 V bias. (c) the Si-LPIN GePD at -2 V bias.

3.3.3 Discussion and Outlook

The frequency response of the equivalent circuit in Fig. 18(b) exhibits a 3-dB bandwidth of 120 GHz and 140 GHz at -1 V and -2 V assuming a 50 Ω load. Comparing these values to the experimental data reveals that the opto-electrical bandwidth of the Si-LPIN GePD is limited by the carrier transit time instead of the RC-constant. It can be seen from Fig. 13(b) that the photo-carriers will drift along the electric field in a non-linear trajectory before being collected. Moreover, certain photo-carriers will hit the top surface and/or the sidewall of the germanium layer in the drifting. This will increase the transit time compared to the simple case where photo-carriers drift in a straight line.

It can be seen from Fig. 13(b) that the thicker the germanium layer, the longer the carrier transit time in the Si-LPIN GePD device will be, and thus the lower the opto-electrical bandwidth. This is clear from Fig. 26(a), comparing the experimental S_{21} curves for a germanium layer thickness of 160 nm and 400 nm (with the same the same germanium width of 500 nm). On the other hand, the modal absorption coefficient is larger for a device with a thicker germanium layer due to the larger modal confinement factor in the germanium layer. Therefore, the Si-LPIN GePD with a 400 nm thick germanium layer has a higher responsivity than that of the device with a 160 nm thick germanium layer (14.2 μm long), as shown in Fig. 26(b). Fig. 26 indicates that the germanium layer thickness can be designed to optimize the opto-electrical bandwidth or responsivity performance of a Si-LPIN GePD device.

The increased overlap of the optical mode with the doped silicon layers in the thin Ge device cannot account for the reduced responsivity at 1550 nm. Light absorption from the doped Si regions was quantified through optical simulation. At 1310 nm, the confinement factor of the fundamental optical mode in the Ge-on-SOI waveguide is 0.79 and 0.076 in the germanium layer and the doped Si layer (both N-doped region and P-doped region), respectively. Assuming a germanium material absorption coefficient of 7000 cm^{-1} and a N/P-doped Si absorption coefficient of 18 cm^{-1}/60 cm^{-1} [18], the modal absorption coefficient related to germanium absorption and doped Si absorption is 5538 cm^{-1} and 3.0 cm^{-1}, respectively. The same exercise is done at 1550 nm, and the (fundamental mode) modal absorption coefficient related to germanium absorption and the doped Si absorption is 1025 cm^{-1} and 7.5 cm^{-1}, respectively. The share of doped Si absorption in the total modal absorption coefficient is 0.05% and 0.73% at 1310 nm and 1550 nm, respectively. Although the doped Si absorption contributes more at 1550 nm than that at 1310 nm in the total modal absorption, its low absolute contribution (0.72% at 1550 nm) cannot explain the responsivity drop at long wavelength. Therefore, since the opto-electrical bandwidth is limited by the carrier transit time, the responsivity of the 160 nm thick Si-LPIN GePD at 1550 nm can be improved by increasing the length of the device without compromising on the

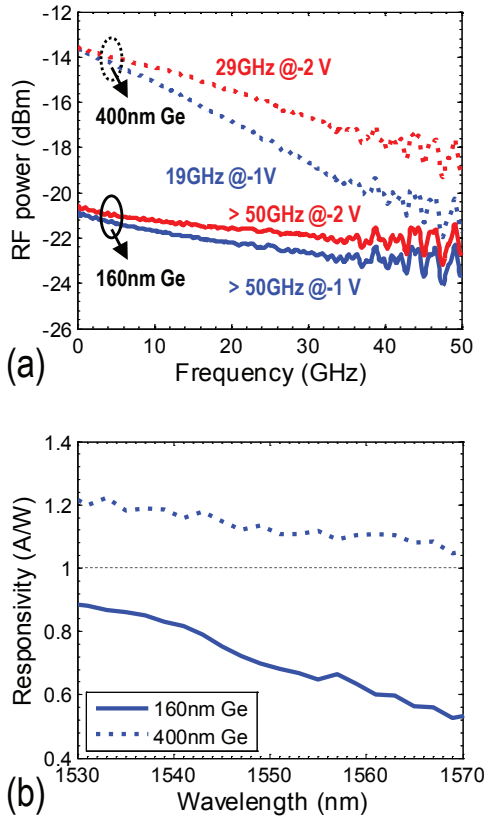

Figure 3.26: (a) Small-signal S21 transmission parameters as a function of frequency at 1550 nm of the Si-LPIN GePD with a 400 nm thick Ge layer and a 160 nm thick Ge layer. (b) Responsivity as a function of wavelength in the C-band of the Si-LPIN GePD with a 400 nm thick Ge layer and a 160 nm thick Ge layer. The only difference between the 2 Si-LPIN GePD devices is the germanium layer thickness.

opto-electrical bandwidth.

A further optimization of the design in O-band is to increase the O/E bandwidth by adopting an even thinner Ge layer. A further optimization of the design in C-band is to increase the responsivity potentially by increasing the device length. A 20 μm long 160 nm-Ge Si-LPIN GePD was characterized. The primary responsivity at 1550 nm was improved to 0.92 A/W. Similarly open eye diagrams were obtained at 80 Gb/s and 100 Gb/s.

3.4 Conclusion

Two version Si-contacted Ge p-i-n photodetectors were reported. The 400 nm Si-LPIN GePD shows a high responsivity over 1 A/W in the whole C-band at -1 V. The 160 nm SI-LPIN GePD shows a high 3-dB opto-electrical bandwidth over 67 GHz at -1 V. The dark current is $<$5 nA for both versions at -1 V bias. The performance of both Si-LPIN GePDs at 1550 nm are benchmarked as shown in Fig. 27(a) and Fig. 27(b). The Si-LPIN GePDs show a large O/E bandwidth, a ultra-low dark current with a relatively high responsivity.

The presented Si-contacted Ge p-i-n photodetectors design is expected to enable a good device performance (responsivity, O/E bandwidth and dark current) by properly designing the Ge layer thickness and length.

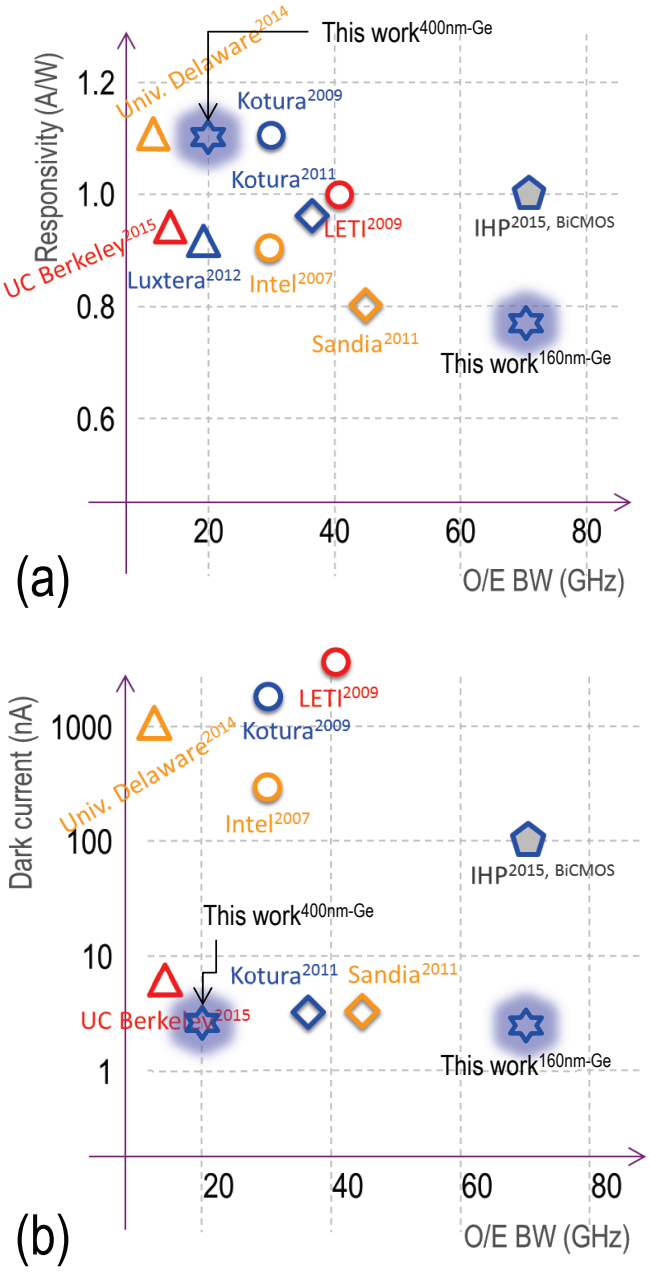

Figure 3.27: Si-LPIN GePDs benchmarking. (a) Responsivity versus the 3-dB O/E bandwidth, and (b) dark current versus the 3-dB O/E bandwidth.

References

[1] Hong Tao Chen, Peter Verheyen, Peter De Heyn, Guy Lepage, Jeroen De Coster, Philippe Absil, Gunther Roelkens, and Joris Van Campenhout. *High-Responsivity Low-Voltage 28-Gb/s Ge p-i-n Photodetector With Silicon Contacts*. J. Lightwave Technol., 33(4):820–824, feb 2015.

[2] H Chen, P Verheyen, P De Heyn, G Lepage, J De Coster, S Balakrishnan, P Absil, W Yao, L Shen, G Roelkens, and J Van Campenhout. *-1 V bias 67 GHz bandwidth Si-contacted germanium waveguide p-i-n photodetector for optical links at 56 Gbps and beyond*. Opt. Express, 24(5):4622–4631, mar 2016.

[3] Jifeng Liu, Dong Pan, Samerkhae Jongthammanurak, Kazumi Wada, Lionel C Kimerling, and Jurgen Michel. *Design of monolithically integrated GeSi electro-absorption modulators and photodetectors on a SOI platform.* Optics express, 15(2):623–628, 2007.

[4] Tao Yin, Rami Cohen, Mike M Morse, Gadi Sarid, Yoel Chetrit, Doron Rubin, and Mario J Paniccia. *31 GHz Ge n-i-p waveguide photodetectors on Silicon-on-Insulator substrate.* Optics express, 15(21):13965–13971, 2007.

[5] Laurent Vivien, Andreas Polzer, Delphine Marris-Morini, Johann Osmond, Jean Michel Hartmann, Paul Crozat, Eric Cassan, Christophe Kopp, Horst Zimmermann, and Jean Marc Fédéli. *Zero-bias 40Gbit/s germanium waveguide photodetector on silicon*. Optics Express, 20(2):1096, 2012.

[6] Shirong Liao, Ning-Ning Feng, Dazeng Feng, Po Dong, Roshanak Shafiiha, Cheng-Chih Kung, Hong Liang, Wei Qian, Yong Liu, Joan Fong, John E Cunningham, Ying Luo, and Mehdi Asghari. *36 GHz submicron silicon waveguide germanium photodetector.* Optics Express, 19(11):10967–10972, 2011.

[7] Christopher T. DeRose, Douglas C. Trotter, William a. Zortman, Andrew L. Starbuck, Moz Fisher, Michael R. Watts, and Paul S. Davids. *Ultra compact 45 GHz CMOS compatible Germanium waveguide photodiode with low dark current*. Optics Express, 19(25):24897, 2011.

[8] Peter Peter Verheyen, Marianna Pantouvaki, Joris Van Campenhout, Philippe P Absil, Hongtao Chen, Peter De Heyn, Guy Lepage, Jeroen De Coster, Pieter Dumon, Adil Masood, Dries Van Thourhout, Roel Baets, and Wim Bogaerts. *Highly Uniform 25 Gb/s Si Photonics Platform for High-Density, Low-Power WDM Optical Interconnects*. In Advanced Photonics for Communications, page IW3A.4. Optical Society of America, 2014.

[9] Philippe P Absil, Peter Verheyen, Peter De Heyn, Marianna Pantouvaki, Guy Lepage, Jeroen De Coster, and Joris Van Campenhout. *Silicon photonics integrated circuits: a manufacturing platform for high density, low power optical I/O's*. Opt. Express, 23(7):9369–9378, apr 2015.

[10] Laurent Vivien, Johann Osmond, Jean-Marc Fédéli, Delphine Marris-Morini, Paul Crozat, Jean-François Damlencourt, Eric Cassan, Y Lecunff, and Suzanne Laval. *42 GHz p.i.n Germanium photodetector integrated in a silicon-on-insulator waveguide.* Optics Express, 17(8):6252–7, 2009.

[11] Guoliang Li, Ying Luo, Xuezhe Zheng, Gianlorenzo Masini, Attila Mekis, Subal Sahni, Hiren Thacker, Jin Yao, Ivan Shubin, Kannan Raj, John E Cunningham, and Ashok V Krishnamoorthy. *Improving CMOS-compatible Germanium photodetectors.* Optics express, 20(24):26345–50, 2012.

[12] M Pantouvaki, P Verheyen, G Lepage, J De Coster, H Yu, P De Heyn, P Absil, and J Van Campenhout. *20Gb/s silicon ring modulator co-integrated with a Ge monitor photodetector*. In Optical Communication (ECOC 2013), 39th European Conference and Exhibition on, pages 1–3, sep 2013.

[13] Yi Zhang, Shuyu Yang, Yisu Yang, Michael Gould, Noam Ophir, Andy Eu-Jin Lim, Guo-Qiang Lo, Peter Magill, Keren Bergman, Tom Baehr-Jones, and Michael Hochberg. *A high-responsivity photodetector absent metal-germanium direct contact*. Optics Express, 22(9):11367, 2014.

[14] Ryan Going, Tae Joon Seok, Jodi Loo, Kyle Hsu, and Ming C. Wu. *Germanium wrap-around photodetectors on Silicon photonics*. Optics Express, 23(9):11975, 2015.

[15] Stefan Lischke, Dieter Knoll, Christian Mai, Lars Zimmermann, Anna Peczek, Marcel Kroh, Andreas Trusch, Edgar Krune, Karsten Voigt, and A. Mai. *High bandwidth, high responsivity waveguide-coupled germanium p-i-n photodiode*. Optics Express, 23(21):27213, 2015.

[16] Michael Galili, Hans Christian Hansen Mulvad, Hao Hu, Leif Katsuo. Oxenløwe, Fausto Gomez Agis, Cedric Ware, Didier Erasme, Anders Thomas. Clausen, and Palle Jeppesen. *650 Gbit/s OTDM Transmission over 80 km*

SSMF Incorporating Clock Recovery, Channel Identification and Demultiplexing in a Polarisation Insensitive Receiver. In Optical Fiber Communication Conference, page OWO3. Optical Society of America, 2010.

[17] Hao Hu, Janaina Laguardia Areal, Hans Christian Hansen Mulvad, Michael Galili, Kjeld Dalgaard, Evarist Palushani, Anders T Clausen, Michael Stübert Berger, Palle Jeppesen, and Leif K Oxenlowe. *Synchronization, retiming and OTDM of an asynchronous 10 Gigabit Ethernet NRZ packet using a time lens for Terabit Ethernet*. In 37th European Conference and Exposition on Optical Communications, page Tu.3.K.4. Optical Society of America, 2011.

[18] Jifeng Liu, Xiaochen Sun, Dong Pan, Xiaoxin Wang, Lionel C Kimerling, Thomas L Koch, and Jurgen Michel. *Tensile-strained, n-type Ge as a gain medium for monolithic laser integration on Si.* Optics express, 15(18):11272–11277, 2007.

4

Low-voltage Ge Waveguide VPIN Avalanche Photodetectors

By leveraging the internal gain of the avalanche photodetectors, optical receivers can be realized with significantly improved optical sensitivity as compared to p-i-n photodetector receivers. This will greatly improve the power budget of Si-based optical interconnects.

In this chapter, 2 versions of low voltage vertical p-i-n (VPIN) Ge APDs will be presented, which have been published in [1, 2]. They have similar design but different Ge layer thickness, 400 nm and 185 nm. This VPIN Ge APD design comes from an exploration of efficient Ge APD designs compatible with imec's Si photonics platform. The 400 nm thick Ge VPIN APD shows a gain$\times$bandwidth product above 100 GHz. A photonic receiver based on such a Ge APD, including a 0.13 μm SiGe BiCMOS low-noise trans-impedance amplifier and a limiting amplifier, was realized. A 5.8 dB sensitivity improvement is demonstrated at -5.9 V bias at an avalanche gain of 6 through bit error rate measurements. The absolute sensitivity in avalanche mode is -23.4 dBm and -24.4 dBm at a bit error rate of 1×10^{-12} and 1×10^{-9} respectively.

The 185 nm thick Ge VPIN APD shows a gain$\times$bandwidth product of 140 GHz at -5 V bias. A low effective k-value (the ratio of holes impact ionization rate to electrons impact ionization rate) of 0.2 is demonstrated from multiplication noise measurements. A 20 Gbps 1310 nm optical receiver based on such a Ge APD shows a 6.2 dB avalanche sensitivity improvement at -5.0 V APD bias, and operation of the receiver up to 25 Gbps is demonstrated.

4.1 Ge APD design exploration

Imec's Si Photonics Platform was introduced in chapter 1. In this platform, 100% Ge is selectively grown in SiO_2 trenches on the 220 nm Si layer of a SOI wafer. After chemical-mechanical planarization, the Ge layer is ion implanted followed by the contact module to define Ge photodetectors. A Ge/Si Separated-Absorption-Charge-Multiplication (SACM) structure, introduced in chapter 1, has been proved to be an effective Ge APD design to construct highly sensitive optical receivers [3–7]. However, the SACM Ge/Si APD is impossible to realize on imec Si Photonics Platform. This is because the Ge/Si SACM APD requires an additional crystalline Si layer grown on top of the 220 nm crystal Si in the SOI wafer. This additional Si layer will then be ion implanted to function as both the charge layer and the multiplication layer of a Ge/Si SACM APD. This additional Si epitaxy module on top of the 220 nm Si layer of a SOI wafer does not exist for the imec Si Photonics Platform. Therefore, a study was done to explore effective Ge APD designs compatible with imec Si Photonics Platform. In this section, such a Ge APD design exploration will be presented.

4.1.1 Metal-Semiconductor-Metal Ge APD

High avalanche gain up to 10 at a low voltage (-3 V) was reported [8] in waveguide APDs comprised of a thin Ge layer with metal-semiconductor-metal (MSM) contacts, as shown in Fig. 1. Strongly non-uniform electric fields generated by the interdigitated contacts were exploited to mitigate the intrinsically poor avalanche excess-noise properties of bulk Ge. The measured k-value is 0.2. However, the large dark current of the MSM device and poor primary responsivity strongly limited the receiver sensitivity to -13.9 dBm at a BER of 1×10^{-9} at 10 Gbps.

In order to reduce the intrinsic large dark current originating from the thermal emission from the Schottky-barrier junction, a thin barrier-enhancement layer needs to be added between Ge and the contact metal. This is however difficult to implement from process point of view.

4.1.2 Lateral p-i-n Ge APD

A lateral p-i-n junction Ge waveguide APD with gain larger than 10 at a bias voltage of -7 V was reported in [9], as shown in Fig. 2. The device shows a low dark current of 18 nA at -1 V. The simple fabrication process of the device and its promising performance make it a good Ge APD design on imec Si Photonics Platform.

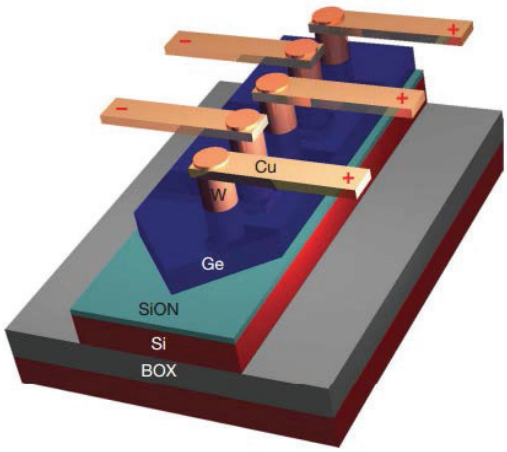

Figure 4.1: Low-voltage MSM waveguide Ge APD demonstrated by IBM [8].

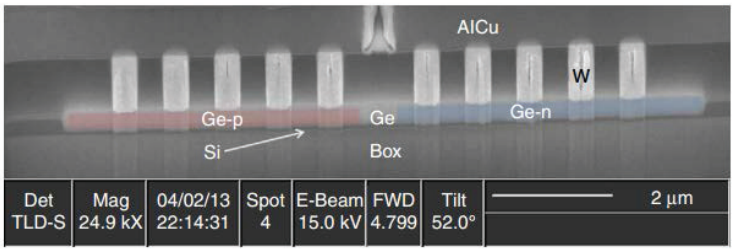

Figure 4.2: Lateral p-i-n Ge APD demonstrated by Université Paris-Sud [9].

The simulated electric field distribution in a lateral p-i-n diode using *Sentaurus Sdevice* is shown in Fig. 3 (b). The Ge layer thickness is 400 nm, and the pitch between the anode and cathode is 800 nm. The structure was generated in *Sentaurus Sprocess* as shown in Fig. 3(a). The doping distribution is created by Monte-Carlo ion implantation simulation using process dose/energy parameters. It can be seen that the electric field in the p-i-n junction around the Ge top surface is $\sim 2 \times 10^5$ V/cm, where photo-carriers are expected to ionize.

The static current-voltage characteristic of a Ge photodetector based on such a lateral p-i-n diode is shown in Fig. 4. The I-V measurement was done for 5 times continuously. In the I-V curve measured for the first time, strong current increase when the voltage is increased over -4 V is observed, which can be potentially attributed to the avalanche multiplication due to the carriers ionizing in the strong electric field region as seen in Fig. 3(b). However, the dark current increases sig-

nificantly as a whole in the I-V curves measured in the following 4 times compared to that measured in the first time. We attribute this to the burn-in effect at the Ge top surface where there is a strong electric field. The Ge top surface is not well passivated by the silicon dioxide, and the non-passivated dangling bonds introduce a high interface-state density at Ge/SiO_2 interfaces [10]. Electrons/holes trapping centers are excited under strong electric field from these interface states, and these electrical traps become effective leakage current channels through the Shockley-Read-Hall process and Traps-Assisted Tunneling process. This explains the current increase as a whole in the I-V curve measured for the following 4 times. As it is difficult to achieve a good Ge passivation using a standard and simple process, the lateral p-i-n structure is not considered as a good Ge APD design.

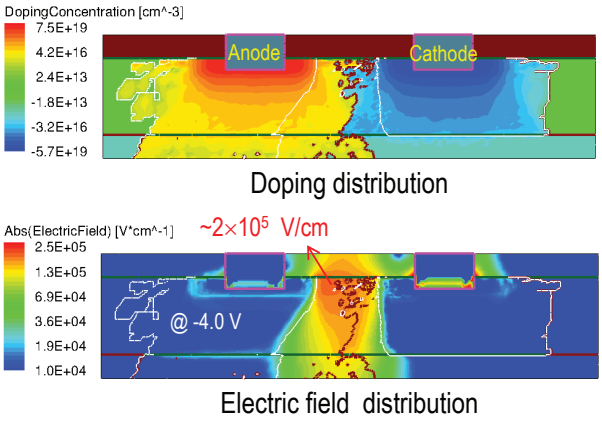

Figure 4.3: (a) Lateral p-i-n diode doping distribution. (b) Lateral p-i-n diode electric field distribution at -4 V.

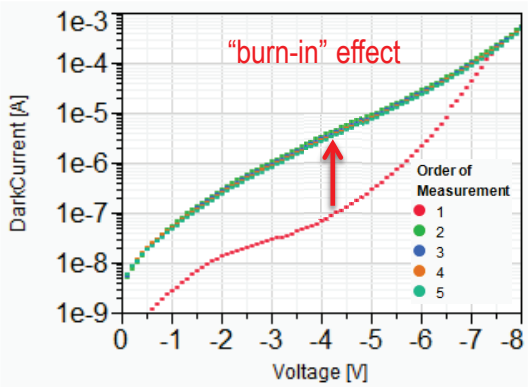

Figure 4.4: Current-voltage characteristic of a lateral p-i-n diode. The I-V measurement was done on the same diode for 5 times continuously.

4.1.3 Vertical p-i-n Ge APD

The VPIN GePDs presented in chapter 2 confines a strong electrical field at the bottom of Ge layer. This electric field is over 1×10^5 V/cm at -5.5 V bias for a 400 nm thick Ge layer. This should allow for a substantial avalanche multiplication. Therefore we focus on Ge VPIN structures to realize Ge APDs. Two designs will be explored: one with a 400 nm thick Ge layer and the other with a 185 nm thick Ge layer.

4.2 400 nm-Ge VPIN Ge APD

4.2.1 Device structure and fabrication process

The Ge waveguide APDs are implemented in imec's fully integrated Si Photonics Platform along with Si modulators [11] and various passive devices [12]. They go through a process flow described in [13]. The cross-sectional dimensions of the Ge APD are shown in Fig. 5(a). Fig. 5(b) shows a TEM image of the Ge APDs longitudinal cross section. The spacing between the p-contact plugs is 1.2 μm. With phosphorus ion implantation in silicon before Ge epitaxy and boron ion implantation in the planarized Ge layer, a vertical P+-I-N+ (VPIN) diode is formed. The simulated doping distribution (Monte Carlo ion implantation simulation) in the Ge layer is shown in Fig. 6(a). This heterogeneous Ge/Si VPIN diode configuration results in a strong electric field as high as 1×10^5 V/cm confined in the lower 200 nm of the Ge layer at -5.5 V bias voltage, as shown in Fig. 6(b). Hence, it is expected that strong avalanche multiplication can take place at moderate applied bias voltage, and that part of the avalanche excess-noise generation can be

suppressed [8, 15–17].

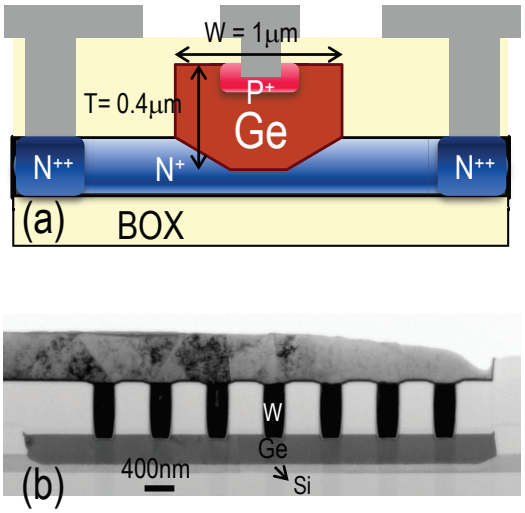

Figure 4.5: (a) Cross-section schematic of the Ge waveguide APD with the Ge layer dimensions. (b) TEM longitudinal cross-section image.

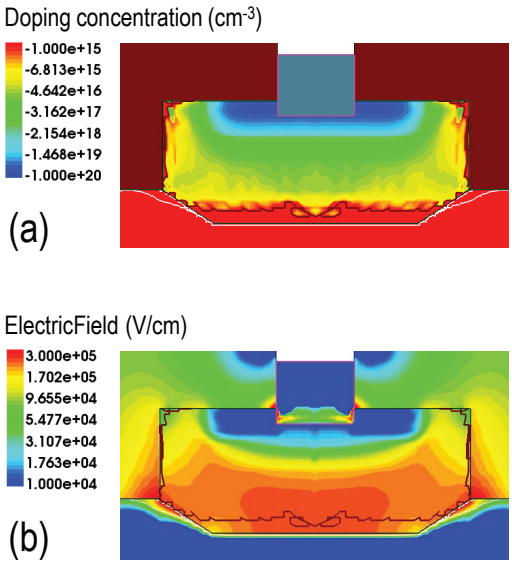

Figure 4.6: (a) Doping distribution in the Ge layer generated from Monte-Carlo ion implantation simulation. (b) Simulated electric field distribution in the Ge layer at 5.5V applied bias voltage.

4.2.2 Standalone APD characteristics

4.2.2.1 Static measurements

A typical static current-voltage characteristic of a 14 μm-long VPIN Ge APD device is shown in Fig. 7(a). The device has a low dark current of 17 nA at -1 V. As the bias voltage is increased to -4 V, the dark current starts to increase rapidly. The breakdown voltage is -6.2 V, and no burn-in effect was observed in the device. The light current is measured at 1550nm wavelength with an input optical power of -19.6 dBm received by the germanium photodiode (using a diffractive grating coupler with -5 dB coupling efficiency as fiber-chip interface). The responsivity is constant from 0 V to -3 V, owing to the relatively large built-in electrical field that is capable of sweeping out the majority of the photo-generated carriers even at 0 V bias. The measured primary responsivity is 0.6 A/W. The light current is 7 μA at -1 V. It starts to rise from -4 V, and it reaches 260 μA at -6.2 V. The avalanche gain extracted from these static measurements, defined as the multiplication factor of the net-light current (light current - dark current) is shown in Fig. 7(b). The gain increases sharply as the bias voltage becomes larger than -5 V, reaching its maximum value at -6.2 V. Beyond this breakdown voltage, the gain

decreases instead. This is because the great amount of photo-carriers generated from the avalanche multiplication partly screen the electric field in the device, and therefore the avalanche multiplication process gets weaker. It can be seen that at 90%, 95% and 98% of the breakdown voltage, the avalanche gain is 3.5, 6.3 and 10.0 respectively. The avalanche gain is independent of input optical power in the range from -30 dBm to -15 dBm.

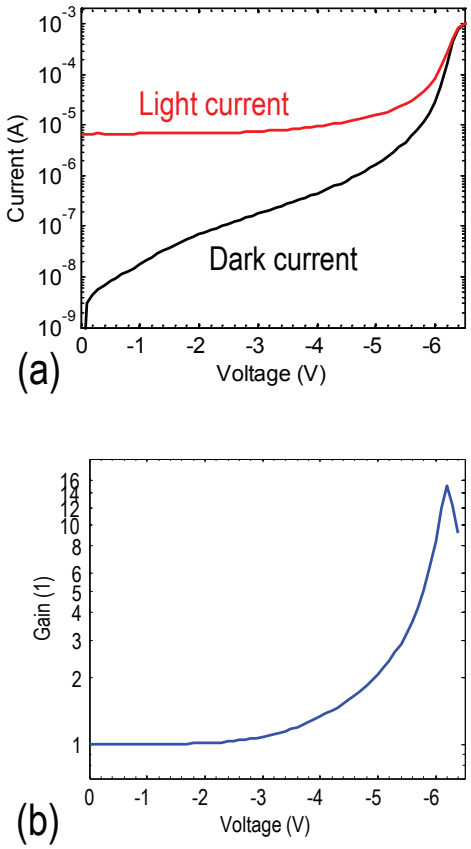

Figure 4.7: (a) Current-voltage characteristics of a 14 μm-long Ge APD (in the dark and under an input optical power of -19.6 dBm). (b) Avalanche gain extracted from the static measurements.

4.2.2.2 Small-signal measurements

Next, small-signal radio-frequency (RF) measurements at 1550 nm wavelength are carried out. Using an average input optical power of -15.8 dBm, the RF power delivered by the photodetector to a vector network analyzer (the S_{21} parameter) is recorded as a function of frequency for various applied bias voltages, as shown in Fig. 8. It can be seen that the low-frequency RF power increases with bias voltage until -6.2 V. Beyond this voltage, the low-frequency RF power drops instead, in accordance with the static measurements. Also, it can be seen that the 3 dB opto-electrical bandwidth drops substantially with increasing bias voltage.

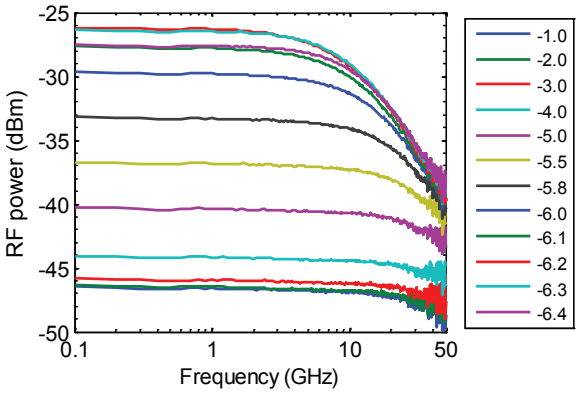

Figure 4.8: Small-signal RF measurement of S_{21} parameter for various bias voltages. As the reverse bias is increased beyond -2V, a substantial increase in the S_{21} parameter can be observed up to an optimum bias of -6.3 V, after which the S_{21} parameter (and hence the gain) starts to drop instead.

Avalanche gain extracted from small-signal measurements, defined as the square root of the multiplication factor of the low-frequency RF power (using the low frequency RF power at -1V as a reference), is shown in Fig. 9(a). Similar to what was obtained from the static measurements, the avalanche gain extracted from small-signal measurements reaches its maximum value at -6.2 V. Besides, it is independent of input optical power in the range from -30 dBm to -15 dBm. The 3dB opto-electrical bandwidth versus avalanche gain is shown in Fig. 9(b). At low bias voltages, the 3dB bandwidth is as high as 50 GHz (limited by the measurement setup). It decreases slowly as long as the multiplication gain is smaller than 2. As the gain further increases, the 3 dB bandwidth drops almost inversely proportional to the avalanche gain owing to the avalanche build-up time [18, 19]. At -6.2 V APD bias, a 3 dB bandwidth of 10.4 GHz at the avalanche gain of 10.2 is obtained. The gain$\times$bandwidth product (GBP) is shown in Fig. 9(c). It can be seen that the GBP

reaches a plateau at -5.8 V ($\sim$100 GHz), after which it further increases due to bandwidth enhancement as seen in Fig. 9(b), similar to what is reported in [5]. The 100 GHz GBP is comparable to standard InP-based APDs [20].

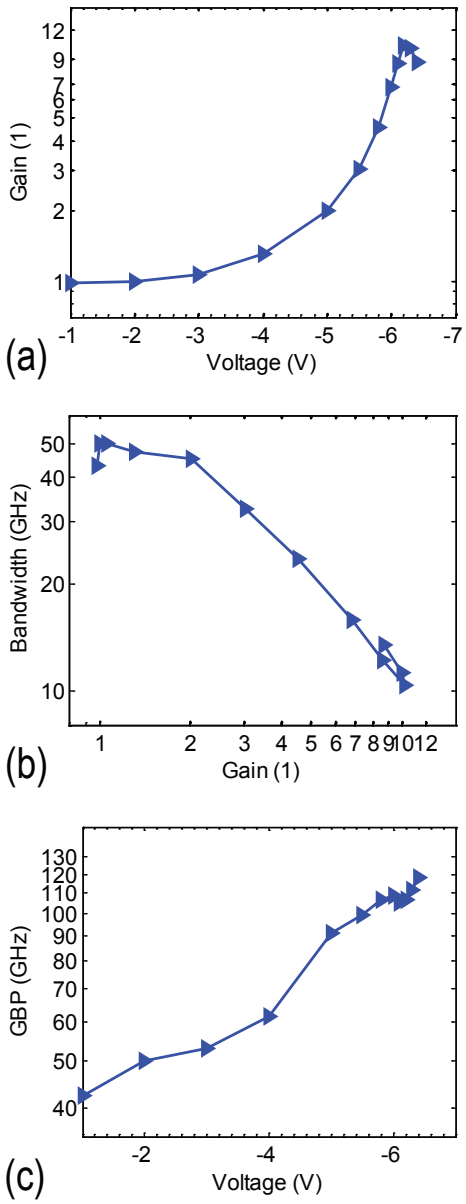

Figure 4.9: (a) Avalanche gain extracted from small-signal RF measurements as a function of bias voltage. (b) Measured 3dB opto-electrical bandwidth versus avalanche gain extracted from the S21 RF curves. (c) gain×bandwidth product as a function of bias voltage.

4.2.2.3 Avalanche excess noise characteristics

Next, excess multiplication noise measurements are performed to characterize the avalanche noise performance of the Ge APDs. The Ge APD was biased using a stable voltage source, and an optical continuous-wave laser source at 1550 nm was used as the input light. The a.c. component of the Ge APD output (which is the noise of the photodiode in this case) was measured at 150 MHz using a low-noise signal analyzer. The noise in the dark current of the Ge APD was also measured in the same way turning off the laser. The power spectral density (*PSD*) of the noise current under consideration (the net-light current power spectral density) is given by Eq. 1 in the avalanche multiplication regime,

$$PSD = 2q \cdot I \cdot M^2 \cdot F(M) \tag{4.1}$$

where *I* is net-light current (= light current - dark current) and *M* is net-light current gain (the avalanche gain extracted from static measurements). q is the elementary charge. The excess noise factor *F(M)* deduced from Eq. 1 as a function of gain is shown in Fig. 10(a) and Fig. 10(b) at 1550 nm wavelength for an input optical power of -23.8 dBm and -18.8 dBm, respectively. The excess noise factor can be expressed for the case of avalanche multiplication in a uniform electric field when electrons initiate the multiplication as in Eq. 2,

$$F(M) = k_{eff} \cdot M + (2 - 1/M) \cdot (1 - k_{eff}) \tag{4.2}$$

where k_{eff} is the effective ratio of ionization coefficients for electrons and holes. These ionization coefficients are almost equal in bulk Ge giving a k_{eff} of about 0.9, which results in a very large excess noise, making conventional Ge APDs uncompetitive for building digital optical links. Fitting the data with Eq. 2 reveals a k_{eff} of 0.5 in the presented device. The total reduction of the power spectral density of the noise current in the presented device compared to a bulk Ge APD can be estimated as 35% for an avalanche gain of 10. This is attributed to the dead space effect (the fact that the multiplication region thickness becomes comparable to the distance over which carriers do not experience impact ionization) in the 200nm thin avalanche multiplication region [8, 15–17].

The measured keff of 0.5 in this paper is larger than that of $\sim$ 0.2 reported in [8]. This can be explained by the fact that the region of impact ionization in germanium is just 30 nm for the MSM structure in [8], while it is $\sim$ 200 nm in the PIN structure demonstrated in this work. A thinner avalanche region results in more noise reduction effects and thus a smaller k_{eff} as discussed in section 1.4.3.2 (”Non-local Field Avalanche Theory”) in Chapter 1.

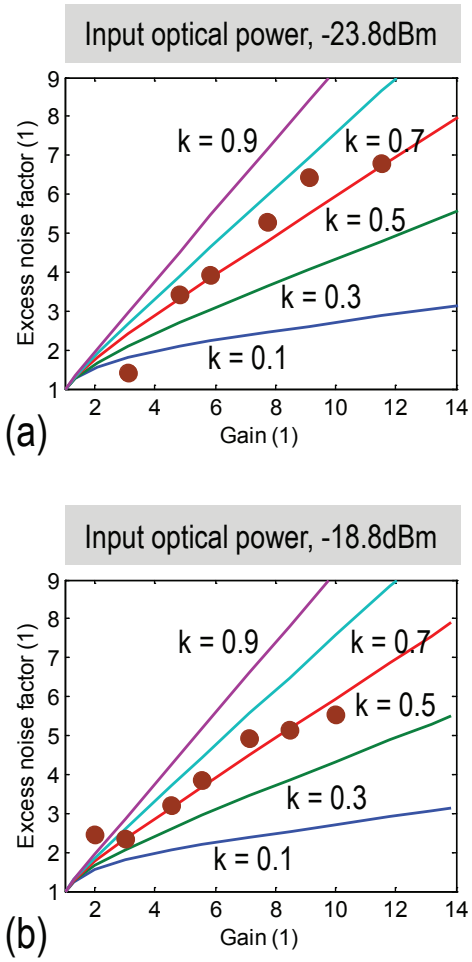

Figure 4.10: The excess noise factor as a function of gain with an input optical power of (a) -23.8 dBm and (b) -18.8 dBm.

4.2.3 APD receiver characteristics

Finally, in order to assess the sensitivity improvement by operating the APD in avalanche mode, the device was wire-bonded to a 10 Gbps trans-impedance amplifier (TIA) designed by INTEC_design, as shown in Fig. 11. The TIA is implemented in 0.13 μm SiGe BiCMOS technology and has a differential output [21, 22]. It is designed for burst-mode operation in access networks with an input referred RMS noise current lower than 1.2 μA. A $(2^{31}-1)$ long optical non-return-

to-zero pseudo-random bit sequence (PRBS) data pattern at 10 Gbps, generated by a commercial optical modulator with 8.9 dB extinction ratio, was launched into the wire-bonded APD receiver. The eye diagram of the optical signal generated by the modulator is shown in the inset of Fig. 12. A commercial limiting amplifier (LA) is connected to the TIA, and the LA differential outputs (both the DATA and XDATA port) were fed to a 10 Gbps error detector for bit error rate (BER) measurement. The measured differential BER as a function of input optical power for various bias voltages are shown in Fig. 12. For a BER of 1×10^{-12} (1×10^{-9}), the waveguide-referred primary sensitivity is -17.6 dBm (-18.6 dBm) average optical power at -1.7 V bias voltage, mostly limited by the TIA input-referred noise (RMS) current. The sensitivity increases with increasing bias. At -5.9 V APD bias voltage, a 5.8 dB sensitivity improvement is obtained, which yields an absolute receiver sensitivity of -23.4 dBm and -24.4 dBm for a 1×10^{-12} and 1×10^{-9} BER respectively. The avalanche gain, extracted from the small-signal measurements, is about 6 at -5.9 V bias voltage. Beyond -5.9 V, while the gain still rises as the bias voltage increases until -6.2 V, the sensitivity saturates due to the excess multiplication noise. 10 Gbps eye diagrams of the electrical signals from the LA with differential BER of $\sim 1 \times 10^{-9}$ at -5.9 V bias voltages for both the DATA and XDATA port were recorded by a high-speed oscilloscope, as shown in Fig. 13(a) and Fig. 13(b) respectively.

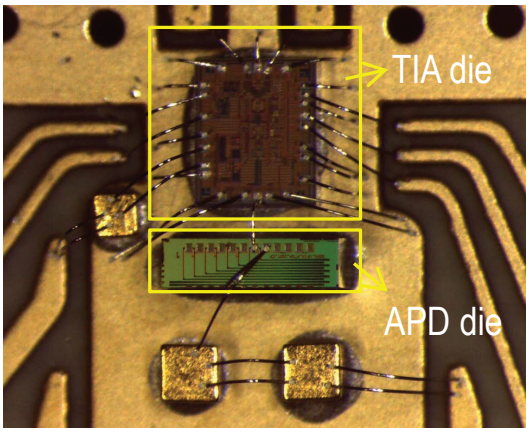

Figure 4.11: Constructed optical receiver with Ge APD wire-bonded to a TIA.

The sensitivity improvement of 5.8 dB is lower than that reported in [23], where the Q factor is used to characterize sensitivity and a 7 dB improvement is obtained for a Q factor of 7. This is because the low-noise TIA used in this work has a much smaller input referred RMS noise current than that of the TIA (implemented in 40 nm LP CMOS technology) wire-bonded in [23].

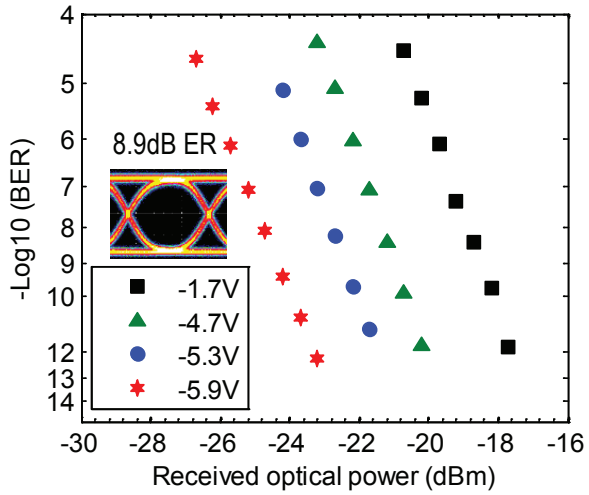

Figure 4.12: Measured bit error rate as a function of input optical power for various bias voltages.

Despite the sensitivity improvement of 5.8 dB, both the primary responsivity of 0.6 A/W (limited mostly due to the light absorption in the via contacts to the germanium) and the k_{eff} value of 0.5 need to be improved to further increase the absolute sensitivity of the wire-bonded optical receiver, which is -23.4 dBm for a 1×10^{-12} BER at 1550 nm wavelength in this paper. Compared with a Ge PIN photodetector with state-of-art responsivity of 1.1 A/W [24], assuming a TIA with the same noise performance as that of the TIA used in this paper, the wire-bonded APD-based optical receiver provides 3 dB sensitivity margin over that of the PIN photodetector based optical receiver. Furthermore, a SACM waveguide APD based optical receiver has been demonstrated with -30.4 dBm sensitivity for a 1×10^{-12} BER at 1304 nm [4] by leveraging the superior avalanche performance of silicon with a k_{eff} of $\sim$0.1. The operation voltage of the SACM waveguide APD is, however, as high as -25 V. Increasing primary responsivity and reducing keff so as to boost the absolute sensitivity of the Ge APD based optical receiver are therefore of key importance for further sensitivity enhancement.

4.2.4 Discussion and outlook

In order to increase the sensitivity of the VPIN Ge APD and further reduce the operation voltage, both the primary sensitivity and the avalanche sensitivity improvement need to be increased at a lower operation voltage. The avalanche sensitivity improvement can be increased by reducing the k-value. A straightforward

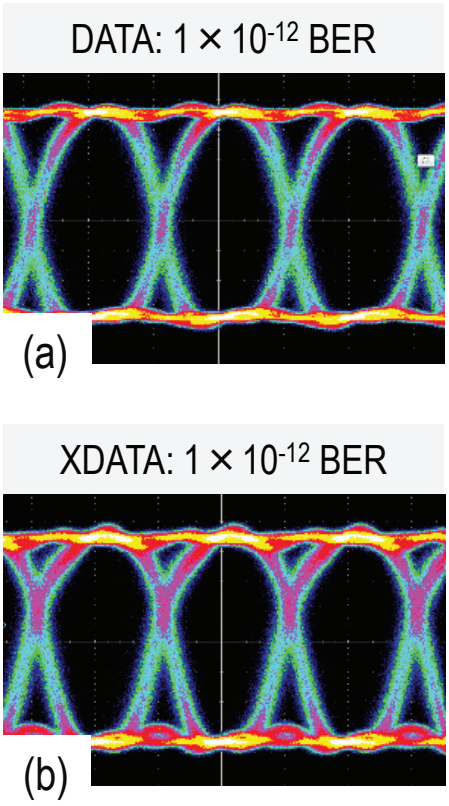

Figure 4.13: (a) 10Gb/s eye diagram of the electrical signal from LA DATA port with differential BER of 1×10^{-12} *at -5.9 V bias voltage (input optical power is -23.4 dBm). (b) 10Gb/s eye diagram of the electrical signal from LA XDATA port with differential BER of* 1×10^{-12} *at -5.9 V bias voltage (input optical power is -23.4dBm).*

way to reduce the k-value is adopting a thinner Ge layer. A thinner Ge VPIN APD has an even stronger electric field confinement at the bottom of the Ge layer. This confines the carriers ionizing in an even thinner region, which will increase the deterministic nature of the avalanche process and thus improve the avalanche noise performance of the Ge APD as discussed in chapter 1. Therefore, a lower k-value can be expected. This lower k-value will increase the 3-dB opto-electrical bandwidth of the Ge APD as it is limited by the build-up time. Finally, due to the stronger electric field confinement, a lower operation voltage can also be expected because a higher electric field strength can be obtained for the same bias voltage using a thinner Ge layer.

4.3 185 nm-Ge VPIN Ge APD

In order to further improve the sensitivity and reduce the operation voltage, a thinner Ge layer of 185 nm was adopted. It shows a 3-dB O/E bandwidth of 15.2 GHz at at a avalanche gain of 9.2 at -5 V bias. The gain$\times$bandwidth product is 140 GHz. A low effective k-value (the ratio of holes impact ionization rate to electrons impact ionization rate) of 0.2 is demonstrated from multiplication noise measurements. A 10 Gbps 1310 nm optical receiver based on such a Ge APD shows a 7 dB avalanche sensitivity improvement at -4.85 V APD bias. The absolute sensitivity is -21.7 dBm for a bit error rate of 1×10^{-9}. A 20 Gbps 1310 nm optical receiver based on such a Ge APD shows a 6.2 dB avalanche sensitivity improvement at -5.0 V APD bias. The absolute sensitivity is -17.4 dBm for a bit error rate of 1×10^{-9}. Operation of the receiver up to 25 Gbps is demonstrated.

4.3.1 Device Design and Fabrication

The Ge waveguide APDs were fabricated in imec's fully integrated Si Photonics platform going through a process flow described in [13]. Light is coupled from a 220 nm thick single-mode Si waveguide to the Ge layer using a fully etched waveguide taper, as shown in Fig. 14. The Ge layer dimensions and doping configuration are shown in Fig. 15(a). A vertical p-i-n structure (VPIN) is formed by implanting Si with phosphorous ions (before Ge growth) and by implanting the planarized Ge layer with boron ions. The boron ion implant window is uniform in the longitudinal direction. Fig. 15(b) shows a SEM image of the Ge APD cross section.

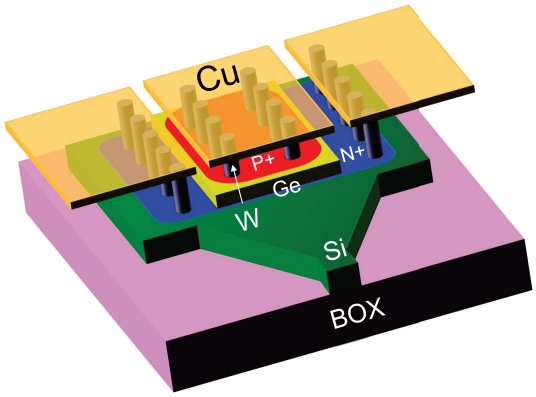

Figure 4.14: 3-D schematic of the Ge waveguide APD consisting of the Ge layer and Si waveguide taper.

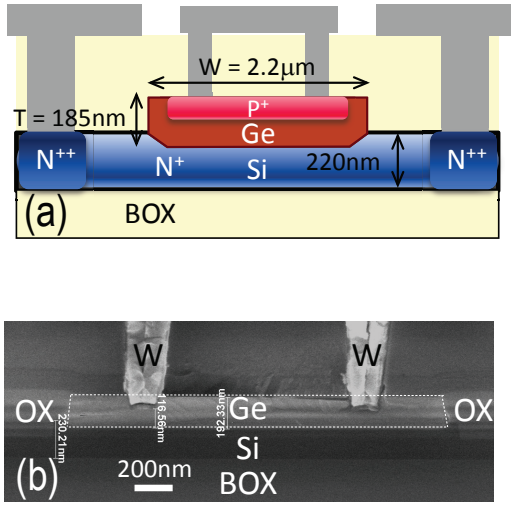

Figure 4.15: (a) Cross sectional schematic of the Ge waveguide APD with Ge layer dimensions. (b) SEM cross-section image of the Ge waveguide APD.

A 185 nm thin Ge layer was adopted to lower the operation voltage of the Ge APD. The simulated doping distribution in the Ge layer is shown in Fig. 16(a), generated from Monte-Carlo ion implantation simulations calibrated to SIMS data. The doping profile along A-A' (in Fig. 16(a)) is shown in Fig. 17(a). The heterogeneous Ge/Si VPIN configuration together with the 185 nm thin Ge layer results in a strongly non-uniform electric field at -3 V bias voltage, mostly confined in the lower 100 nm of the Ge layer, as shown in Fig. 16(b). Fig. 17(b) shows the electric field profile along A-A'(in Fig. 16. (b)) for a Ge layer of 185 nm, 285 nm and 385 nm thick, respectively, at -3 V bias voltage (assuming the same implant conditions). It can be seen that the thinner the Ge layer, the stronger the electric field is in the Ge layer. For the case of a 185 nm-thick Ge layer, the electric field strength is calculated to be as high as 5.2×10^5 V/cm at the Ge/Si interface at a bias of -3 V. The non-uniform electric field drops sharply to 1.4×10^5 V/cm about 100 nm away from the interface inside the Ge layer. Therefore, it is expected that strong avalanche multiplication can take place at low bias voltage and that the avalanche excess-noise generation can be suppressed to a great extent due to the limited thickness of the avalanche multiplication region [14–17].

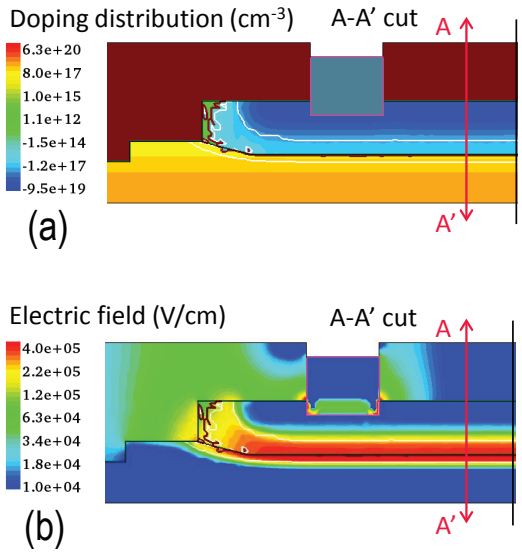

Figure 4.16: (a) Simulated doping distribution in the Ge APD. The boron ion implantation in the Ge layer was simulated using Monte-Carlo method calibrated to SIMS data. Only half of the structure is shown for clarity. (b) Simulated electric field distribution in the Ge layer at -3 V bias voltage.

4.3.2 Standalone APD Characteristics

4.3.2.1 Static Measurements

Static current-voltage characteristics of a 10 μm long VPIN Ge APD device are shown in Fig. 18(a). The device has a low dark current of 10 nA at -1 V. The light current was measured at 1310 nm wavelength under an waveguide referred input optical power of -19.8 dBm, -14.8 dBm, -9.8 dBm and -4.8 dBm, respectively. A compliance current of 0.5 mA was applied in the measurements. The measured primary responsivity is 0.3 A/W at -1 V. The light current increases rapidly as the bias voltage surpasses -3 V, owing to the adopted thin Ge layer design. The avalanche gain extracted from static measurements is consistent for the various input optical powers, as shown in Fig. 18(b).

As the Ge thickness is merely 185 nm, a small variation in this thickness over the wafer could have an impact on the device performance. Therefore wafer scale measurements of the static device performance were carried out. Wafer scale primary responsivity data (in the bottom half of the wafer) of the Ge APD at -1 V under an input optical power of -19.8 dBm are shown in Fig. 19(a). The mean primary responsivity value is 0.3 A/W with a standard deviation of 0.06 A/W. Fig.

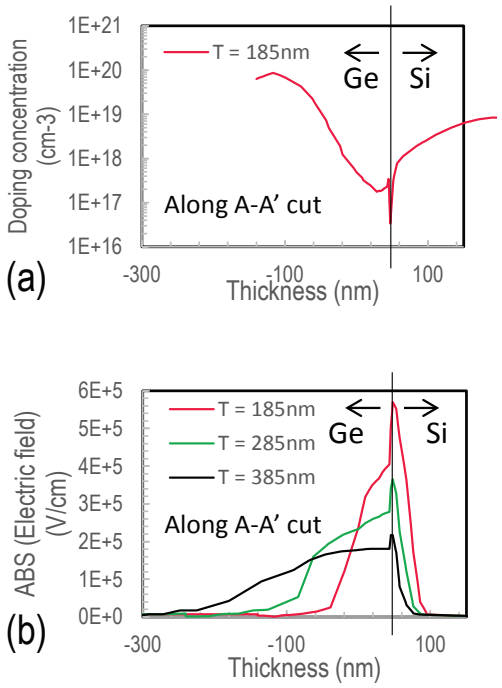

Figure 4.17: (a) Doping profile extracted along the A-A cut (in Fig. 3(a)). (b) Electric field profiles extracted along the A-A cut (in Fig. 3(b)) for a Ge layer of 185 nm, 285 nm, and 385 nm thick, respectively.

19(b) shows wafer scale avalanche gain data extracted from static measurements at -5 V under an input optical power of -19.8 dBm. The mean avalanche gain value is 10.6 with a standard deviation of 2.4. Both the primary responsivity data and avalanche gain data indicate a uniform wafer-scale APD static performance.

4.3.2.2 Small-signal RF Measurements

Next, small-signal radio-frequency (RF) measurements were carried out at 1310 nm using an average optical input power of -14.2 dBm. As shown in Fig. 20, with increasing bias voltage, the generated low-frequency RF power increases substantially. Fig. 21(a) shows the wafer-scale avalanche gain data extracted from these small-signal measurements. It reaches a mean value of 9.2 at -5 V. The wafer-scale gain·bandwidth product (GBP) data is shown in Fig. 21(b). The mean value is 140 GHz at -5 V. Fig. 21(c) shows the mean value of the 3-dB bandwidth data (at a given reverse bias) as a function of the mean value of avalanche gain data (at that same reverse bias). The increase of the 3-dB bandwidth as long as the

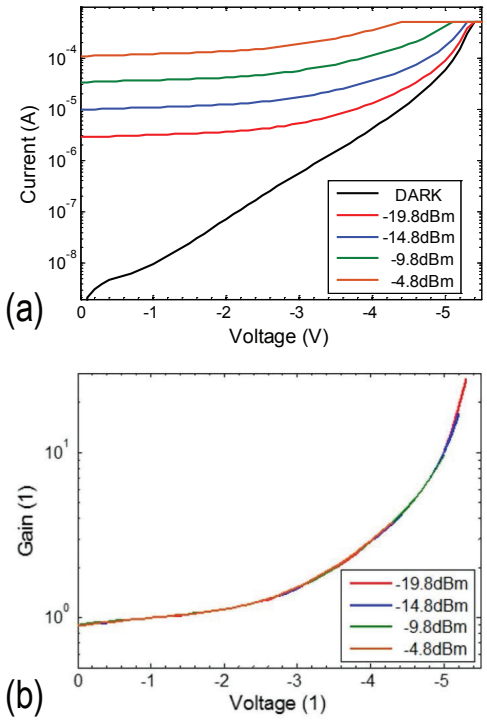

Figure 4.18: (a) Current-voltage characteristics of a 14 μm long Ge APD device (in the dark and for an input optical power of -19.8dBm, -14.8 dBm, -9.8 dBm, and -4.8 dBm, respectively). (b) Avalanche gain extracted from static measurements under the various input optical powers.

avalanche gain is lower than 2 is due to the widening of the depletion region in the Ge layer. As the gain gets larger than 4, the 3-dB bandwidth drops quickly, due to the avalanche build-up time.

A contour plot of wafer-scale avalanche gain data of the Ge APD at -5 V bias is shown in Fig. 22(a). The mean avalanche gain value is 9.2 with a standard deviation of 1.6. The similar magnitude and pattern of the wafer-scale avalanche gain data extracted from static measurements and small-signal measurements confirm the validity of the avalanche gain definition in both types of measurements. Fig. 22(b) shows the contour plot of wafer scale GBP data at -5 V bias. The mean value is 140 with a standard deviation of 27. The relatively large variation in the avalanche gain and GBP at wafer scale is mainly due to the Ge layer thickness variation at wafer scale introduced from the CMP after Ge epitaxy. This will not be a problem as an APD will always operate together with a control circuit.

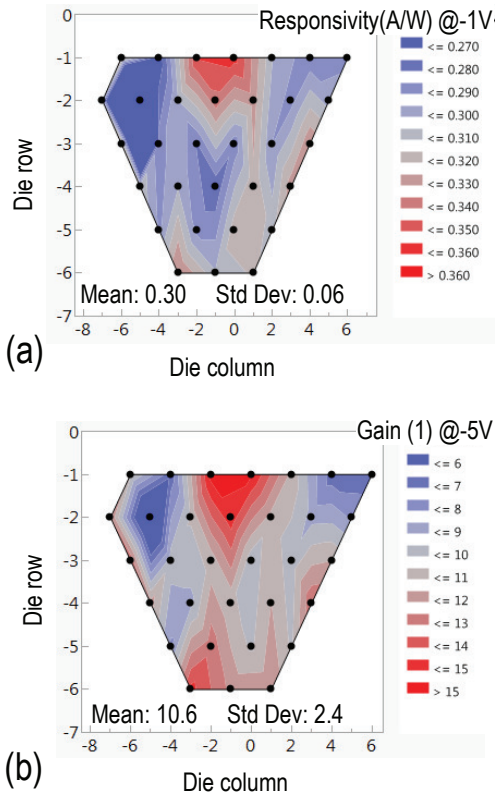

Figure 4.19: (a) Wafer-scale primary responsivity data (at -1 V) under an input optical power of -19.8 dBm. (b) Wafer-scale avalanche gain data extracted from static measurements at -5 V under an input optical power of -19.8 dBm.

4.3.2.3 Avalanche Excess Noise Characteristics

Next, multiplication noise measurements were performed to characterize the avalanche multiplication noise. The noise current power spectral density (PSD) at 250 MHz in both dark current and light current (at 1310 nm wavelength) was measured using a low-noise signal analyzer. The excess noise factor *F(M)* as a function of gain is shown in Fig. 23 for an input optical power of -22.4 dBm. The excess noise factor can be expressed for the case of avalanche multiplication in a uniform electric field with electrons initiating the multiplication as in Eq. 1,

$$F(M) = k_{eff} \cdot M + (2 - 1/M) \cdot (1 - k_{eff}) \tag{4.3}$$

where k_{eff} is the effective ratio of ionization coefficients for holes and electrons. Fitting the data with Eq. 1 reveals a k_{eff} of 0.2 in the presented device. Such a low

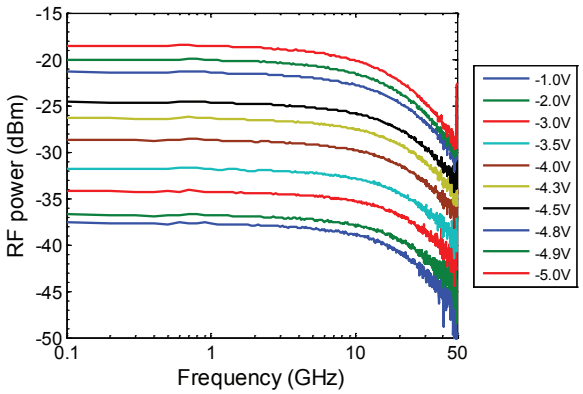

Figure 4.20: Small-signal RF measurements of the transmission parameter (S_{21}) for various bias voltages under an input optical power of -14.2 dBm. The S_{21} parameter rises significantly with increasing bias voltage.

value (the k-value is close to 1 in bulk germanium) is a signature of multiplication noise suppression owing to the thin avalanche multiplication region [14–17].

4.3.3 APD Receiver Characteristics

4.3.3.1 10 Gbps APD receiver sensitivity measurements

A 10 Gbps optical receiver was constructed by wire-bonding an APD device to a 10 Gbps trans-impedance amplifier (TIA) to assess the receiver sensitivity. The 10 Gbps TIA [21, 22] used is the same as that adopted for the 400 nm Ge VPIN APD [1], and has an input referred root-mean-square (RMS) noise current lower than 1.2 μA. A (2^{31}-1) long non-return-to-zero (NRZ) pseudo-random bit sequence (PRBS) data pattern at 10 Gbps, generated by a commercial optical modulator with 9.6 dB extinction ratio at 1310 nm wavelength (as shown in the inset of Fig. 24), was launched into the wire-bonded APD receiver. The measured bit error rate (BER) as a function of input optical power for various bias voltages is shown in Fig. 24. For a BER of 1×10^{-9}, the waveguide-referred primary sensitivity is -14.7 dBm average optical power at -1.1 V bias voltage. A 7 dB sensitivity improvement is obtained at -4.85 V bias voltage, yielding an absolute receiver sensitivity of -21.7 dBm for a 1×10^{-9} BER. The avalanche gain, extracted from small-signal measurements, is larger than 7 at -4.85 V bias. The higher sensitivity improvement of 7 dB at a larger gain of > 7 compared to that reported for the 400 nm Ge VPIN APD [1] results from the lower effective k-value of 0.2 than that of 0.5 reported for the 400 nm Ge VPIN APD [1] by adopting an 185 nm thin Ge layer. 10 Gbps eye diagrams of the electrical signals from the TIA at a BER

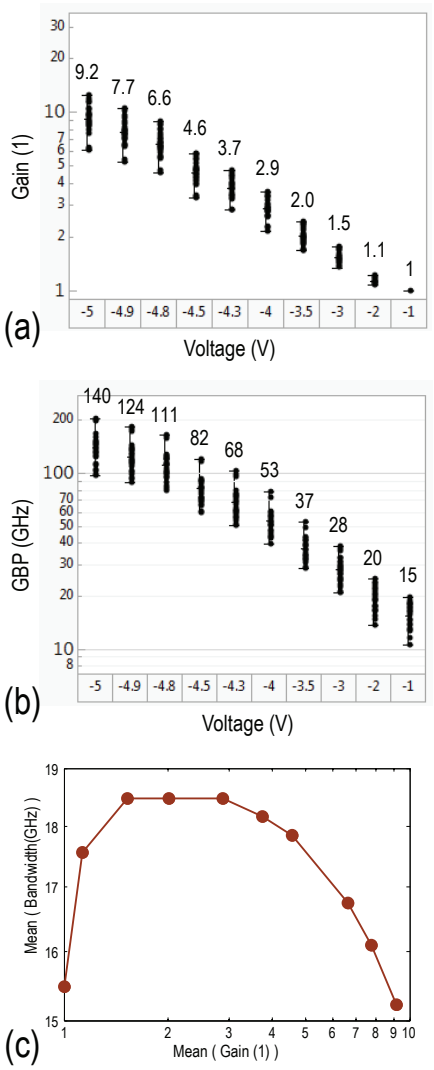

Figure 4.21: (a) Wafer-scale avalanche gain data extracted from the small-signal RF measurements for various bias voltages. (b) Wafer-scale gain bandwidth product data. (c) The mean value of the measured 3-dB opto-electrical bandwidth data (at a given reverse bias) as a function of the mean value of avalanche gain data (at the same reverse bias) extracted from small-signal measurements.

of 3×10^{-12} at both -1.1 V and -4.85 V bias voltages from both the DATA and XDATA port were recorded by a high-speed oscilloscope, as shown in Fig. 25.

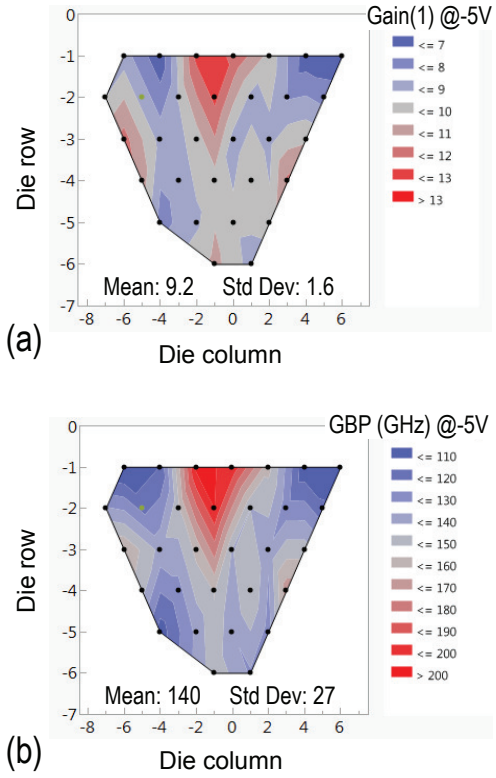

Figure 4.22: (a) Contour plot of the wafer-scale avalanche gain data at -5 V bias. (b) Contour plot of the wafer-scale gain×bandwidth product data at -5 V bias.

4.3.3.2 20/25 Gbps APD receiver sensitivity measurements

Given the higher gain×bandwidth product, a higher data-rate optical receiver is also built by wire-bonding another 185 nm Ge VPIN APD to a 40 Gbps TIA designed by INTEC_design. The 0.13 μm SiGe BiCMOS TIA has an input referred (RMS) noise current of 2 μA for 20 Gbps settings [25]. Fig. 26 shows the measured BER at 20 Gbps as a function of input optical power at 1310 nm wavelength. The waveguide-referred primary sensitivity is -11.2 dBm average optical power at -1.1 V bias voltage for a BER of 1×10^{-9}. A 6.2 dB sensitivity improvement is obtained at -5.0 V bias voltage, yielding an absolute receiver sensitivity of -17.4 dBm for a 1×10^{-9} BER. The avalanche gain, extracted from small-signal measurements, is 9 at -5.0 V bias. The inset of Fig. 26 shows an eye diagram of the 20 Gbps optical NRZ PRBS data pattern ($(2^{31} - 1)$ long) with 8.3 dB extinction ratio at 1310 nm wavelength used for the BER measurements. The 20 Gbps eye

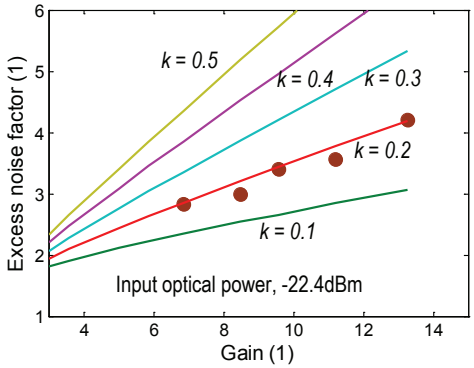

Figure 4.23: The excess noise factor as a function of avalanche gain for an input optical power of -22.4 dBm for a 185 nm thick Ge VPIN APD.

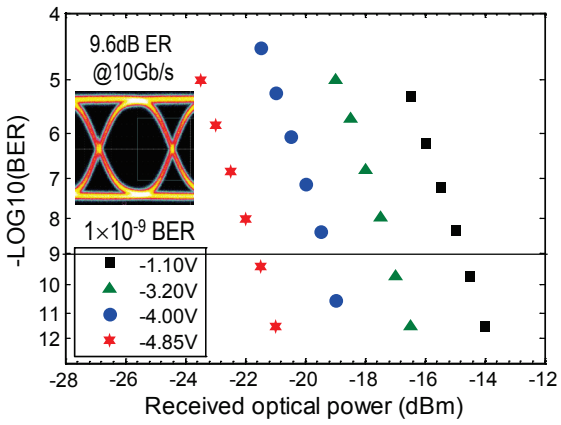

Figure 4.24: Measured BER at 10 Gbps as a function of input optical power for various bias voltages using a $(2^{31} - 1)$ long optical NRZ PRBS pattern at 1310 nm. The inset is the 10 Gbps input eye generated by a commercial optical modulator with an extinction ratio of 9.6 dB.

diagrams of the electrical signal from the TIA with a BER of 2×10^{-9} at both -1.1 V and -5.0 V bias voltage is shown in Fig. 27(a) and Fig. 27(b), respectively.

Operation at 25 Gbps was also evaluated. The obtained BER at -5 V APD bias at 25 Gbps for the wire-bonded optical receiver is shown in Fig.28. The absolute sensitivity is -14.8 dBm for a 1×10^{-9} BER. A 25 Gbps eye diagram of the electrical signal from the TIA with a BER of 2×10^{-9} at -5.0 V APD bias is

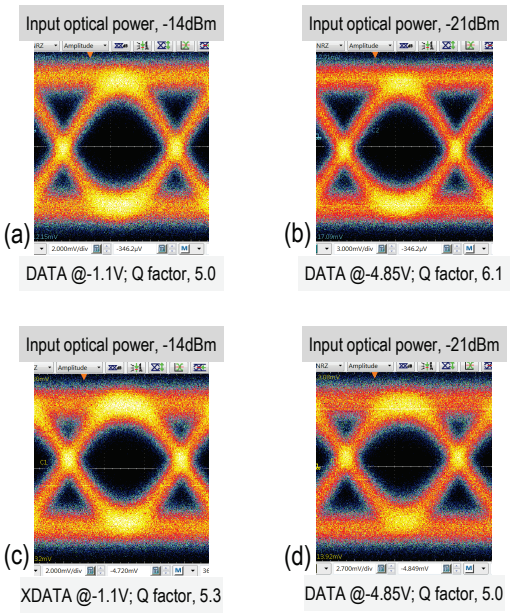

Figure 4.25: 10 Gbps eye diagrams of the electrical signal with a BER of 3×10^{-12} *from (a) TIA DATA port at -1.1 V APD bias, (b) TIA DATA port at -4.85 V APD bias, (c) TIA XDATA port at -1.1 V APD bias, and (d) TIA XDATA port at -4.85 V APD bias, respectively.*

shown in the inset of Fig. 28, where eye degradation owing to the APD bandwidth limitation starts to be observed. The 2.6 dB power penalty for a 1×10^{-9} BER at 25 Gbps compared to that at 20 Gbps can be largely attributed to this bandwidth limitation (15.2 GHz) of the APD at -5.0 V bias voltage.

4.3.4 Discussion and outlook

The presented 185 nm VPIN Ge APD shows a better avalanche performance than that of the 400 nm VPIN Ge APD. The k-value is reduced to 0.2 from 0.5, and as for an avalanche gain of 10, the 3-dB bandwidth is increased to 18 GHz from 10 GHz at a lower operation voltage of -5 V. However, the low primary responsivity of 0.3 A/W is the limiting factor for further improving the sensitivity of the APD based optical receiver. There are 4 potential factors responsible for the low primary responsivity: light absorption from the tungsten via contacts, free-carrier absorption, (valence) band-filling induced Ge absorption reduction and a low photo-carrier collection efficiency. Optimizing the taper design to confine the incoming lightwave from the Si waveguide to the middle of the Ge layer is an ef-

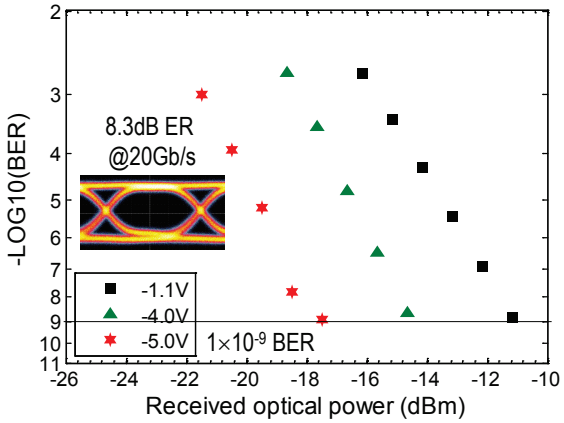

Figure 4.26: BER at 20 Gbps as a function of input optical power using a ($2^{31} - 1$) long NRZ PRBS pattern at 1310 nm. The inset shows the 20 Gbps optical input eye diagram with an extinction ratio of 8.3 dB.

fective way to minimize the light absorption from via contacts. Adopting a dotted ion implant window layout rather than a continuous implant window layout (as adopted in this paper) will effectively reduce both free-carrier absorption and Ge absorption reduction due to the Boron doping induced valence band filling. At the same time, it also increases the photo-carrier collection efficiency.

4.4 Conclusion

2 versions of VPIN Ge APDs were demonstrated. The 400 nm Ge VPIN APD receiver shows a 5.8 dB sensitivity improvement at -5.9 V bias at 10 Gbps, and the absolute sensitivity is -23.4 dBm for a bit error rate of 1×10^{-12}. The 185 nm Ge VPIN APD receiver shows a 6.2 dB sensitivity improvement at -5 V bias at 20 Gbps, and the absolute sensitivity is -17.4 dBm for a bit error rate of 1×10^{-9}.

The performance of both VPIN Ge APDs (absolute sensitivity versus operation voltage) are benchmarked as shown in Fig. 29. With a simple design, the VPIN Ge APDs show good sensitivities at a low operation voltage.

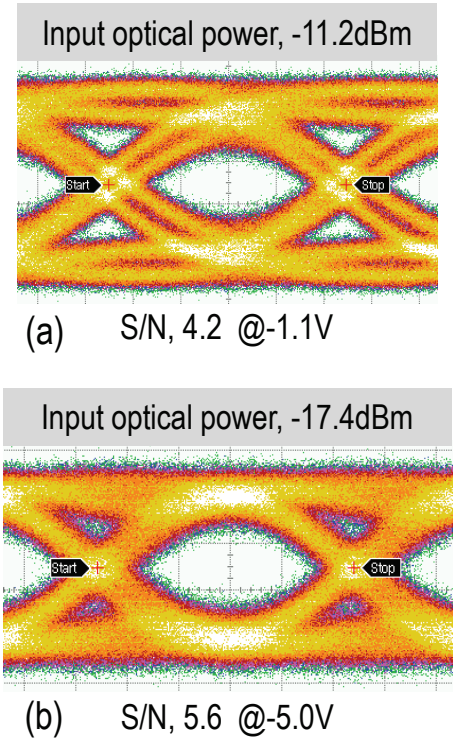

Figure 4.27: 20 Gbps eye diagrams of the electrical signal with a BER of 2×10^{-9} *from TIA at -1.1 V and (b) at -5.0 V APD bias, respectively.*

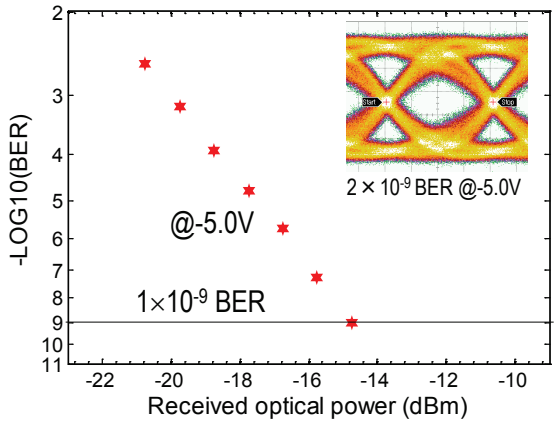

Figure 4.28: BER at 25 Gbps using a $(2^{31}-1)$ *long NRZ PRBS pattern at 1310 nm at -5.0 V APD bias. The inset shows the 25 Gbps eye diagram of the electrical signal with a BER of* 2×10^{-9} *from TIA at -5.0 V APD bias.*

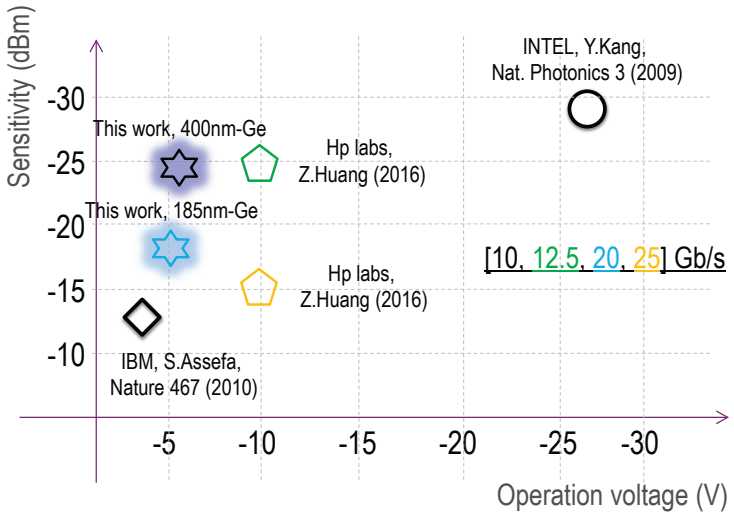

Figure 4.29: VPIN Ge APDs benchmarking, absolute sensitivity $(1 \times 10^{-12}$ *BER) versus operation voltage.*

References

[1] H T Chen, J Verbist, P Verheyen, P De Heyn, G Lepage, J De Coster, P Absil, X Yin, J Bauwelinck, J Van Campenhout, and G Roelkens. *High sensitivity 10Gb/s Si photonic receiver based on a low-voltage waveguide-coupled Ge avalanche photodetector*. Opt. Express, 23(2):815–822, jan 2015.

[2] H. T. Chen, J. Verbist, P. Verheyen, P. De Heyn, G. Lepage, J. De Coster, P. Absil, B. Moeneclaey, X. Yin, J. Bauwelinck, J. Van Campenhout, and G. Roelkens. *25-Gb/s 1310-nm optical receiver based on a sub-5-V waveguide-coupled germanium avalanche photodiode*. IEEE Photonics Journal, 7(4), 2015.

[3] Yimin Kang, Han-Din Liu, Mike Morse, Mario J Paniccia, Moshe Zadka, Stas Litski, Gadi Sarid, Alexandre Pauchard, Ying-Hao Kuo, Hui-Wen Chen, Wissem Sfar Zaoui, John E Bowers, Andreas Beling, Dion C McIntosh, Xiaoguang Zheng, and Joe C Campbell. *Monolithic germanium/silicon avalanche photodiodes with 340 GHz gain-bandwidth product*. Nat Photon, 3(1):59–63, jan 2009.

[4] Yimin Kang, Zhihong Huang, Yuval Saado, Joe Campbell, Alex Pauchard, John Bowers, and Mario Paniccia. *High Performance Ge/Si Avalanche Photodiodes Development in Intel*. In Optical Fiber Communication Conference/National Fiber Optic Engineers Conference 2011, page OWZ1. Optical Society of America, 2011.

[5] Wissem Sfar Zaoui, Hui-Wen Chen, John E Bowers, Yimin Kang, Mike Morse, Mario J Paniccia, Alexandre Pauchard, and Joe C Campbell. *Frequency response and bandwidth enhancement in Ge/Si avalanche photodiodes with over 840GHz gain-bandwidth-product*. Opt. Express, 17(15):12641–12649, jul 2009.

[6] M Huang, T Shi, P Cai, L Wang, S Li, W Chen, C y. Hong, and D Pan. *25Gb/s normal incident Ge/Si avalanche photodiode*. In 2014 The European Conference on Optical Communication (ECOC), pages 1–3, sep 2014.

[7] Mengyuan Huang, Pengfei Cai, Su Li, Liangbo Wang, Tzung-i Su, Liyuan Zhao, Wang Chen, Ching-yin Hong, and Dong Pan. *Breakthrough of 25Gb/s*

Germanium on Silicon Avalanche Photodiode. In Optical Fiber Communication Conference, page Tu2D.2. Optical Society of America, 2016.

[8] Solomon Assefa, Fengnian Xia, and Yurii a Vlasov. *Reinventing germanium avalanche photodetector for nanophotonic on-chip optical interconnects.* Nature, 464(7285):80–84, 2010.

[9] Léopold Virot, Paul Crozat, Jean-Marc Fédéli, Jean-Michel Hartmann, Delphine Marris-Morini, Eric Cassan, Frédéric Boeuf, and Laurent Vivien. *Germanium avalanche receiver for low power interconnects*. Nature Communications, 5:4957, 2014.

[10] J. R. Weber, A. Janotti, P. Rinke, and C. G. Van De Walle. *Dangling-bond defects and hydrogen passivation in germanium*. Applied Physics Letters, 91(14), 2007.

[11] M Pantouvaki, P Verheyen, G Lepage, J De Coster, H Yu, P De Heyn, P Absil, and J Van Campenhout. *20Gb/s silicon ring modulator co-integrated with a Ge monitor photodetector*. In Optical Communication (ECOC 2013), 39th European Conference and Exhibition on, pages 1–3, sep 2013.

[12] Peter De Heyn, Jeroen De Coster, Peter Verheyen, Guy Lepage, Marianna Pantouvaki, Philippe Absil, Wim Bogaerts, Joris Van Campenhout, and Dries Van Thourhout. *Fabrication-tolerant four-channel wavelength-division-multiplexing filter based on collectively tuned si microrings*. Journal of Lightwave Technology, 31(16):2785–2792, 2013.

[13] Peter Peter Verheyen, Marianna Pantouvaki, Joris Van Campenhout, Philippe P Absil, Hongtao Chen, Peter De Heyn, Guy Lepage, Jeroen De Coster, Pieter Dumon, Adil Masood, Dries Van Thourhout, Roel Baets, and Wim Bogaerts. *Highly Uniform 25 Gb/s Si Photonics Platform for High-Density, Low-Power WDM Optical Interconnects*. In Advanced Photonics for Communications, page IW3A.4. Optical Society of America, 2014.

[14] Joe C. Campbell. *Recent advances in telecommunications avalanche photodiodes*. In Journal of Lightwave Technology, volume 25, pages 109–121, 2007.

[15] M.M. Hayat, B.E.a. Saleh, and M.C. Teich. *Effect of dead space on gain and noise of\ndouble-carrier-multiplication avalanche photodiodes*. IEEE Transactions on Electron Devices, 39(3):546–552, 1992.

[16] Majeed M. Hayat, Oh Hyun Kwon, Shuling Wang, Joe C. Campbell, Bahaa E A Saleh, and Malvin C. Teich. *Boundary effects on multiplication noise in thin heterostructure avalanche photodiodes: Theory and experiment*. IEEE Transactions on Electron Devices, 49(12):2114–2123, 2002.

[17] S. C Liew Tat Mun, C. H. Tan, Y. L. Goh, A. R J Marshall, and J. P R David. *Modeling of avalanche multiplication and excess noise factor in In 0.52Al0.48As avalanche photodiodes using a simple Monte Carlo model*. Journal of Applied Physics, 104(1), 2008.

[18] R. B. Emmons. *Avalanche-photodiode frequency response*. Journal of Applied Physics, 38(9):3705–3714, 1967.

[19] Robert J. McIntyre. *The Distribution of Gains in Uniformly Multiplying Avalanche Photodiodes: Theory*. IEEE Transactions on Electron Devices, 19(6):703–713, 1972.

[20] D S Franco, K Vaccaro, W R Clark, W A Teynor, H M Dauplaise, M Roland, B Krejca, and J P Lorenzo. *High-performance InGaAs-InP APDs on GaAs*. IEEE Photonics Technology Letters, 17(4):873–874, apr 2005.

[21] Xin Yin, Xing-Zhi Qiu, Jan Gillis, Jasmien Put, Jochen Verbrugghe, Johan Bauwelinck, Jan Vandewege, Heinz Krimmel, Dora van Veen, Peter Vetter, and Others. *Experiments on a 10 Gb/s fast-settling high-sensitivity burst-mode receiver with on-chip auto-reset for 10G-GPONs [Invited]*. Journal of Optical Communications and Networking, 4(11):B68—-B76, 2012.

[22] X Yin, J Put, J Verbrugghe, J Gillis, X Z Qiu, J Bauwelinck, J Vandewege, H G Krimmel, and M Achouche. *A 10Gb/s burst-mode TIA with on-chip reset/lock CM signaling detection and limiting amplifier with a 75ns settling time*. In 2012 IEEE International Solid-State Circuits Conference, pages 416–418, feb 2012.

[23] H T Chen, P Verheyen, M Rakowski, P De Heyn, G Lepage, J De Coster, P Absil, G Roelkens, and J Van Campenhout. *Low-voltage Ge avalanche photodetector for highly sensitive 10Gb/s Si photonics receivers*. In 11th International Conference on Group IV Photonics (GFP), pages 106–107, aug 2014.

[24] Hong Tao Chen, Peter Verheyen, Peter De Heyn, Guy Lepage, Jeroen De Coster, Philippe Absil, Gunther Roelkens, and Joris Van Campenhout. *High-Responsivity Low-Voltage 28-Gb/s Ge p-i-n Photodetector With Silicon Contacts*. J. Lightwave Technol., 33(4):820–824, feb 2015.

[25] B Moeneclaey, J Verbrugghe, F Blache, M Goix, D Lanteri, B Duval, M Achouche, J Bauwelinck, and X Yin. *A 40-Gb/s Transimpedance Amplifier for Optical Links*. IEEE Photonics Technology Letters, 27(13):1375–1378, jul 2015.

5 Conclusion and Outlook

5.1 Conclusion

5.1.1 Germanium p-i-n photodetector

Germanium waveguide p-i-n photodetectors without metal contacts on Ge, grown on and contacted through a silicon p-i-n diode structure were developed. Such Si-contacted Ge p-i-n photodetectors adopting a 160 nm thick and 14 μm long Ge layer showed an opto-electrical 3-dB bandwidth of 67 GHz and 44 GHz at 1550 nm and 1310 nm, respectively, at -1 V bias. The junction capacitance was 6.8 fF at -1 V. The measured responsivity at -1 V was 0.74 A/W and 0.93 A/W at 1550 nm and 1310 nm respectively. The dark current was as low as 4 nA at -1 V. 56 Gbps on-off keying non-return-to zero data reception was demonstrated with clear open eye diagrams at both 1550 nm and 1310 nm wavelength. 80 Gbps and 100 Gbps on-off keying return-to zero data reception were demonstrated with clear open eye diagrams at 1550 nm wavelength.

The Ge layer thickness of a Si-contacted Ge p-i-n photodetector can be designed to optimize the opto-electrical bandwidth or responsivity performance. A 400 nm thick and 14 μm long device was demonstrated with a responsivity over 1 A/W in the whole C-band and a 3-dB opto-electrical bandwidth of 20 GHz at 1550 nm at -1 V bias. The opto-electrical bandwidth of the 160 nm $\times$ 14 μm device was limited by the transit time. The relatively low responsivity of 0.74 A/W at 1550 nm was limited by the short device length (Ge waveguide length), and the incident lightwave was not fully absorbed in the 14 μm long Ge waveguide. This indi-

cates that the responsivity can be improved by increasing the length of the device reasonably without compromising on the opto-electrical bandwidth.

5.1.2 Germanium avalanche photodetector

Low-voltage Germanium waveguide avalanche photodetectors based on a vertical p-i-n junction were developed. Such VPIN Ge APDs adopting a 185 nm thick and 2.2 μm wide Ge layer showed a low effective k-value of 0.2 and a gain$\times$bandwidth product value of 140 GHz at -5 V bias. A 1310 nm optical receiver constructed using such a Ge APD showed a 6.2 dB avalanche sensitivity improvement at -5.0 V APD bias at 20 Gbps, and operation of the receiver up to 25 Gbps was demonstrated. The absolute sensitivity was -17.4 dBm at a bit error ratio of 1×10^{-9}. This relatively low absolute sensitivity was limited by the low primary responsivity of 0.3 A/W.

Increasing the Ge layer thickness could improve the primary responsivity, however, the avalanche performance (avalanche gain, excess noise factor) will get compromised. A 400 nm thick Ge VPIN APD was demonstrated with a primary responsivity of 0.6 A/W at 1550 nm, and the effective k-value is $\sim$0.5 and a higher operation voltage of -6.2 V is required for the optical receiver to operate at the optimal state (with highest sensitivity).

5.2 Outlook

5.2.1 Germanium p-i-n photodetector

As the Ge layer thickness can be designed to optimize the responsivity and/or opto-electrical bandwidth performance, the optimal Ge layer thickness should be determined by the actual application (high responsivity and/or high bandwidth).

As for the 160 nm Si-contacted Ge p-i-n photodetector, the responsivity at a long wavelength of 1570 nm is only 0.5 A/W. This is limited by the low modal confinement factor at long wavelength in the 160 nm$\times$500 nm Ge layer. Adding a distributed Bragg reflector (DBR) following the Ge waveguide, as shown in Fig. 1, might help improving the responsivity since the transmitted light through the Ge waveguide will be reflected back and get absorbed again. In this case, a short device can be used and the opto-electrical bandwidth will not get compromised.

5.2.2 Germanium avalanche photodetector

There are four potential factors responsible for the low primary responsivity in the 185 nm VPIN Ge APD: light absorption from the tungsten via contacts, free-carrier absorption, (valence) band-filling induced Ge absorption reduction, and a low photocarrier collection efficiency. Optimizing the taper design to confine

Figure 5.1: Improving the responsivity at long wavelength using a DBR following the Ge waveguide.

the incoming lightwave from the Si waveguide to the middle of the Ge layer is an effective way to minimize the light absorption from via contacts. Adopting a dotted ion implant window layout rather than a continuous implant window layout (as adopted in this work) will effectively reduce both free-carrier absorption and Ge absorption reduction due to the Boron doping induced valence band filling. At the same time, it also increases the photo-carrier collection efficiency.

As there is a trade-off between the primary responsivity and avalanche performance regarding the Ge layer thickness, and adopting a dotted ion implant window might reduce the avalanche gain since the electric field confined to the bottom of Ge might get weak. New Ge APD designs need to be explored to eliminate this trade-off. An interesting design is to construct a lateral separated-absorption-charge-multiplication (L-SACM) Ge APD, as shown in Fig. 2, where Ge only serves for light absorption with both the charge 'layer' and multiplication 'layer' realized on the 220 nm Si. This could leverage both the strong absorption of Ge and the low avalanche excess noise of Si, and thus high sensitivity can be expected at a low operation voltage.

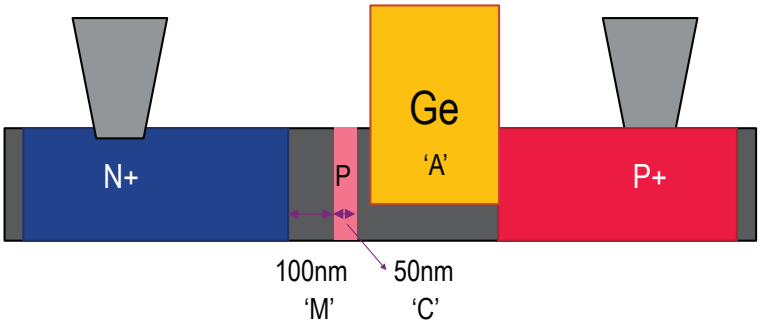

Figure 5.2: L-SACM Ge APD design with both the charge 'layer' and the multiplication 'layer' in the 220 nm Si. 'A': absorption; 'C': charge; 'M':multiplication.

Special attention should be paid to the reliability of such Ge avalanche photodetectors. Hot carrier mediated reliability problems are known to occur in avalanche photodetectors and are potentially stronger in germanium because of the misfit defects around the Ge/Si interface, the threading dislocations in the Ge layer, and the surface defects due to the poor passivation.

A Publications

A.1 Patent

1. H. Chen, J. Van Campenhout, G. Roelkens, "Integrated avalanche germanium photodetector," U.S. Patent EP 3038167 A1.

A.2 International journals

1. H. Chen, P. Verheyen, P. De Heyn, G. Lepage, J. De Coster, P. Absil, G. Roelkens, J. Van Campenhout, High responsivity low-voltage 28Gb/s Ge p-i-n photodetector with silicon contacts, Journal of Lightwave Technology 33(4), 820-824 (2015).

2. H. Chen, P. Verheyen, P. De Heyn, G. Lepage, J. De Coster, P. Absil, W. Yao, L. Shen, G. Roelkens, J. Van Campenhout, -1 V Bias 67 GHz Bandwidth Si-Contacted Ge p-i-n photodetector for Optical Links at 56 Gb/s and beyond, Optics Express 24(5), 4622-4631 (2016).

3. H. Chen, P. Verheyen, P. De Heyn, G. Lepage, J. De Coster, P. Absil, W. Yao, L. Shen, M. Galili, G. Roelkens, J. Van Campenhout, 100 Gbps RZ Data Reception in 67 GHz Si-contacted Germanium Waveguide p-i-n Photodetectors, (invited) accepted to be published in Journal of Lightwave Technology,
DOI 10.1109/JLT.2016.2593942.

4. H. Chen, P. Verheyen, P. De Heyn, G. Lepage, J. De Coster, P. Absil, G. Roelkens, J. Van Campenhout, Dark Current Analysis in High-speed Germanium

p-i-n Waveguide Photodetectors, Journal of Applied Physics 119 (21), 213105 (2016).

5. H. Chen, J. Verbist, P. Verheyen, P. De Heyn, G. Lepage, J. De Coster, P. Absil, X. Yin, J. Bauwelinck, J. Van Campenhout, G. Roelkens, "High sensitivity 10Gb/s Si photonic receivers based on a low-voltage waveguide coupled Ge avalanche photodetector, Optics Express 23(2), 815-822 (2015).

6. H. Chen, J. Verbist, P. Verheyen, P. De Heyn, G. Lepage, J. De Cster, P. Absil, B. Moeneclaey, X. Yin, J. Bauwelinck, J. Van Campenhout, G. Roelkens, 25 Gbps 1310nm optical receiver based on a sub-5V waveguide-coupled germanium avalanche photodiode, IEEE Phtonics Journal 7(4), 7902909 (2015).

7. A. Srinivasan, M. Pantouvaki, S. Gupta, H. Chen, P. Verheyen, G. lepage, G. Roelkens, K. Saraswat, D. Van Thourhout, P. Absil, J. Van Campenhout, 56Gb/s Germanium Waveguide Electro-Absorption Modulator, (invited) Journal of Lightwave Technology 34(2), 419-424 (2015).

8. J. Zhang, J. Verbist, B Moeneclaey, J. van Weerdenburg, R. Van Uden, H. Chen, J. Van Campenhout, C.M. Okwonko, X. Yin, J. Bauwelinck, G. Roelkens, Ultra-compact, low power consumption silicon photonic/electronic QPSK/16-QAM coherent receiver operating at 28Gbaud, IEEE Photonics Journal 8(1), 7100110 (2016).

A.3 International conferences

1. H. Chen, P. Verheyen, P. De Heyn, G. Lepage, J. De Coster, P. Absil, G. Roelkens, J. Van Campenhout, -1 V Bias 56 Gbps Germanium Waveguide p-i-n Photodetector with Silicon Contacts, Optical Fiber Communication Conference 2016, paper Tu2D.6 United States.

2. H. Chen, P. Verheyen, M. Rakowski, P. De Heyn, G. Lepage, J. De Coster, P. Absil, G. Roelkens, J. Van Campenhout, Low-voltage Ge avalanche photodetector for highly sensitive 10Gb/s Si photonic receivers, International Conference on Group IV Photonics 2014, 106-107, France.

3. H. Chen, J. Verbist, P. Verheyen, P. De Heyn, G. Lepage, J. De Coster, P. Absil, X. Yin, J. Bauwelinck, J. Van Campenhout, G. Roelkens, Low-voltage waveguide Ge APD based high sensitivity 10Gb/s Si photonic receiver, European Conference on Optical Communication 2015, paper Tu.1.3.4, Spain.

4. H. Chen, J. Verbist, P. Verheyen, P. De Heyn, G. Lepage, J. De Coster, P. Absil, X. Yin, J. Bauwelinck, J. Van Campenhout, G. Roelkens, Sub-5V Germanium waveguide avalanche photodiode based 25Gb/s 1310nm optical receiver, Asia Communications and Photonics Conference 2015, paper AM1B.4, HONG KONG. (IEEE Photonics Society Best Student Paper).

5. P. Verheyen, M. Pantouvaki, J. Van Campenhout, P. Absil, H. Chen, P. De Heyn, G. Lepage, J. De Coster, P.Dumon, A. Masood, D. Van Thourhout, R. Baets, and

W. Bogaerts, Highly uniform 25 Gb/s Si photonics platform for high-density, low-power WDM optical interconnects, in Integrated Photonics Research, Silicon and Nanophotonics 2014, paper IW3A.4, United States.

6. P. Absil, P. De Heyn, H. Chen, P. Verheyen, G. Lepage, M. Pantouvaki, J. De Coster, A. Khanna, Y. Drissi, D. Van Thourhout, J. Van Campenhout, Imec iSiPP25G silicon photonics: a robust CMOS-based photonics technology platform, SPIE Photonics West 2015, 9367, Silicon Photonics X, 93670V, United States.

7. P. Absil, P. De Heyn, H. Chen, A. Srinivasan, P. Verheyen, S. Balakrishnan, G. Lepage, M. Pantouvaki, J. De Coster, G. Roelkens, D. Van Thourhout, J. Van Campenhout, Isipp-200: a silicon photonics platform supporting optical data rates beyond 50Gb/s, (invited) SPIE Photonics West 2016 , United States.

8. M. Rakowski, M. Pantouvaki, P. De Heyn, P. Verheyen, M. Ingels, H. Chen, J. De Coster, G. Lepage, B. Snyder, K. De Meyer, M. Steyaert, N. Pavarelli, Jun Su Lee, P. O'Brien, P. Absil, J. Van Campenhout, A 420Gb/s WDM Ring-Based Hybrid CMOS Silicon Photonics Transceiver, IEEE International Solid State Circuit Conference 2015, 408-410, United States.

9. M. Pantouvaki, P. De Heyn, M. Rakowski, P. Verheyen, B. Snyder, A. Srinivasan, H. Chen, J. De Coster, G. Lepage, P. Absil, J. Van Campenhout, 50 Gb/s Silicon Photonics Platform for Short-Reach Optical Interconnects, (invited) Optical Fiber Communication Conference 2016, United States.